RETRIEVAL OF AEROSOL MICROPHYSICAL PROPERTIES FROM THE AERONET

PHOTO-POLARIMETRIC MEASUREMENTS

by

Xiaoguang Xu

A DISSERTATION

Presented to the Faculty of

The Graduate College at the University of Nebraska

In Partial Fulfilment of Requirements

For the Degree of Doctor of Philosophy

Major: Earth & Atmospheric Sciences
(Meteorology/Climatology)

Under the Supervision of Professor Jun Wang

Lincoln, Nebraska

May, 2015

Table of Contents

List of Figures

List of Tables

CHAPTER 1

INTRODUCTION

1.1   Background and Motivation

Atmospheric aerosols play a crucial role in the global climate change. They affect earth energy budget directly by scattering and absorbing solar and terrestrial radiation, and indirectly through altering the cloud formation, lifetime, and radiative properties [*Haywood and Boucher*, 2000; *Ramanathan et al.*, 2001]. However, quantification of these effects in the current climate models is fraught with uncertainties. The global average of aerosol effective radiative forcing were estimated to range from –0.1 to –1.9 Wm^{-2} with the best estimate of –0.9 Wm^{-2} [*Boucher et al.*, 2013], indicating that the cooling effects of aerosol might counteract the warming effects of 1.82 ± 0.19 Wm^{-2} caused by the increase of carbon dioxide since the industrial revolution [*Myhre et al.*, 2013]. The climate effects of aerosol particles depend on their geographical distribution, optical properties, and efficiency as cloud condensation nuclei and ice nuclei. Key quantities pertain to the aerosol optical and cloud-forming properties include particle size distribution (PSD), chemical composition, mixing state, and morphology [Boucher et al., 2013]. While the daily aerosol optical depth (AOD) can be well measured from current satellite and ground-based remote sensing instrumentations [e.g., *Holben et al.*, 1998; *Kaufman et al.*, 2002], the accurate quantification of aerosol ERF is in no small part hindered by our limited knowledge about the aerosol PSD and refractive index (describing chemical composition and mixing state).

To fully understand the role of aerosol particles in the global climate change, further development in observations along with retrieval algorithms for these aerosol microphysical properties from different platforms are thus highly needed [*Mishchenko et al.*, 2004], and the focus of this two-part series study is the characterization of aerosol properties from ground-based passive remote sensing.

1.1.1   Previous studies on aerosol microphysical retrievals

There have been continuous efforts in determining aerosol microphysical properties from ground-based measurements of direct and/or diffuse solar radiation since *Ångström* [1929] first suggested an empirical relationship between the spectral dependency of extinction coefficients and the size of aerosol particles. Over thirty years later, *Curcio* [1961] inferred the aerosol PSD from the spectral particulate extinction coefficients in the visible and near-infrared regions. Soon with the effective numerical inversion technique developed by *Phillips* [1962] and *Twomey* [1963] specifically for error-involved optimization, a number of studies explored the use of either spectral attenuations or scattered radiances (in a small range of scattering angles) to determine the aerosol PSD [*Twomey and Howell*, 1967; *Yamamoto and Tanaka*, 1969; *Dave*, 1971; *Grassl*, 1971; *Herman et al.*, 1971; *King et al.*, 1978]. *Shaw* [1979] and *Nakajima et al.* [1983] were among the first studies that have combined optical scattering measurements with spectral extinctions to recover particle size spectrum. *Kaufman et al.* [1994] suggested useful information contained in the sky radiances of larger scattering angles to retrieve the aerosol scattering phase function and PSD. The first operational retrieval algorithm for aerosol microphysical properties was introduced by *Nakajima et al.* [1996], when the multi-band automatic sun- and sky-scanning radiometer was deployed in the AErosol RObotic NETwork, or the AERONET [*Holben et al.*, 1998]. All of above mentioned methods treated aerosol particles as homogeneous

spheres and with refractive index assumed a priori, even though the refractive index can highly impact the optical, especially the scattering characteristics [*Hansen and Travis*, 1974]. *Tanaka et al.* [1982, 1983] developed an inversion library method to estimate the complex refractive index and PSD simultaneously from measurements of scattered radiances polarized in the perpendicular and parallel directions. Another concept for determining refractive index from both direct and diffuse angular radiances was developed by *Wendisch and Von Hoyningen-Huene* [1994] and *Yamasoe et al.* [1998], which were based on the fact that sensitivities of scattered radiances to the PSD and those to the refractive index are dominated on different scattering-angular regions. The current AERONET operational inversion algorithm was developed by *Dubovik and King* [2000], which has heritage from algorithms developed by *King et al.* [1978] and *Nakajima et al.* [1983, 1996] but was implemented for simultaneous retrieval of particle size distribution and complex refractive index with sophisticated inclusion of multiple a priori constraints. *Dubovik et al.* [2002a, 2006] further implemented the spheroids in the particle shape consideration for desert dust in the retrieval, and added fractional volume of non-spherical particles to the inversion products.

1.1.2   The AERONET measurements

With over 400 locations around the word, most AERONET sites are equipped with an automatic sun and sky scanning spectral radiometer, or the CIMEL-318 type SunPhotometer (Figure 1.1a), to routinely measure direct and diffuse solar radiation in various atmospheric window channels [*Holben et al.*, 1998]. As listed in Table 1.1 and illustrated in Figure 1.1, these measurements include direct sun radiances, sky radiance on both the solar almuncantar and pruncipal planes, as well as the optional polarization of sky light on the solar principal plane.
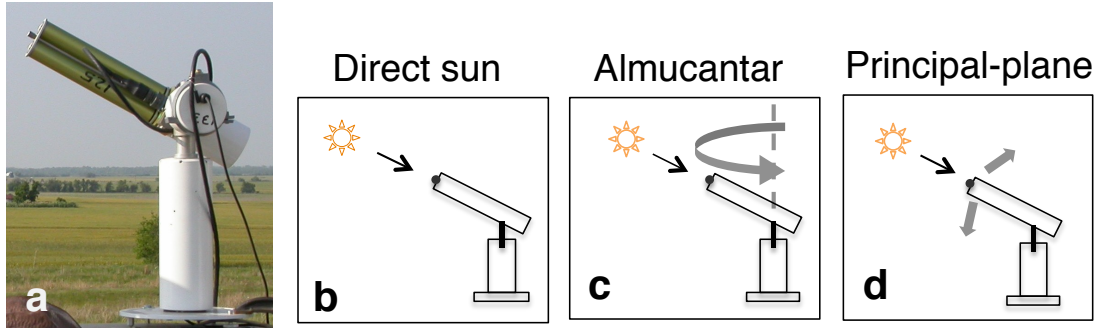
Figure 1.1: A photo of the CIMEL-318 type SunPhotometer and its observational modes.

Direct sun radiances at various atmospheric window channels from the ultra-violet (UV) to near-infrared (NIR) are used to infer the spectral AODs with the Beer-Lambert-Bouguer Law [*Holben et al.*, 1998; *Smirnov et al.*, 2000]. Depending on site-specific instruments, AOT values are typically reported at 7 wavelengths centered at 340 nm, 380 nm, 440 nm, 500 nm, 675 nm, 870 nm, and 1020 nm. Their calibration errors are believed to as small as 0.01 for visible and NIR bands and 0.02 for UV bands.

Sky radiance measurements, which are performed at 440, 670, 870, and 1020-nm bands with full width spectrum at half maximum (FWHM) of 10 nm, are acquired from both solar almucantar and solar principal plane. An almucantar is a series of measurements taken at the viewing angle of the sun for 76 specified relative azimuthal angles (for detail see table 2 of citepholben98). To achieve an enough range of scattering angles, almucantar scans are usually made at an optical air mass of 1.7 or more (corresponding to solar zenith angle larger than about 50°). The principal-plane sequence for each spectrum performs right after almucantar scans. It begins with a sun observation, moves 6°) below the sunray, sweeps up through the sun, and ends at a scattering angle of 150°) or viewing angle achieves horizon, collecting radiances from up to 42 viewing angles. Hereinafter, we will use I_{alm} and I_{ppl} to represent the sky radiances from the solar almucantar and solar principal plane, respectively.

These sky radiance data are used in the current AEROENT operational inversion al-

Table 1.1: Measurement sequences of the CIMEL-318 SunPhotometer.

	Spectra (nm)	Viewing Geometry (°)	Applications
Direct sun	340–1020 340–1640[a]	Target to the sun	AOD, P_w, AE
Almucantar (I_{alm})	440, 675, 870, 1020 (340, 380, 500, 1640)[a]	Azimuth angles relative to Sun: 6, 5, 4.5, 4, 3.5, 3, 2.5, 2, –2, –2.5, –3, –3.5, –4, –4.5, –5, –6, –8, –10, –12, –14, –16, –18, –20, –25, –30, –35, –40, –45, –50, –60, –70, –80, –90, –100, –110, –120, –130, –140, –160, –180 (Duplicate above sequence for a complete counter clockwise rotation to –6)	PSD, m_r, m_i, SSA, phase function
Principal-plane (I_{ppl})	Same as above	Scattering angle from Sun: –6, –5, –4.5, –4, –3.5, –3, –2.5, –2, 2, 2.5, 3, 3.5, 4, 4.5, 5, 6, 8, 10, 12, 14, 16, 18, 20, 25, 30, 35, 40, 45, 50, 60, 70, 80, 90, 100, 110, 120, 130, 140 (negative is below the Sun)	Same as above
Polarization (I_{pp}, $DOLP_{pp}$)	870, (340, 380, 440, 500, 675, 870, 1020, 1640)[a]	Zenith angle on the solar principal plane: –85, –80, –75, –70, –65, –60, –55, –50, –45, –40, –35, –30, –25, –20, –15, –10, –5, 5, 10, 15, 20, 25, 30, 35, 40, 45, 50, 55, 60, 65, 70, 75, 80, 85 (negative is in the antisolar direction)	Not used yet

[a]Additional measurements taken by the newer-generation CIMEL-318DP SunPhotometer.

gorithm [*Dubovik and King*, 2000; *Dubovik et al.*, 2006] (hereafter Dubovik00&06) to derive: (1) the aerosol particle size distribution (PSD) in terms of the aerosol volume (in the atmospheric column) at 22 size bins, (2) the fractional volume of non-spherical particles, and (3) the complex refractive index assumed to be independent of particle size. From those microphysical parameters, the Dubovik00&06 algorithm computes the aerosol single scattering albedo (SSA) and the phase function. Uncertainties in the AERONET inversion products are 15–100% for the bin-based PSD parameters, 0.025–0.05 for real-part refractive index and 0.03 for SSA [*Dubovik et al.*, 2000].

Light polarization measurements are performed optionally over many sites. They are measured by the SunPhotometer with three polarizers placed 60° between each axial direction. The total radiance is derived by

$$I_{pp} = \frac{2}{3} \left(I_1 + I_2 + I_3 \right), \tag{1.1}$$

where I_1, I_2, and I_3 are radiance with these three polarizers, respectively. The degree of linear polarization (DOLP) of skylight is inferred by

$$\mathrm{DOLP_{pp}} = \frac{2(I_1^2 + I_2^2 + I_3^2 - I_1 I_2 - I_2 I_3 - I_1 I_3)^{(1/2)}}{I_1 + I_2 + I_3}. \tag{1.2}$$

It should be noted that we prefer to use $\mathrm{DOLP_{pp}}$ instead of polarized radiance in our inversion, since as a relative quantity it is more accurate. Polarization measurements are made every hour (right after principal plane scans) at 870 nm in the principal plane at $5°$ increments between viewing zenith angle of $-85°$ and $+85°$. These measurements are optional depending on the instrument version and configuration, and are currently available mostly over European and African stations. Recently, multi-spectral polarizations have also been taken with a newer-generation SunPhotometer (CIMEL CE318-DP) at some sites [*Li et al.*, 2009] and the UAE^2 fields campaign [*Reid et al.*, 2008]. Here we focus our study on using multi-spectral polarizations for the inversion of aerosol parameters.

1.1.3 Challenges and opportunities

While the AERONET AOD and other inversion products have been widely used to study the climatology of aerosol optical properties [*Dubovik et al.*, 2002b; *Levy et al.*, 2007a] and for the development and validation of aerosol retrieval algorithms for satellite sensors such as the Moderate Resolution Imaging Spectrometer (MODIS) [*Kaufman et al.*, 1997; *Remer et al.*, 2005; *Levy et al.*, 2007b, 2010; *Wang et al.*, 2010] and the Multi-angle Imaging SpectroRadiometer (MISR) [*Diner et al.*, 1998; *Kahn et al.*, 2010], the AERONET operational algorithm also faces: (i) challenges in evaluation of aerosol data either retrieved from newer-generation satellite sensors or simulated from chemistry transport models, and (ii) opportunities to improve the retrieval through the use of multi-spectral polarization measurements that are now available at a few sites and will be made available at more sites as

part of the AERONET future research development (http://aeronet.gsfc.nasa.gov).
These challenges and opportunities, as further described below, are also the motivation for
us to develop a new research algorithm.

The first challenge is that newer-generation satellite sensors are expected to offer aerosol
microphysical products with accuracy that is equivalent to, if not higher than, that of the
current AERONET microphysical products. For instance, the Aerosol Polarimetry Sensor
(APS) for the NASA Glory mission, through measuring the first three Stokes vector elements
simultaneously from 250 viewing angles at nine spectral bands (410, 443, 556, 670, 865,
910, 1370, 1610, and 2200 nm), was designed to retrieve aerosol effective radius (r_{eff}),
effective variance (v_{eff}), and spectral complex index of refraction for both fine and coarse
modes [*Mishchenko et al.*, 2007]. While no actual product is available because of the failure
of Glory launch, several case studies with the APS's prototype airborne sensor, RSP (the
Remote Sensing Polarimeter), demonstrated feasibility of APS algorithm [*Chowdhary et al.*,
2002, 2005; *Mishchenko et al.*, 2004; *Waquet et al.*, 2009]. At least in the case of spherical
particles, the accuracy of APS's bi-modal aerosol products was expected to be 10% for r_{eff},
40% for v_{eff}, 0.02 for m_{r}, and 0.03 for the SSA (ω_{A}) [*Mishchenko et al.*, 2007]. Some of
these accuracy expectations are unlikely to be matched by existing ground-based and in
situ instruments, including those at the AERONET sites. Moreover, the current AERONET
retrieval of the refractive index and the ω_{A} are not recommended to use when the 440-nm
AOD is lower than 0.4 [*Holben et al.*, 2006] due to expected limited accuracy identified in
the detailed sensitivity study by [*Dubovik et al.*, 2000].

The second challenge is associated with the inconsistency in assumptions of PSD that
exists between current AERONET inversion products and satellite retrievals on the one
hand, as well as the aerosol models used by climate models on the other hand. Specifically,
the Dubovik00&06 algorithm retrieves the aerosol PSD on in 22 discrete size bins. In
contrast, a continuous PSD function (e.g., lognormal) is usually assumed in satellite retrieval

algorithms, such as those for APS/RSP [*Mishchenko et al.*, 2007; *Waquet et al.*, 2009] and the POLDER/PARASOL algorithm [*Hasekamp et al.*, 2011]. Also, aerosol microphysical properties are usually calculated with continuous PSD assumptions in many chemistry transport models, such as GEOS-Chem [*Drury et al.*, 2010; *Wang et al.*, 2010] and the GOCART model [*Chin et al.*, 2002]. Clearly, the actual aerosol PSD is never a perfect lognormal distribution, but neither it is discrete. At least from the scattering perspective, the aerosol PSD can be well characterized with an effective radius r_{eff} and an effective variance v_{eff}, while the specific function of the PSD is shown to be much less important [*Hansen and Travis*, 1974]. In other words, since the retrieval is based on the information content in the particle optical scattering, the most relevant size parameters, regardless of the PSD shape, should be r_{eff} and v_{eff}, at least for spherical particles.

The third challenge is that the assumption of a size-independent refractive index (and SSA) in Dubovik00&06 is not in line with the majority of counterpart satellite retrieval algorithms [e.g., *Mishchenko et al.*, 2007; *Hasekamp et al.*, 2011; *Martonchik et al.*, 2009], which often uses different refractive indices for various individual aerosol modes. In many cases, tropospheric aerosol is a mixture of modes with substantially different refractive indices. For example, smoke from biomass burning can be mixed with mineral dust over western coastal North Africa [*Yang et al.*, 2013]. Furthermore, the assumption of size-independent refractive index can lead to errors in the retrieval of the size distributions when the refractive indices for fine- and coarse-mode aerosols differ substantially [*Dubovik et al.*, 2000; *Chowdhary et al.*, 2001]. Thus, a mode-resolved parameterization of the refractive index in an aerosol retrieval algorithm not only can facilitate the validation of satellite products and chemistry transport models, but also is expected to improve the accuracy of PSD and SSA retrievals for each mode. [*Dubovik et al.*, 2000] have tested the possibility of retrieving separated refractive indices of fine and coarse modes, however, they concluded that the retrieval of bi-modal refractive indices is essentially non-unique due to limited

information in the AERONET radiance-only observations.

Therefore, this work aims to developing an algorithm to retrieve the aerosol microphysical properties of both fine and coarse aerosol modes, which embraces the future opportunities of deploying polarization measurements through AERONET, and ameliorates the aforementioned limitations in the Dubovik00&06 algorithm by incorporating both radiance and polarization data. Polarization measurements contain valuable information on aerosol microphysical properties [*Mishchenko and Travis*, 1997], as the polarization of the scattered light is highly sensitive to aerosol size and refractive index [*Hansen and Travis*, 1974; *Mishchenko et al.*, 2002]. We note, however, their conclusions were based on consideration of spherical aerosol particles and were primarily from a theoretical point of view. In contrast, the studies by *Dubovik et al.* [2006] and *Deuzé et al.* [1993, 2001] revealed serious limitation of polarimetric retrieval of the properties for coarse, especially non-spherical aerosols. Moreover, *Dubovik et al.* [2006] have shown that while the polarimetic observation of fine particles and large spheres are highly sensitive to real part of refractive index, even they have non-negligible sensitivity to particle shape. Therefore, adding polarization measurements to the inversion has great potential to improve the accuracy of AERONET microphysical retrievals, provided that the difficulty of representing aerosol particle shapes is recognized or adequately addressed. In these regards, most of the past efforts seem to suggest clear improvements in characterization of fine mode aerosol using polarimetric observations. For example, *Li et al.* [2009], based upon the Dubovik00&06 algorithm, demonstrated the possibility to reduce errors in the fine-mode size distribution, real part of the refractive index, and particle shape parameters.

1.2   Research Goals and Thesis Outline

As discussed above, this dissertation seeks to contribute to an improved research algorithm to retrieval aerosol micriphysical properties from AERONET measurements of light radiance and polarization, with emphasis on elucidating the potentially important role of polarization measurements. It does so by pursuing three following spcifci objectives:

1. *Develop ground-based inversion algorithms for the retrieval of r_{eff}, v_{eff}, m_r, and m_i from a combined use of direct solar radiance, skylight radiance and skylight linear polarization measurements from AERONET.*

2. *Perform a sensitivity study and error budgeting exercise to characterize retrieval accuracy and error sources.*
   By doing so, we can answer the questions:

3. *Perform ground-based retrievals using available AERONET polarimetric measurements.*

CHAPTER 2

MODEL DEVELOPMENTS

2.1 Introduction

The radiation fields—radiance and the state of polarization—measured by the AERONET SunPhotometer are the outcome of solar radiation interacting with various physical processes including the absorption and scattering by atmospheric molecules, aerosols and clouds, as well the reflection and absorption by underlying surface. The radiance and polarization of light at any wavelength can be represented by a Stokes column vector $\mathbf{I}$ having four elements [*Hansen and Travis*, 1974]:

$$\mathbf{I} = [I, Q, U, V]^T, \tag{2.1}$$

where I is the total intensity (or radiance), Q and U describe the state of linear polarization, V describes the state of circular polarization, and T indicates a transposed matrix. It should be noted that all radiation fields and optical parameters used in this paper are functions of the light wavelength λ. For simplicity, however, we omit λ in all formulas. The degree of linear polarization (DOLP) is defined by

$$\text{DOLP} = \frac{\sqrt{Q^2 + U^2}}{I}. \tag{2.2}$$

In the solar principal plane, U is negligibly small and the above formula becomes $\text{DOLP} = -Q/I$. Let $\mathbf{I}_0 = [I_0, 0, 0, 0]^T$ denote the Stokes vector for incident Solar radiation

at the top of the atmosphere (TOA) from the direction (θ_0, ϕ_0), where θ_0 and ϕ_0 are the incident solar zenith and azimuth angles, respectively. For a plane-parallel atmosphere bounded below by a reflective surface, the vector radiative transfer equation in the medium for the specific intensity column vector $\mathbf{I}$ of light propagating in the viewing direction (θ, ϕ) can be written [*Hovenier et al.*, 2004; *Mishchenko et al.*, 2002]:

$$\mu \frac{\partial \mathbf{I}(\tau, \mu, \phi)}{\partial \tau} = \mathbf{I}(\tau, \mu, \phi) - \mathbf{J}(\tau, \mu, \phi; \mu_0, \phi_0) \tag{2.3}$$

$$\begin{aligned}
\mathbf{J}(\tau, \mu, \phi; \mu_0, \phi_0) &= \frac{\omega}{4\pi} \int_{-1}^{1} \int_{0}^{2\pi} \mathbf{P}(\tau, \mu, \mu_0, \phi - \phi_0) \mathbf{I}(\tau, \mu_0, \phi_0) \mathrm{d}\phi_0 \mathrm{d}\mu_0 \\
&+ \frac{\omega}{4\pi} \mathbf{P}(\tau, \mu, \mu_0, \phi - \phi_0) \mathbf{I}_0 \exp(-\tau/\mu_0)
\end{aligned} \tag{2.4}$$

Here, τ is the extinction optical depth measured from TOA, μ and μ_0 are cosines of θ and θ_0, respectively, ω is the SSA and $\mathbf{P}$ is the phase matrix. The first term in equation (2.3) represents multiple scattering contributions, while the second indicates scattered light from the direct solar beam.

Parameters required to solve the above radiative transfer equation are τ, ω, and $\mathbf{P}(\Theta)$ for the atmosphere, and the reflectance matrix $\mathbf{R}_s(\tau, \mu, \phi; \mu_0, \phi_0)$ of the underlying surface. Considering a cloud-free atmosphere, the solar radiation is attenuated by molecular scattering, gaseous absorption, and aerosol scattering and absorption. For a given layer, we have

$$\tau = \tau_A + \tau_R + \tau_G \tag{2.5}$$

$$\omega = \frac{\tau_A \omega_A + \tau_R}{\tau} \tag{2.6}$$

$$\mathbf{P}(\Theta) = \mathbf{P}_A(\Theta) \frac{\tau_A \omega_A}{\tau_A \omega_A + \tau_R} + \mathbf{P}_R(\Theta) \frac{\tau_R}{\tau_A \omega_A + \tau_R} \tag{2.7}$$

where τ_A, τ_R, and τ_G are optical depth, respectively, by aerosol extinction, Rayleigh scattering of air density fluctuations, and gaseous absorption. ω_A is the SSA of aerosol, and

$\mathbf{P}_A(\Theta)$ and $\mathbf{P}_R(\Theta)$ are, respectively, the aerosol and Rayleigh phase matrices as functions of the scattering angle Θ. Therefore, the forward modeling development thus requires the computation of single scattering properties for aerosols and air density fluctuations, rigorous treatment for absorption of trace gases, accuracte representation of reflectance/polarization by surface, an the realistic simulation of polarimetric radiative transfer.

In this regard, we have developed the UNified Linearized Vector Radiative Transfer Model, or UNL-VRTM, specifically for simulation, analysis, and inversion of the photo-polarimetric measurements. Components of the UNL-VRTM are described in section 2.2, and the model benchmarking and verification are presented in section 2.3.

2.2   The UNL-VRTM

As shown in Figure 2.1, the UNL-VRTM comprises 6 modules; they are

1. A module computing Rayleigh scattering (section 2.2.1);

2. A module that deal with gaseous absorption (section 2.2.1);

3. A linearized Mie scattering code (section 2.2.2);

4. A linearized T-matrix electromagnetic scattering code (section 2.2.2);

5. A surface model computing various bidirectional reflectance/polarization functions (BRDF/BPDF) (section 2.2.3);

6. A vector linearized radiative transfer model—VLIDORT (section 2.2.4).

These modules are integrated for the forward calculation of aerosol single scattering, gas absorption, and vector radiative transfer hereafter, and thus they together constitute the UNified Linearized Radiative Transfer Model, UNL-VRTM.
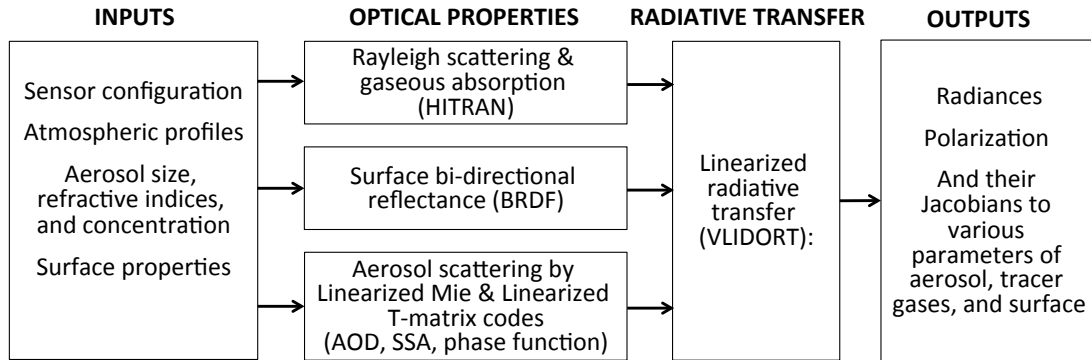
Figure 2.1: Flowchart of the UNL-VRTM. See text for detail.

Inputs for the UNL-VRTM are profiles of atmospheric properties and constituents (temperature, pressure, aerosol mass concentration or layer AOD, water vapor amount and other trace gas volume mixing ratio profiles [*McClatchey et al.*, 1972]), the surface properties, as well as the aerosol parameters (such as PSD parameters and refractive index) themselves. Bearing in mind the lack of sensitivity in passive remote sensing for the retrieval of vertical profiles of aerosol properties, the UNL-VRTM as it stands now is only designed to deliver radiative calculations for a maximum of two sets of aerosol single scattering properties (e.g., aerosol PSD, refractive index, and particle shape), typically with one fine-mode and one coarse-mode aerosol. Other inputs for model include spectral and geometrical definitions that characterizing specification of an observing sensor.

Outputs of the model include the Stokes vector (**I**) at user-defined spectral wavelengths and desired atmospheric levels for both upwelling and downwelling radiation, from which the light radiance and degree of polarization can be derived. Outputs also include analytical Jacobians of **I** with respect to all aerosol particle parameters (PSD, refractive index, vertical profile), Rayleigh scattering optical depth, optical depth of all trace gases, and parameters describing surface optical property. A detail description of the UNL-VRTM's Jacobian capability is presented in section 2.2.5.

2.2.1 Molecular scattering and absorption

The Rayleigh scattering optical depth at certain wavelength in any atmospheric layer (τ_R) is computed by

$$\tau_R = N_{air}\sigma_R \tag{2.8}$$

where N_{air} is air molecular number density of that layer (molec cm^{-2}), and σ_R is the Rayleigh scattering cross-section (cm^2 molec^{-1}) computed following *Bodhaine et al.* [1999]. The Rayleigh phase matrix, $\mathbf{P}_R(\Theta)$, depends upon molecular anisotropy through the depolarization factor, also computed from the same source. *Bodhaine et al.* [1999] computes the wavelength-dependent Rayleigh scattering cross-section as a function of mixing ratios for N_2, O_2, H_2O, and CO_2. The phase matrix for Rayleigh scattering follows *Hansen and Travis* [1974]; we use the set of spherical-function expansion coefficients for the phase matrix as supplied for VLIDORT [*Spurr*, 2006].

Calculation of the absorption optical depth (τ_G) at any atmospheric layer for K different trace gases follows

$$\tau_G = \sum_{i=1}^{K} N_{gas,i}\sigma_{A,i}(T,P) \tag{2.9}$$

where $N_{gas,i}$ is the number density of ith gas within that layer, and $\sigma_{A,i}$ is the corresponding absorption cross-section, a function of temperature and pressure. Our model accounts for absorptions by a total number of 22 trace gases: H_2O, CO_2, O_3, N_2O, CO, CH_4, O_2, NO, SO_2, NO_2, NH_3, HNO_3, OH, HF, KCl, HBr, HI, ClO, OCS, H_2CO, HOCl, and N_2. The determination of σ_A utilizes a UV-to-visible cross-section library and the line-spectroscopic absorption parameters archived in the HITRAN database [*Orphal and Chance*, 2003; *Rothman et al.*, 2009]. The cross-section library compiles the extinction cross-section for O_3, NO_2, SO_2, and O_2-O_2 in the UV and/or visible spectral regions. Meanwhile, line-spectroscopic absorption databased are used to simulate the pressure- and temperature-dependent extinc-

tion cross-section with line-by-line (LBL) approach [*Liou*, 2002; *Rothman et al.*, 2009] by accumulating each individual absorption line. Doppler broadening is calculated from the molecular mass and the temperature, and Doppler and Lorentz broadening are included in the Voigt calculation.

Particular to work, we only consider the most influential trace species for the AERONET spectral bands: H_2O (vapor), O_3, and NO_2. In our algorithm (section 3), the columnar amounts of O_3 and NO_2 are dynamically adjusted with retrievals from the Ozone Monitoring Instrument (OMI) [*Levelt et al.*, 2006] on board the AURA satellite. We apply the columnar water vapor amount retrieved from the 940-nm radiances measured by the AERONET SunPhotometer *Halthore et al.* [1997].

2.2.2 Aerosol single scattering

Aerosol single scattering properties necessary to the radiative transfer calculation include aerosol optical depth (τ_A) (Q_{ext}), SSA (ω_A), and scattering phase matrix ($\mathbf{P}_A(\Theta)$). The calculation of these parameters is made with a Linearized Mie (LMIE) scattering electromagnetic code for spherical particles and a Linearized T-matrix (LTMATRIX) scattering code for non-spherical convex and axially symmetric particles [*Spurr et al.*, 2012]. The LMIE code originates from the Mie code of *de Rooij and Stap* [1984], and the LTMATRIX code originates from the T-Matrix code developed by *Mishchenko et al.* [1996]; *Mishchenko and Travis* [1998]; both include linearization capabaility developed by *Spurr et al.* [2012].

Common inputs for both codes are the complex refractive index ($m_r + im_i$), and the particle size distribution (PSD) parameters for polydisperse scattering. The codes have several options to specify the PSD function: two-parameter gamma, two-parameter lognormal, three-parameter modified gamma, and four-parameter bi-lognormal. In addition, the linearized T-matrix code offers options to characterize the shape of non-spherical aerosols

(spheroids, cylinders, or Chebyshev particles) [*Spurr et al.*, 2012]. For non-spherical particles, the specified size distribution is interpreted as the equivalent surface-area sphere in the linearized T-matrix calculation, regardless of the shape.

For AERONET inversion alorithm, we assume that the aerosol volume distribution follows a bi-modal lognormal function [in agreement wit *Schuster et al.*, 2006; *Waquet et al.*, 2009]:

$$\frac{dV}{d\ln r} = \sum_{i=1}^{2} \frac{V_0^i}{\sqrt{2\pi}\ln\sigma_g^i} \exp\left[-\frac{(\ln r - \ln r_v^i)^2}{2\ln^2\sigma_g^i}\right] \tag{2.10}$$

where V_0, r_v, and σ_g are the total volume concentration, geometric median radius, and standard deviation, respectively. The superscript i indicates the size mode, and later will be replaced by 'f' for fine mode and 'c' for coarse mode. We assume that particle size ranges from 0.01 to 10 μm for the fine mode and from 0.05 to 20 μm for the coarse mode, both covering $> 99.9\%$ of the total volume of an idealistic size range $(0, +\infty)$. An advantage of the lognormal distribution is that standard deviations for the number, area, and volume PSD functions are identical, and therefore allowing that the median radii for these PSD functions can be converted from one to another [*Seinfeld and Pandis*, 2006]. The r_{eff} and v_{eff} are related to the geometric parameters through:

$$r_{\text{eff}} = r_v \exp\left(-\frac{1}{2}\ln^2\sigma_g\right), \tag{2.11}$$

$$v_{\text{eff}} = \exp\left(\ln^2\sigma_g\right) - 1. \tag{2.12}$$

The LMIE/LTMATRIX code computes the aerosol extinction efficiency factor Q_{ext}, single scattering albedo ω_A, and phase matrix $\mathbf{P}_A(\Theta)$, as well as Jacobians of these quantities with respect to input parameters including r_{eff}, v_{eff}, m_r, and m_i. The phase matrix and its Jacobians are expressed in terms of the coefficients $\mathbf{B}_A(\Theta)$ for each moment l in terms of the generalized spherical function expansions for each non-zero phase matrix element. Let

A denotes the vector of aerosol microphysical parameters, $\mathbf{A} = [V_0, r_{\text{eff}}, v_{\text{eff}}, m_{\text{r}}, m_{\text{i}}]^T$, and **M** the vector of aerosol optical parameters, $\mathbf{M} = [\tau_{\text{A}}, \omega_{\text{A}}, \mathbf{B}_{\text{A}}(\Theta)]^T$, where τ_{A} is related to Q_{ext} by $\tau_{\text{A}} = \frac{3V_0 Q_{\text{ext}}}{4r_{\text{eff}}}$. The LMIE/LTMATRIX code acts as an operator that maps vector **A** to **M**. The Jacobian matrix of **M** with respect to **A** calculated by means of the linearization feature of the code, and it can be expressed by $\nabla_{\mathbf{A}} \mathbf{M}$.

2.2.3 Surface representations

VLIDORT has a supplementary module for specification of the surface BRDF as a linear combination of (up to) three semi-empirical kernel functions; for details, see *Spurr* [2004]. This supplementary module can also provide partial derivatives of the BRDF with respect to the kernel weighting factors or with respect to kernel parameters such as the wind speed for glitter reflectance. These kernel functions include Lambertian, Ross-Thick, and Li-Sparse functions [*Wanner et al.*, 1995; *Lucht et al.*, 2000], a Bi-directional Polarization Distribution Function (BPDF) [*Maignan et al.*, 2009], and an ocean surface model based on the Cox-Munk model [*Cox and Munk*, 1954]. In addition, VLIDORT has an option for using a surface-leaving radiation field, either as a fluorescence term or as a water-leaving term expressed as a function of chlorophyll absorption.

Although surface reflectance has in general a low influence on AERONET down-welling sky radiances and polarization, a state-of-the-art representation of the surface reflectivity potentially reduces model uncertainties, especially for measurements taken at low elevation angles that could be affected by surface diffusion. Here, we utilize the spectral BRDF parameters from the MODIS surface products that are operationally reported every 16 days at a 1-km resolution [*Lucht et al.*, 2000]. Here we use time-matched MODIS BRDF products to reconstruct the bidirectional reflectance over AERONET stations. The MODIS BRDF product supplies three weighting parameters (f_{iso}, f_{vol}, and f_{geo}) for the first 7 MODIS

bands, respectively, corresponding to three kernel types: isotropic, Ross-Thick (K_{vol}), and Li-Sparse (K_{geo}):

$$\rho_{\text{R}}(\mu,\phi;\mu_0,\phi_0) = f_{\text{iso}} + f_{\text{vol}}K_{\text{vol}}(\mu,\phi;\mu_0,\phi_0) + f_{\text{geo}}K_{\text{geo}}(\mu,\phi;\mu_0,\phi_0) \qquad (2.13)$$

Expanded expressions for K_{vol} and K_{geo} appear in *Wanner et al.* [1995]; *Lucht et al.* [2000].

Studies have shown that the BPDF for land surfaces is generally rather small and is "spectrally neutral" [*Nadal and Breon*, 1999; *Maignan et al.*, 2004, 2009; *Waquet et al.*, 2007; *Litvinov et al.*, 2011]. Most empirical BPDF models are based on Fresnel coefficients of light reflectance from the surface. Here we have incorporated the one-parameter model developed by *Maignan et al.* [2009], which was derived from analyses of several years of POLDER/PARASOL measurements. This model describes the polarized reflectance at any viewing geometry (μ, ϕ) from the given incident geometry (μ_0, ϕ_0) as:

$$\boldsymbol{\rho}_{\text{P}}(\mu,\phi;\mu_0,\phi_0) = \frac{C_0\exp(-\tan\theta_{\text{h}})\exp(-\text{NDVI})}{\mu_0+\mu}\mathbf{F}_{\text{P}}(\theta_{\text{h}},n_{\text{v}}) \qquad (2.14)$$

where C_0 is a constant parameter chosen for a certain surface type, θ_{h} is half of the phase angle of reflectance, n_{v} is the refractive index of vegetation (1.5 is used), and $\mathbf{F}_{\text{P}}$ is the Fresnel reflection matrix. We chose a spectrally-independent value for C_0 based on the recommendations by *Maignan et al.* [2009] for relevant surface types.

The combination of the BRDF and BPDF for land surface follows the discussion by *Dubovik et al.* [2011]. The surface reflectance matrix $\mathbf{R}_{\text{s}}(\mu,\phi;\mu_0,\phi_0)$ is represented as a sum of diffuse unpolarized reflectance and specular reflectance; the former is modeled using the MODIS BRDF in equation (2.13), and the latter using the BPDF formula in equation (2.14).

2.2.4 Radiative transfer

The radiative transfer equation (2.3) is solved with the Vector Linearized Discrete Ordinate Radiative Transfer (VLIDORT) model, which is a core part of the UNL-VRTM. VLIDORT, developed by *Spurr* [2006], is a linearized pseudo-spherical vector discrete ordinate radiative transfer model for multiple scattering of diffuse radiation in a stratified multi-layer atmosphere. It computes four elements of the Stokes vector I for downwelling and upwelling radiation at any desired atmospheric level. The VLIDORT includes the pseudo-spherical approximation to calculate solar beam attenuation in a curved medium. It also uses the delta-M approximation for dealing with sharply peaked forward scattering. Specifically for the AERONET inversion, we consider 16 discrete ordinate streams in the radiative transfer calculation and retain 180 terms in the spherical-function expansion of the scattering matrix to ensure accurate calculation of diffuse radiation.

Along with the Stokes vector $\mathbf{I}$, VLIDORT also computes the Jacobian matrix of I with respect to aerosol optical vector $\mathbf{M}$, $\nabla_{\mathbf{M}}\mathbf{I}$. Therefore, the combination of the VLIDORT and the LMIE/LTMATRIX codes allows for a direct calculation of the Jacobian matrix of the Stokes vector with respect to aerosol microphysics, $\mathbf{A}$, by

$$\nabla_{\mathbf{A}}\mathbf{I} = \nabla_{\mathbf{M}}\mathbf{I} \cdot \nabla_{\mathbf{A}}\mathbf{M} \tag{2.15}$$

Essentially, the above equation can yield the derivatives of the radiance I and DOLP with respect to any aerosol microphysical parameter, i.e., $\nabla_{\mathbf{A}}I$ and $\nabla_{\mathbf{A}}$DOLP. While obtaining $\nabla_{\mathbf{A}}I$ is straightforward, $\nabla_{\mathbf{A}}$DOLP can be derived from equation (2.2) following:

$$\nabla_{\mathbf{A}}\text{DOLP} = -\frac{\text{DOLP}\nabla_{\mathbf{A}}}{I} + \frac{Q\nabla_{\mathbf{A}}Q + U\nabla_{\mathbf{A}}U}{I\sqrt{Q^2 + U^2}} \tag{2.16}$$

2.2.5   Capability of calculating Jacobians

This section analytically derives the Jacobian of $\mathbf{I}$ with respect to various aerosol related parameters, including τ_A, ω_A, $\mathbf{B}_A$, refractive index, PSD parameters, and aerosol vertical profile. Computation of the Stokes vector in VLIDORT requires input of an optical property set $[\tau, \omega, \langle \mathbf{B}^j \rangle_{j=0,J}]$ for each atmospheric layer, where $<>_{j=0,J}$ denotes the vector that consists of elements having the similar expression as that inside $<>$ but for $j = 0,J$. For each atmospheric layer L, the optical property inputs are assumed constant and are given by equations (2.5)–(2.6), as well as equation (2.7) with $\mathbf{P}(\Theta)$ replaced by $\mathbf{B}^j$. It should be noted that all parameters in these requations are for each layer, but we ignore L for convenience.

Since VLIDORT generates Jacobians with respect to layer-integrated single scattering properties in each atmospheric layer as well as column-integrated single scattering property as a whole, and LMIE and LTMATRIX offer the sensitivity of aerosol scattering properties to microphysical aerosol physical parameters, an integrated use of VLIDORT and LTMA-TRIX/LMIE can, in principle, provide the Jacobians of Stokes parameters with respect to both aerosol single scattering properties as well as aerosol microphysical parameters (as expressed by equations (2.15)–(2.16)). Practically, the VLIDORT calculation of Jacobians of any Stokes parameter ξ with respect to any aerosol parameter x proceeds according to

$$
\begin{aligned}
x \frac{\partial \xi}{\partial x} &= x \left[\frac{\partial \xi}{\partial \tau}, \frac{\partial \xi}{\partial \omega}, \left\langle \frac{\partial \xi}{\partial \mathbf{B}^j} \right\rangle_{j=1,J} \right] \left[\frac{\partial \tau}{\partial x}, \frac{\partial \omega}{\partial x}, \left\langle \frac{\partial \mathbf{B}^j}{\partial x} \right\rangle_{j=1,J} \right]^T \\
&= \left[\tau \frac{\partial \xi}{\partial \tau}, \omega \frac{\partial \xi}{\partial \omega}, \left\langle \mathbf{B}^j \frac{\partial \xi}{\partial \mathbf{B}^j} \right\rangle_{j=1,J} \right] \left[\phi_x, \varphi_x, \langle \mathbf{\Psi}_x^j \rangle_{j=1,J} \right]^T .
\end{aligned}
\tag{2.17}
$$

The first square bracket on the right-hand side of equation (2.17) contains quantities computed internally by VLIDORT, while the second so-called "transformation vector" must

Table 2.1: Elements of transformation vector for various aerosol single scattering parameters (composite of fine and coarse mode).

x	ϕ_x	φ_x	$\mathbf{\Psi}_x^j$	
τ_A	$\frac{\tau_A}{\tau}$	$\frac{\tau_A}{\tau}\left(\frac{\omega_A}{\omega}-1\right)$	$\begin{cases} \frac{\omega_A\tau_A}{\omega\tau}\left(\frac{\mathbf{B}_A^j}{\mathbf{B}^j}-1\right) & \text{for } j<3 \\ \frac{\tau_R}{\omega\tau} & \text{for } j\geq 3 \end{cases}$	
ω_A	0	$\frac{\tau_A\omega_A}{\tau\tau_A\omega_A+\tau_R}$	Same as above	
$\mathbf{B}_A^j$	0	0	$\begin{cases} \frac{\omega_A\tau_A\mathbf{B}_A^j}{\omega_A\tau_A\mathbf{B}_A^j+\tau_R\mathbf{B}_R^j} & \text{for } m=j<3 \\ 1 & \text{for } m=j\geq 3 \\ 0 & \text{for } m\neq j \end{cases}$	

be supplied by users and is defined as:

$$\phi_x = \frac{x}{\tau}\frac{\partial\tau}{\partial x}; \quad \varphi_x = \frac{x}{\omega}\frac{\partial\omega}{\partial x}; \quad \mathbf{\Psi}_x^j = \frac{x}{\mathbf{B}^j}\frac{\partial\mathbf{B}^j}{\partial x}. \tag{2.18}$$

As we are interested in aerosol parameters, this transformation vector can be further expanded as

$$\left[\phi_x, \varphi_x, \left\langle\mathbf{\Psi}_x^j\right\rangle_{j=1,J}\right]^T = \mathbf{\Pi}\left[\phi_x', \varphi_x', \left\langle\mathbf{\Psi}_x'^j\right\rangle_{j=1,J}\right]^T, \tag{2.19}$$

where

$$\phi_x' = x\frac{\partial\tau_A}{\partial x}, \quad \varphi_x' = x\frac{\partial\delta_A}{\partial x}, \quad \text{and}\,\mathbf{\Psi}_x'^j = x\frac{\partial\mathbf{B}_A^j}{\partial x}, \tag{2.20}$$

and $\mathbf{\Pi}$ is a matrix expressed by

$$\mathbf{\Pi} = \begin{bmatrix} \frac{1}{\tau} & \mathbf{0} & \mathbf{0} \\ -\frac{1}{\tau} & \frac{1}{\delta_A+\tau_R} & \mathbf{0} \\ \mathbf{0} & \left\langle\frac{\mathbf{B}_A^j-\mathbf{B}_R^j}{\mathbf{B}^j(\delta_A+\tau_R)}\right\rangle_{j=1,J} & \left\langle\frac{\delta_A}{\mathbf{B}^j(\delta_A+\tau_R)}\right\rangle_{j=1,J} \end{bmatrix}. \tag{2.21}$$

Here, δ_A is the scattering optical depth of aerosols. The detailed derivations of the matrix $\mathbf{\Pi}$ are presented in Appendix C. Hence, the transformation vector for calculating Stokes profile Jacobians with respect to τ_A, ω_A, $\mathbf{B}_A^j$ can be obtained by combining equations (2.19) and

Table 2.2: Elements of transformation vector for various microphysical parameters of fine and coarse mode aerosols[a].

x	ϕ'_{x^f}	φ'_{x^f}	$\mathbf{\Psi}'^j_{x^f}$
τ^f_A	τ^f_A	δ^f_A	$\frac{\delta^f_A}{\tau_A}(\mathbf{B}^{fj}_A - \mathbf{B}^j_A)$
ω_A	0	δ^f_A	$\frac{\delta^f_A}{\tau_A}(\mathbf{B}^{fj}_A - \mathbf{B}^j_A)$
V^f_0	$\frac{3V^f_0 Q^f_{ext}}{4r^f_{eff}}$	$\frac{3V^f_0 Q^f_{sca}}{4r^f_{eff}}$	$\frac{\delta^f_A}{\tau_A}(\mathbf{B}^{fj}_A - \mathbf{B}^j_A)$
m^f_r, m^f_i	$\tau^f_A \frac{x^f}{Q^f_{ext}}\frac{\partial Q^f_{ext}}{\partial x^f}$	$\delta^f_A \frac{x^f}{Q^f_{sca}}\frac{\partial Q^f_{sca}}{\partial x^f}$	$\frac{\varphi'_{x^f}}{\delta^f_A}(\mathbf{B}^{fj}_A - \mathbf{B}^j_A) + x^f\frac{\partial \mathbf{B}^{fj}_A}{\partial x^f}$
$r^f_g, \sigma^f_g, \varepsilon^f$	$\tau^f_A\left(\frac{x^f}{Q^f_{ext}}\frac{\partial Q^f_{ext}}{\partial x^f} - \frac{x^f}{r^f_{eff}}\frac{\partial r^f_{eff}}{\partial x^f}\right)$	$\delta^f_A\left(\frac{x^f}{Q^f_{sca}}\frac{\partial Q^f_{sca}}{\partial x^f} - \frac{x^f}{r^f_{eff}}\frac{\partial r^f_{eff}}{\partial x^f}\right)$	$\frac{\varphi'_{x^f}}{\delta^f_A}(\mathbf{B}^{fj}_A - \mathbf{B}^j_A) + x^f\frac{\partial \mathbf{B}^{fj}_A}{\partial x^f}$
H^f	$H^f\frac{\partial \tau_A}{\partial H^f}$	$\phi'_{x^f}\omega^f_A$	$\frac{\delta^f_A}{\tau_A}(\mathbf{B}^{fj}_A - \mathbf{B}^j_A)$

[a] Expressions are shown only for fine-mode parameters; expressions for coarse-mode parameters are the same but with superscripts replaced by 'c'

(2.21), and the components of this vector are listed in Table 2.1.

In an atmosphere where both fine (superscript "f") and coarse (superscript "c") aerosol particles co-exist, the ensemble aerosol optical properties may be derived by assuming external mixing:

$$\begin{cases} \tau_A &= \tau^f_A + \tau^c_A \\ \delta_A &= \delta^f_A + \delta^c_A \\ \mathbf{B}^j_A &= \frac{\delta^f_A + \delta^c_A}{\delta^f_A \mathbf{B}^{f,j}_A + \delta^c_A \mathbf{B}^{c,j}_A} \end{cases} \tag{2.22}$$

We can generate the transformation vectors (as listed in Table 2.2) for any of the following parameters: τ^f_A, ω^f_A, V^f_0, m^f_r, m^f_i, r^f_g, σ^f_g, ε^f, H^f, and τ^c_A, ω^c_A, V^c_0, m^c_r, m^c_i, r^c_g, σ^c_g, ε^c, and H^c. Here, r_g, σ_g, and H denote the median and standard deviation of the particle radius (e.g., two parameters in the log-normal aerosol number distribution), and the scale height of aerosol extinction, respectively. V_0 is the aerosol volume concentration and ε the shape factor of the non-spherical particle. Details of the algebra for deriving the transformation vectors may be found in Appendix C. Note that the shape of the aerosol extinction vertical profile in the testbed is assumed to be constant or exponentially decreasing with height or quasi-Gaussian (Appendix C). The analytical formulas for ϕ'_x, φ'_x, and $\mathbf{\Psi}'^j_x$ for coarse mode

aerosol parameters are the same as their counterparts for fine-mode aerosols; we need only replace superscript "s" with "c" in Table 3 entries. Jacobians with respect to the fine mode fraction, either in terms of AOD (fmf_τ) or in terms of the volume concentration (fmf_v), can be derived from the corresponding Jacobians with respect to modal AOD and volume, respectively:

2.3   Model Benchmarking and Verifications

Figure 2.2a shows the downward solar spectral irradiance at the top-of-atmosphere and at the surface for a solar zenith angle of $30°$. Spectral regions dominated by gas absorption can be clearly identified, including the O_3 Hartley-Huggins bands in the UV, the O_2B band (0.69 μm) and O_2A band (0.76 μm), as well as a number of water vapor bands. The spectroscopic calculations shown in Figure 2.2 were performed at a resolution of 0.01 nm. In general this resolution is high enough to pick up fine structure in gas absorptions. In the UV below 300 nm, and in parts of the O_2A and O_2B bands, whole-atmosphere gas absorption optical depths can reach 50 or more, and the downward irradiance is nearly zero at the ground (Figure 2.2b). The inset in Figure 2.2b shows a close-up view of the fine structure in absorption optical depth for the O_2A band, with dual peaks centered at 0.761 μm and 0.764 μm, and a deep, narrow valley around 0.762 μm. Similarly, the continuum of water vapor absorption from the near-infrared to about 4 μm is also well simulated (Figure 2.2c). Also of note is the non-negligible absorption of SO_2 and NO_2 in UV and blue wavelength regions respectively (Figure 2.2d). In urban regions, high SO_2 and NO_2 can together contribute optical depths of around 0.03–0.07 (Figure 2.2d). Hence, in order to take advantage of low surface reflectance in the UV and the use of deep-blue wavelengths for the retrieval of AOD in urban regions, it is critical to treat absorption by SO_2 and NO_2. In contrast, calculations performed at moderate spectral resolution (such as those from Santa
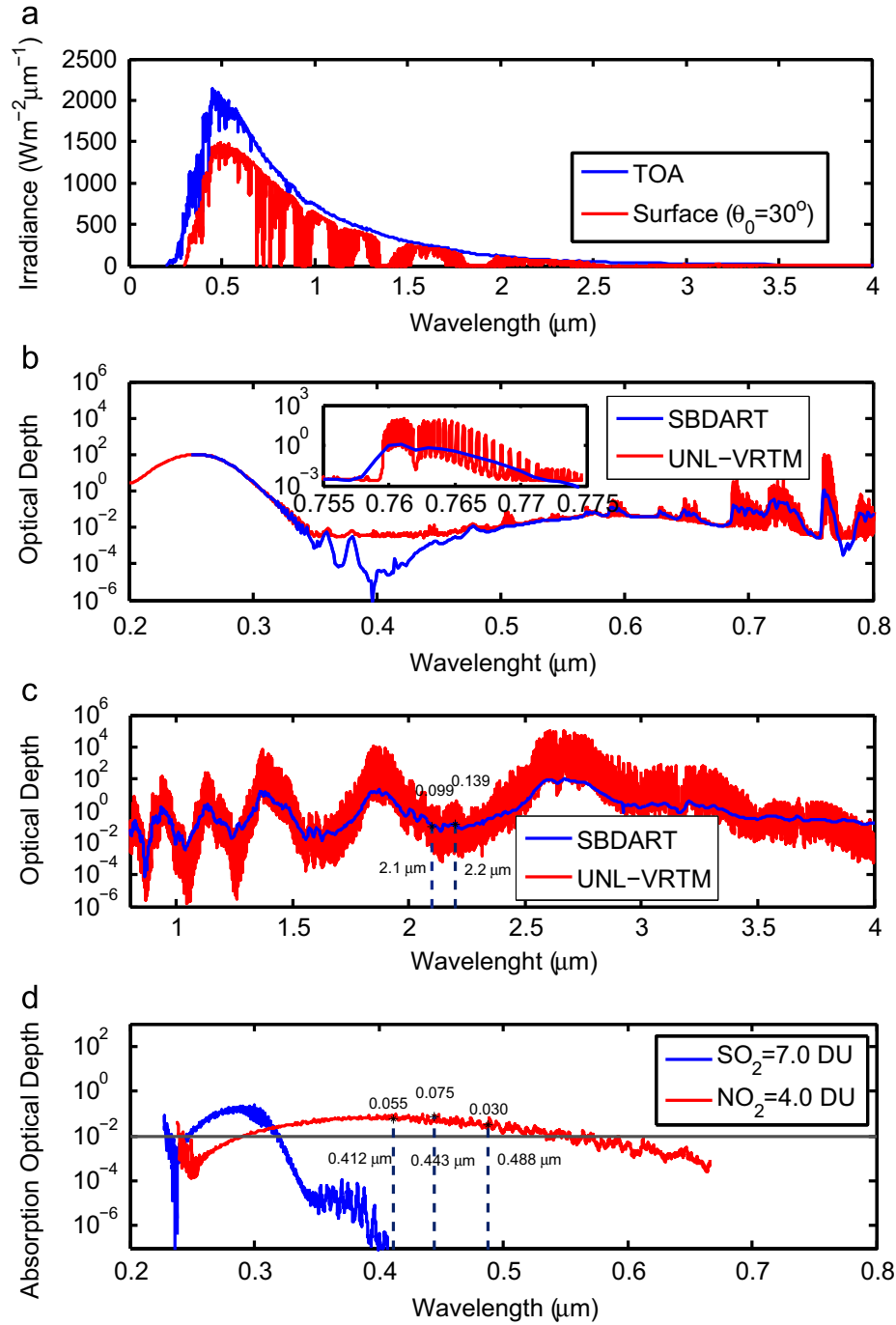
Figure 2.2: (a) Downward solar spectral irradiance at the TOA and the surface for solar zenith angle of 30°. (b) Total-atmosphere gas absorption optical depth in the range 0.2–0.8 μm. (c) Same as (b) but for 0.8–4 μm. (d) Optical depth of SO_2 and NO_2 in polluted cases. Also shown in (b) and (c) are the optical depth computed from Santa Barbara DISORT Atmospheric Radiative Transfer (SBDART) model [*Ricchiazzi et al.*, 1998]. The mid-latitude summer atmospheric profile is assumed [*McClatchey et al.*, 1972]. (Figure adopted from *Wang et al.* [2014])
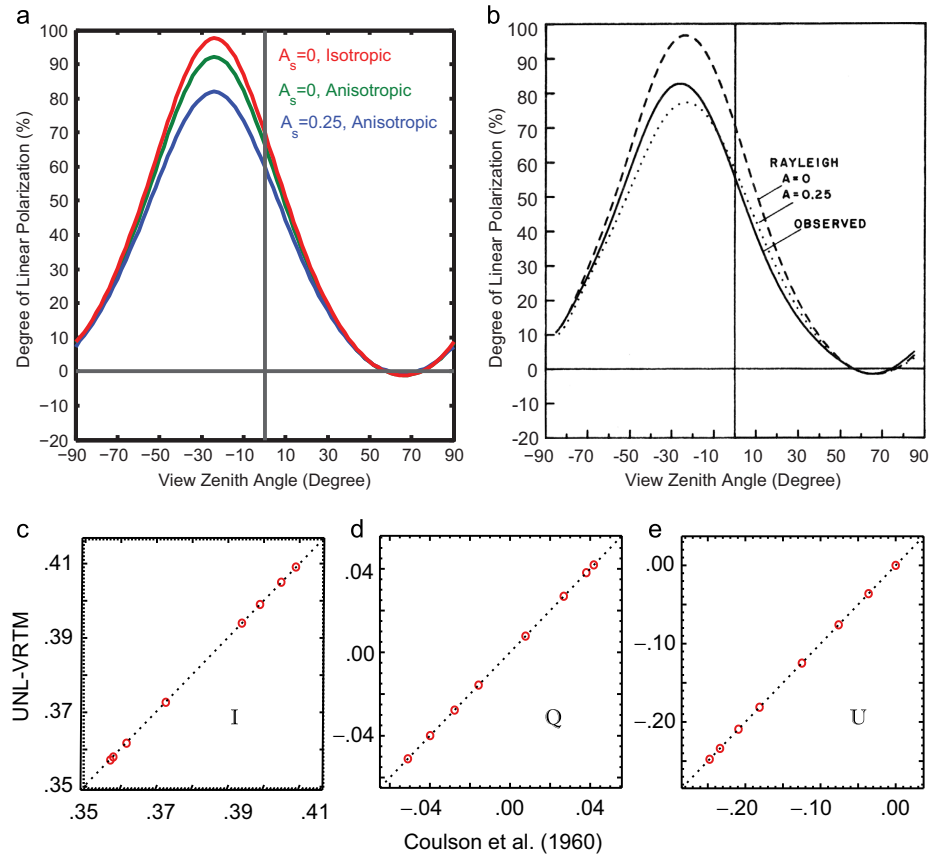
Figure 2.3: Degree of linear polarization ($-Q/I$) of downward radiation for a pure Rayleigh atmosphere: (a) computed by UNL-VRTM for the case analyzed in Figure 5.7 of *Coulson* [1988] and shown here as (b). (c)–(e) shows the comparisons of *I*, *Q*, and *U* computed by *Coulson et al.* [1960] and those from UNL-VRTM. In (a) and (b), As represents the surface albedo value. In (c) and (d), the calculation is for $\tau = 1.0$, surface albedo is 0.25, $\cos\theta_0 = 0.8$, and for 8 different viewing angles. (Figure adopted from *Wang et al.* [2014])

Barbara Discrete-Ordinate Atmospheric Radiative Transfer, or SBDART [*Ricchiazzi et al.*, 1998], shown as the blue lines in Figure 2.2b and c) do not resolve fine-structure details, sometimes missing the absorption lines for SO_2 or NO_2, and in general producing significant underestimation of optical depths in the O_2A band.

Figure 2.3 shows the calculation of the degree of linear polarization (DOLP) of downward radiation in a pure Rayleigh scattering atmosphere. The solid blue line in Figure 2.3a (dotted line in Figure 2.3b) reproduces the theoretical results shown in Figure 5.7 of *Coulson* [1988],
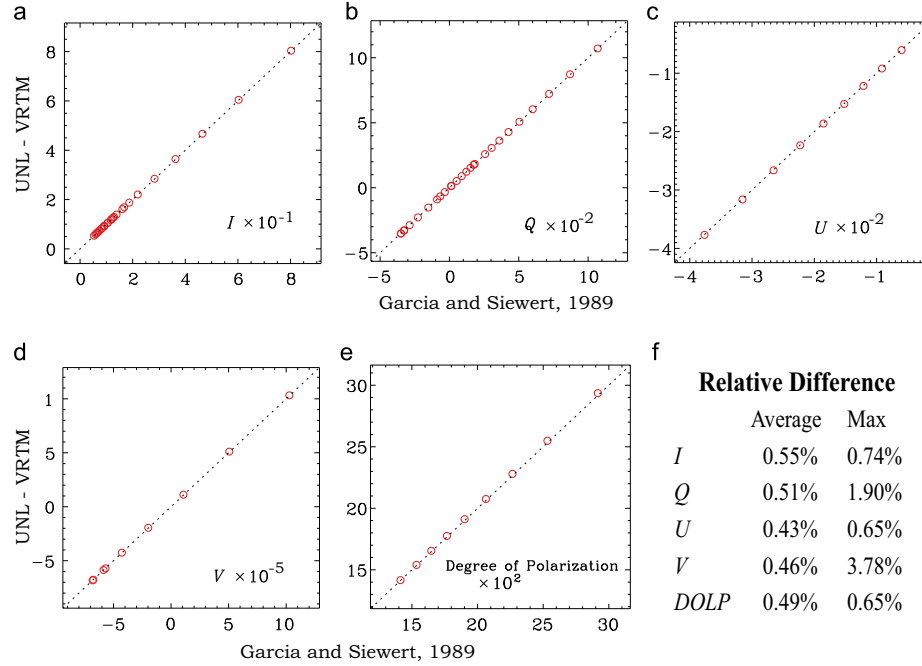
Figure 2.4: Counterparts in Tables 3–10 of *Garcia and Siewert* [1989] for upwelling radiation on the top of the same atmospheric conditions of aerosol scattering. No gas absorption and Rayleigh scattering are considered. Note that compared here are *I* and *Q* values reported in *Garcia and Siewert* [1989] for 9 view angles (with cosine values from 0.1 to 0.9 at equal spacing of 0.1) and 3 relative azimuth angles (0, $\pi/2$, and π), which yields a total of 27 data points. For *U* and *V*, their values are reported for the same 9 viewing angles but for one relative azimuth angle ($\pi/2$) only. The calculation is performed at wavelength of 951 nm and τ of 1.0, and aerosol size distribution parameters $r_{\text{eff}} = 0.2$, $v_{\text{eff}} = 0.07$, refractive index $m_{\text{r}} = 1.44$, and SSA of 0.99. (Figure adopted from *Wang et al.* [2014].)

which was used to interpret the DOLP measured at Mauna Loa Observatory on February 19, 1977. Furthermore, Figure 2.3a shows that the anisotropy in Rayleigh scattering reduces the peak DOLP by 5% (e.g., the difference between the green and red lines) at 0.7 μm. Surface reflection and its concomitant increase of atmosphere scattering will decrease the DOLP of downward radiation. An increase of surface reflectance from 0 to 0.25 decreases the peak DOLP by 10%.

Quantitatively, the Stokes-vector *I*, *Q*, and *U* components computed with UNL-VRTM differ from their counterparts found in the tables by *Coulson et al.* [1960] by average (relative)

deviations of 1.9×10^{-4} (0.05%), 2×10^{-5} (0.14%), and 4×10^{-5} (0.03%), respectively (Figure 2.3c–e). These differences are similar to the values 2.1×10^{-4}, 9×10^{-5}, and 4×7^{-5} identified by *Evans and Stephens* [1991]. More recently, Rayleigh-atmosphere benchmark results have been re-computed by *Vijay and Hovenier* [2012] to a much higher degree of accuracy; this work also included benchmarking of the VLIDORT model.

Figure 2.4 shows benchmark calculations of four Stokes parameters for radiative transfer in an aerosol-only atmosphere. *Garcia and Siewert* [1989] documented their results for unpolarized incident radiation at 951 nm and $cos\Theta_0$ of 0.2, for an atmosphere with a Lambertian reflectance of 0.1. The aerosols in that atmosphere were assumed to satisfy a gamma-function size distribution with r_{eff} of 0.2 μm and v_{eff} of 0.07, and a refractive index yielding an aerosol single scattering albedo of 0.99. Compared to their results, the Stokes parameters computed by UNL-VRTM show relative differences of less than 0.6%, with maximum relative differences (at certain viewing geometries) of up to 2% for Q and 3.8% for V. The DOLP computed from the UNL-VRTM (with 15 streams for the hemisphere) and documented by *Garcia and Siewert* [1989] (with 3 streams) differ on average by 0.5%, with a maximum relative difference of 0.65%.

The simultaneous calculation of analytic Jacobians of the four Stokes parameters with respect to the aerosol optical depth, size parameters, refractive indices, and aerosol-loading peak height for both fine and coarse model aerosols may be validated against Jacobians calculated using the finite difference method (Figures 2.5 and 2.6). Overall, results from the two methods are highly correlated as seen in the scatter plots shown in these figures. Relative differences in all comparisons are less than 0.5%, and in many cases the differences are less than 0.05%.
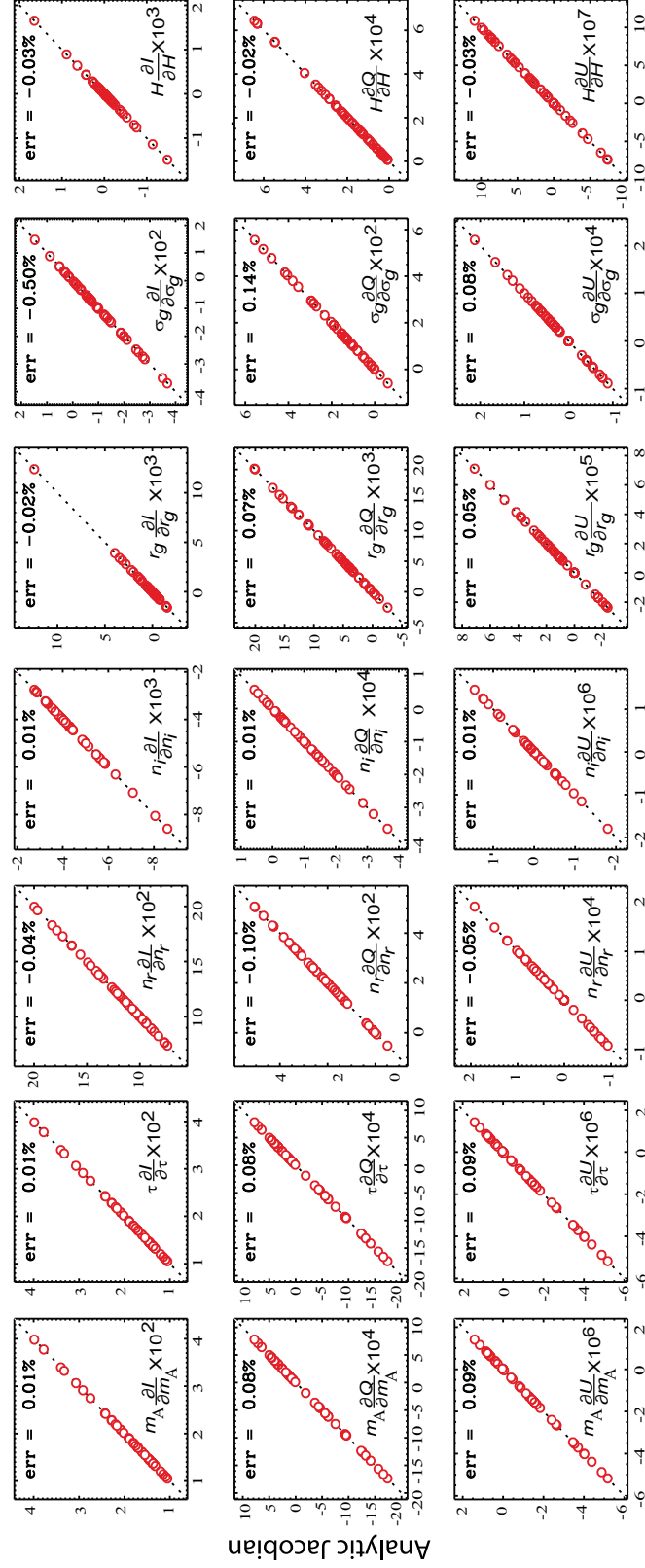
Figure 2.5: Intercomparison of Jacobians ($\partial \xi / \partial \ln x$) calculated with UNL-VRTM using the analytical method (y-axis) with those computed from UNL-VRTM using finite-difference estimates (x-axis). Here ξ is one of the Stokes parameters: I (top row), Q (middle row), and U (last row). x is one of 7 parameters associated with fine-mode aerosols: mass concentration m_A, τ_A, m_r, m_i, r_g and σ_g (of the lognormal PSD), and height (H) of peak aerosol concentration in the vertical. Note, the calculation is done for an atmosphere containing both fine- and coarse-mode aerosols as described in *Hess et al.* [1998]. (Figure adopted from *Wang et al.* [2014])
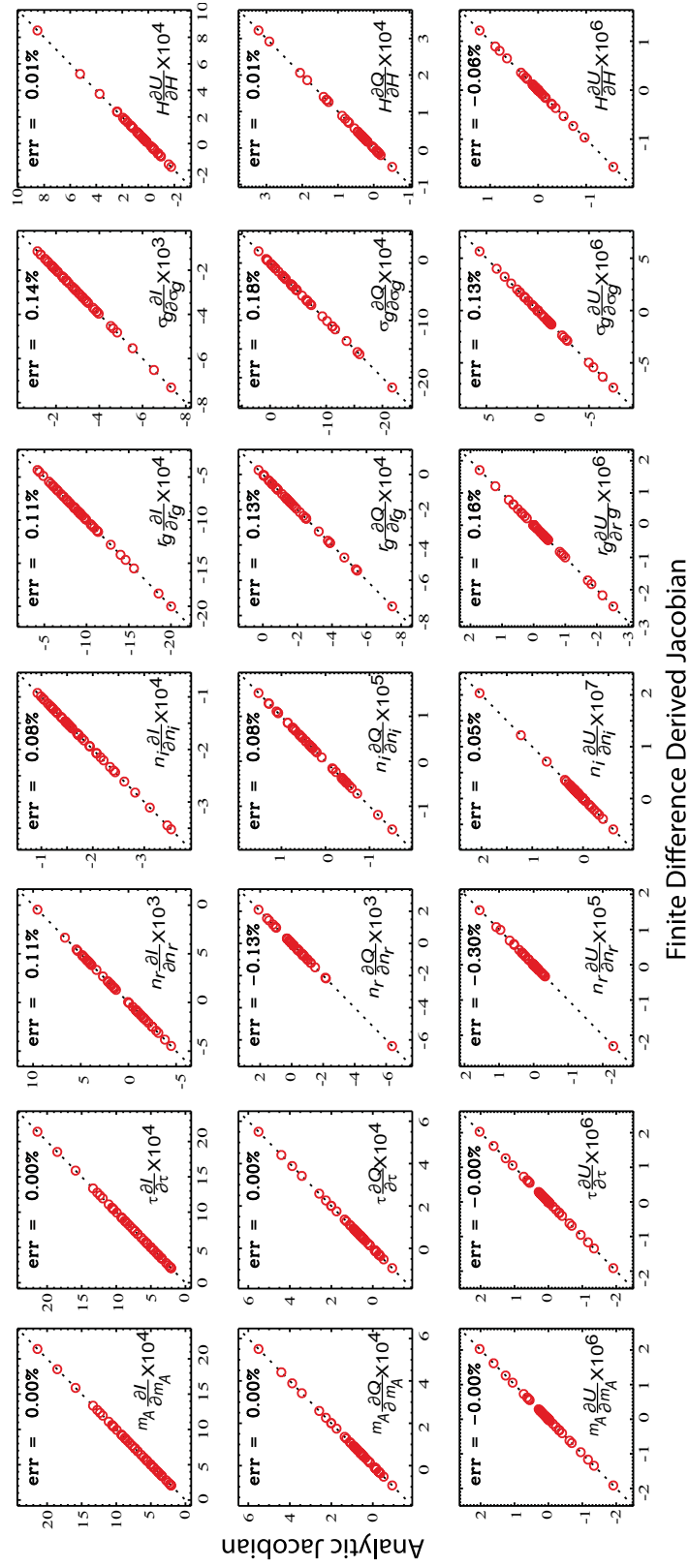
Figure 2.6: Same as in Fig. 5, but for coarse mode aerosols. (Figure adopted from *Wang et al.* [2014])

<div align="center">

CHAPTER 3

INVERSION THEORIES AND ALGORITHM

</div>

3.1 Introduction

To be filled ...

3.2 Inversion Theories

3.2.1 Maximum a posteriori solution of an inverse problem

Let $\mathbf{x}$ denote a state vector that contains n parameters to be retrieved (such as PSD parameters and complex indices of refraction), and $\mathbf{y}$ an observation vector with m elements of measurements (such as multi-band radiances from different viewing angles). Furthermore, let $\mathbf{F}$ indicate a forward model (such as the radiative transfer model) that describes the physics on how $\mathbf{y}$ and $\mathbf{x}$ are related. Then, we have

$$\mathbf{y} = \mathbf{F}(\mathbf{x}, \mathbf{b}) + \boldsymbol{\varepsilon}_y \tag{3.1}$$

where the vector $\mathbf{b}$ consists of forward model parameters (such as the surface reflectance) that are not included in $\mathbf{x}$ but quantitatively influence the measurement to our known, the $\boldsymbol{\varepsilon}_y$ term is the error that results from inaccurate modeling and measurement processes. In this study, we use the best-estimated $\hat{\mathbf{b}}$ in the forward model and consider its contributions to the

total measurement accuracy. Linearize the forward model at $\mathbf{b} = \hat{\mathbf{b}}$:

$$\mathbf{y} = \mathbf{F}(\mathbf{x}, \hat{\mathbf{b}}) + \hat{\mathbf{K}}_b + \boldsymbol{\varepsilon}_y \tag{3.2}$$

where $\hat{\mathbf{K}}_b$ is the weighting function (or Jacobian matrix) of forward model to model parameters $\mathbf{b}$ at $\hat{\mathbf{b}}$, $\left.\frac{\partial \mathbf{F}}{\partial \mathbf{b}}\right|_{\mathbf{b}=\hat{\mathbf{b}}}$. If we treat the forward model as linear in the vicinity of the true state of x, the forward model can be rewritten as:

$$\mathbf{y} = \mathbf{K}\mathbf{x} + \boldsymbol{\varepsilon} \tag{3.3}$$

Where $\boldsymbol{\varepsilon}$ represents the error that sums the errors from forward modeling and measurement processes. We only consider the errors propagated from errors in $\mathbf{b}$, but omit any other source in the forward modeling. Thus, $\boldsymbol{\varepsilon} = \boldsymbol{\varepsilon}_y + \hat{\mathbf{K}}_b \boldsymbol{\varepsilon}_b$, where $\boldsymbol{\varepsilon}_b = \mathbf{b} - \hat{\mathbf{b}}$ indicates error of $\hat{\mathbf{b}}$. K is the $m \times n$ Jacobian matrix comprising derivatives of the forward model with respect to each retrieved parameter, $\frac{\partial \mathbf{F}}{\partial \mathbf{x}}$.

The inverse problem is to solve $\mathbf{x}$ from the measurement $\mathbf{y}$ by inverting the forward model $\mathbf{F}$. In many situations, the forward model is a complex process with large number of internal uncertainties. As a result, the inverse problem tends to be an ill-posed problem. In this regard, the *a priori* constraints are usually considered. *A priori* represents the knowledge of the state before the measurement is made. And the true state occurs nearby the *a priori*:

$$\mathbf{x} = \mathbf{x}_a + \boldsymbol{\varepsilon}_a. \tag{3.4}$$

where $\mathbf{x}_a$ is the *a priori estimate* and $\boldsymbol{\varepsilon}_a$ indicates *apriori* error.

Then, the inverse problem becomes to solve the equation set (as illustrated in Figure
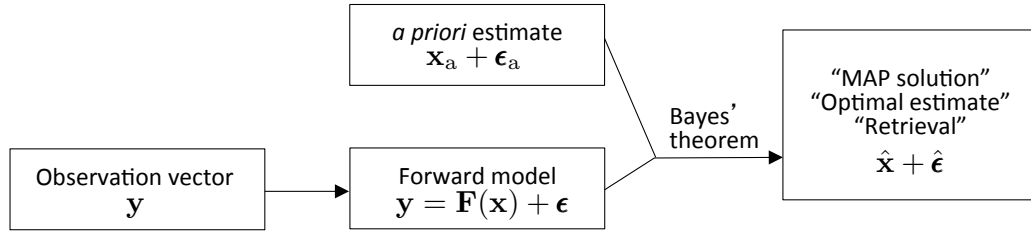
Figure 3.1: The concept of an inverse problem that optimzing an estimates from observations. (Courtesy: Daniel Jacobs)

3.1):

$$\begin{cases} \mathbf{y} = \mathbf{K}\mathbf{x} + \boldsymbol{\varepsilon} \\ \mathbf{x} = \mathbf{x}_a + \boldsymbol{\varepsilon}_a. \end{cases} \tag{3.5}$$

Provided that errors of measurements and the a priori are characterized by a Gaussian probability distribution function (PDF) and the forward model is linear in the vicinity of the true state, the maximum a posteriori (MAP) solution of the state vector, also called the retrieval or the a posteriori, can be derived with the Bayes's Theorem [*Rodgers*, 2000]:

$$\hat{\mathbf{x}} = \mathbf{x}_a + (\mathbf{K}^T \mathbf{S}_y^{-1} \mathbf{K} + \mathbf{S}_a^{-1})^{-1} \mathbf{K}^T \mathbf{S}_y^{-1} (\mathbf{y} - \mathbf{K}\mathbf{x}_a) \tag{3.6}$$

Here, $\mathbf{S}_a$ is the error covariance matrix of *a priori*, $\mathbf{x}_a$; $\mathbf{S}_y$ is the error covariance matrix of the measurements; T denote matrxi transpose operation.

The "retrieval", $\hat{\mathbf{x}}$, in above equation (3.6) is corresponding to the maximum posterior PDF and the minimum of a cost function defined by

$$J = (\mathbf{y} - \mathbf{K}\mathbf{x})^T \mathbf{S}_y^{-1} (\mathbf{y} - \mathbf{K}\mathbf{x}) + (\mathbf{x} - \mathbf{x}_a)^T \mathbf{S}_a^{-1} (\mathbf{x} - \mathbf{x}_a). \tag{3.7}$$

J is indeed the negative exponent term of the posterior PDF, which also follows a Gaussion

shape with the expected value of $\hat{\mathbf{x}}$ and the error covariance matrix $\hat{\mathbf{S}}$ given by

$$\hat{\mathbf{S}}^{-1} = \mathbf{K}^T \mathbf{S}_y^{-1} \mathbf{K} + \mathbf{S}_a^{-1}. \tag{3.8}$$

$\hat{\mathbf{S}}$ describes the statistical uncertainties in retrieved $\hat{\mathbf{x}}$ due to measurement noise, forward modeling uncertainty, and smoothing error [*Rodgers*, 2000]. The square roots of its diagonals are the one-sigma uncertainties of each retrieved parameters given the observation uncertainties, forward model uncertainties, and prior knowledge of the state. With $\hat{\mathbf{S}}$, we can also estimate the uncertainty for any parameter (for example, the aerosol single scattering albedo in this study) that can be fully determined by parameters (for example, aerosol refractive index and PSD parameters) in $\mathbf{x}$ but is not directly retrieved. If one parameter is a function defined by $\zeta = zeta\mathbf{x}$, then the uncertainty in derived ζ is [*Rodgers*, 2000]:

$$\hat{\varepsilon}_\zeta = \sqrt{\sum_{i=1}^{n} \sum_{i=1}^{n} \frac{\partial \zeta}{\partial x_i} \frac{\partial \zeta}{\partial x_j}}. \tag{3.9}$$

3.2.2 Information theory

The Jacobian matrix $\mathbf{K}$ usually serves as gradients in the sensitivity analysis and can be a useful indicator of information. For a linear system in the absence of measurement error, the rank of $\mathbf{K}$ indicates independent pieces of information that can be determined from the measurements. In practice, error inevitably presents in measurements and thus can impact the effective rank. To identify the effective sensitivity of individual measurement to each retrieved parameter, we define the error-normalized (EN) Jacobian matrix by

$$\tilde{\mathbf{K}} = \mathbf{S}_y^{-\frac{1}{2}} \mathbf{K} \mathbf{S}_a^{\frac{1}{2}} \tag{3.10}$$

$\tilde{\mathbf{K}}$ is also called the 'pre-whitening' by *Rodgers* [2000]. The superiority of the matrix

$\tilde{\mathbf{K}}$ over the matrix $\mathbf{K}$ is that it compares the observation error covariance ($\mathbf{S}_y^{\frac{1}{2}}$) with the natural variability of the observation vector as expressed by its prior covariance ($\mathbf{K}\mathbf{S}_a^{\frac{1}{2}}$). Any component whose natural variability is smaller than the observation error is not measurable. Therefore, an element $\tilde{\mathbf{K}}_{i,j}$ less than unity indicates that the measurement component y_i contains null useful information for determining parameter x_j. In contrast, when $\tilde{\mathbf{K}}_{i,j} > 1$, the larger of its value, the more useful information retained in y_i for determining x_j. Therefore, the $\tilde{\mathbf{K}}$ matrix provides not only sensitivity of individual measurements to each retrieved parameter, but also a capacity-metric for those observations to infer retrieved parameters.

The averaging kernel matrix has been widely used to quantify the information gained by making a measurement [e.g., *Rodgers*, 1998; *Hasekamp and Landgraf*, 2005a; *Frankenberg et al.*, 2012; *Sanghavi et al.*, 2012]. It provides the sensitivity of the retrieval to the true state and is defined by

$$\mathbf{A} = \frac{\partial \hat{\mathbf{x}}}{\partial \mathbf{x}}. \tag{3.11}$$

Replace y in equation (3.6) with equation (3.3) at $\mathbf{x} = \mathbf{x}_a$,

$$\hat{\mathbf{x}} = \mathbf{x}_a + (\mathbf{K}^T\mathbf{S}_y^{-1}\mathbf{K} + \mathbf{S}_a^{-1})^{-1}\mathbf{K}^T\mathbf{S}_y^{-1}[\mathbf{K}(\mathbf{x} - \mathbf{x}_a) + \boldsymbol{\varepsilon}] \tag{3.12}$$

Then we have

$$\mathbf{A} = \frac{\partial \hat{\mathbf{x}}}{\partial \mathbf{x}} = (\mathbf{K}^T\mathbf{S}_y^{-1}\mathbf{K} + \mathbf{S}_a^{-1})^{-1}\mathbf{K}^T\mathbf{S}_y^{-1}\mathbf{K} \tag{3.13}$$

Matrix $\mathbf{A}$ quantifies the ability of the retrieval to infer $\hat{\mathbf{x}}$ given the relationship between $\mathbf{y}$ and $\mathbf{x}$ (i.e., $\mathbf{K}$) and given the observation noise and a priori characterization. Thus, an identity matrix of A represents a perfect retrieval, while a null matrix of $\mathbf{A}$ indicates that none of the information can be gained from the observation. The trace of $\mathbf{A}$ is the degree of freedom for signal, i.e., $\mathrm{DFS} = \mathrm{Trace}(\mathbf{A})$, which represents independent pieces of information that the observation can provide. The diagonal elements of averaging kernel matrix $\mathbf{A}$, or the

DFS components, indicate the partial sensitivity of each individual retrieved parameters with respect to their corresponding truth:

$$\mathbf{A}_{i,i} = \frac{\partial \hat{x}_i}{\partial x_i} \tag{3.14}$$

Clearly, $\mathbf{A}_{i,i} = 1$ indicates that the observation is capable of fully characterizing the truth of x_i; while $\mathbf{A}_{i,i} = 0$ indicates the observation contains zero information on x_i and x_i is not measurable. From the formulation of $\hat{\mathbf{S}}$ and $\mathbf{A}$, we can conclude that only the error covariance and Jacobian matrix, but not the retrieval, are important for the purpose of understanding information content.

Other quantities used for information analysis of a measurement include the Shannon information content (SIC) [*Shannon*, 1948] and the Fisher information matrix. SIC, a widely used quantity [e.g., *Rodgers*, 1998; *Knobelspiesse et al.*, 2012], is defined as the reduction in entropy after the measurement

$$H = \frac{1}{2}\ln|\mathbf{S}_{\mathrm{a}}| - \frac{1}{2}\ln|\hat{\mathbf{S}}| = -\frac{1}{2}\ln|\hat{\mathbf{S}}\mathbf{S}_{\mathrm{a}}^{-1}| = -\frac{1}{2}\ln|\mathbf{I}_n - \mathbf{A}| \tag{3.15}$$

where $\mathbf{I}_n$ is an identity matrix of order n. Clearly, SIC is highly related to the DFS for the information analysis. In the Gaussian linear case, the Fisher information matrix is equal to the inverse of *a posteriori* error covariance matrix, $\hat{\mathbf{S}}^{-1}$. The retrieval indeed corresponds to the maximum of a posteriori PDF and the minimum of retrieval error. It is thus straightforward that higher level of the Fisher information is subject to a smaller retrieval error. Due to their close relationship with the DFS and $\hat{\mathbf{S}}$, we will not present the SIC and Fisher information analysis in this study.

3.3 New Research Algorithm for AERONET Inversion

Figure 3.2 gives an overview of the retrieval algorithm specifically designed for the analysis and inversion of photo-polarimetric remote sensing observations, such as those from AERONET. The algorithm builds upon the UNified and Linearized Vector Radiative Transfer Model (UNL-VRTM), which consists of seven component modules for the forward simulation of observations (section 2.2). The forward modeling includes the linearized vector radiative transfer model (VLIDORT) developed by *Spurr* [2006], a linearized Mie code and a linearized T-Matrix code calculating aerosol single scattering properties [*Spurr et al.*, 2012], a module calculating Rayleigh scattering and a module for gas absorption, plus a surface model computing bidirectional reflectance/polarization distribution function (BRDF/BPDF) [*Spurr*, 2004]. The required input parameters for the algorithm are the relevant atmospheric profiles (of pressure, temperature, and gaseous mixing ratio), aerosol loading in terms of AOD or aerosol columnar volume, aerosol vertical profiles, aerosol microphysical and chemical parameters (size distribution and complex refractive index), and surface reflection parameters. The users can specify up to two modes of the aerosol population. Each mode is characterized by the total particle number (or volume), the vertical profile, size distribution, and refractive index. The aerosol-related modules—Mie, T-matrix, and VLIDORT—are analytically linearized and fully coupled. Thus, the forward model not only simulates radiance and/or polarization for a given spectrum, but also computes the Jacobians of these radiation fields with respect to input aerosol microphysical parameters. Our inversion-oriented UNL-VRTM supplies these Jacobians together with observation error characterizations and *a priori* constraints to the statistical optimization procedure for the retrieval. Information content and error analysis are also included in the procedure along with the inversion. Although our algorithm is tailored to measurements from the AERONET SunPhotometer, its modularized framework enables the simulation and inversion
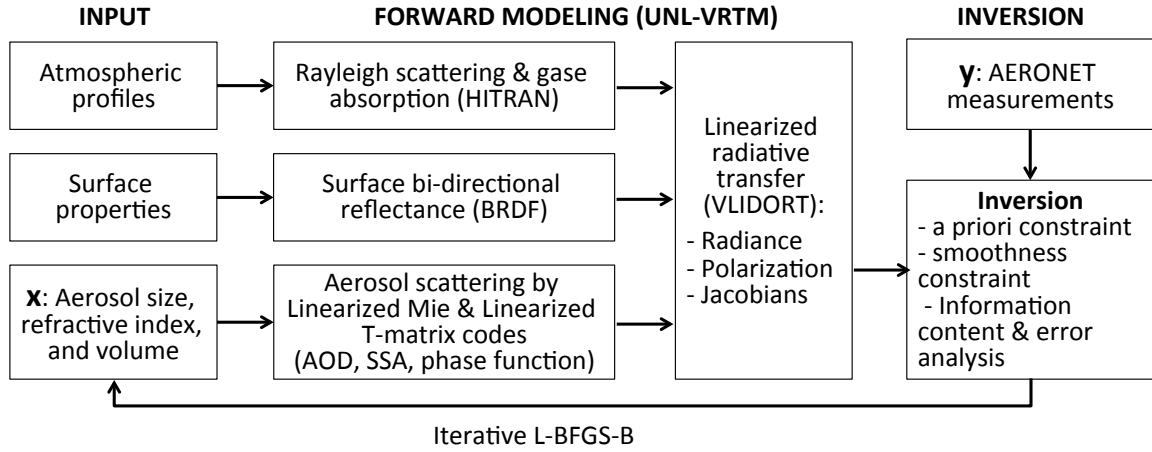
Figure 3.2: General structure of the new research inversion algorithm for the retrieval of aerosol microphysical parameters from AERONET photo-polarimetric measurements.

of observations from various platforms, including satellite sensors.

Development of the inversion component in our algorithm was built upon our experience with optimization of aerosol emissions using the adjoint chemistry transport model (CTM) [*Wang et al.*, 2012; *Xu et al.*, 2013]. In essence, the optimization method is consistent with the adjoint modeling that constrains aerosol emissions from measurements through inverting a CTM, although different physical processes are involved for inversion of AERONET observation. Both inversions seek the optimal solutions for a state vector that minimizes the differences between the model simulation and observation. In addition, our algorithm inherits the inversion strategy from the Dubovik00&06 algorithm, in particular with regard to the smoothness constraint on the spectral dependence of the complex refractive index.

3.3.1   Definition of state vector and Observation vector

For this study, the observation vector **y** comprises components from different sources. As listed in Table 3.1 (and Table 1.1 for specific measurements by the SunPhotometer), there are four categories of observations, i.e., the direct sun AOD, the sky radiance around the solar aureole, the sky radiance in the solar principal plane, and the DOLP in the solar principal

Table 3.1: AERONET observation characteristics.

Symbol	Parameter	Instrumental uncertainty	Other uncertainties
$\mathbf{y}_1$	Direct sun AOD	0.01–0.02	$\sim$0.02 spatial/temporal variation
$\mathbf{y}_2$	Sky radiance in solar almucantar	5%	Surface BRDF and BPDF
$\mathbf{y}_3$	Sky radiance in principal plane	5%	Surface BRDF and BPDF
$\mathbf{y}_4$	DOLP in principal plane	0.01	Surface BRDF and BPDF

plane, with all measurements performed at 440, 675, 870, and 1020 nm. Also indicated in Table 3.1 are the calibration errors and other measurement uncertainties that make of the term $\boldsymbol{\varepsilon}$.

The state vector x contains 11 pairs of parameters characterizing aerosol properties in the fine and the coarse modes, respectively, the columnar volume concentration V_0, the effective radius r_{eff}, the effective variance v_{eff}, and the complex refractive index $m_{\text{r}} - m_{\text{i}}i$ at 440, 675, 870, and 1020 nm (Table 3.2). r_{eff} and v_{eff} are two commonly used size parameters in the aerosol radiative quantification, because different types of size distribution function having same values of r_{eff} and v_{eff} possess similar scattering and absorption properties [*Hansen and Travis*, 1974]. In line with many studies [*Schuster et al.*, 2006; *Hasekamp and Landgraf*, 2005a, 2007; *Mishchenko et al.*, 2007; *Waquet et al.*, 2009], we assume the aerosol PSD follows a bi-modal lognormal function expressed in equation (2.10). All parameters include both the fine and coarse modes and account for a total of 22 elements ($n = 22$).

3.3.2 Combine a priori and smoothness constraints

A priori information describes our knowledge of the state vector before measurements are applied, and an *a priori* constraint is commonly used to achieve a well-defined stable and physically reasonable solution to an ill-posed problem. Usually, a priori knowledge comprises both a mean state $\mathbf{x}_{\text{a}}$ and its error $\boldsymbol{\varepsilon}_{\text{a}}$ (equation (3.4)). One of the satisfactory sources for the *a priori* knowledge is a climatology based on historical measurements. For a

Table 3.2: State vector elements and associated constraints for inversion.[a]

Symbol	Parameter	*a priori* constraint?	Smoothness constraint?
V_0^f, V_0^c	Columnar volume ($\mu m^3 \mu m^{-2}$)	$\checkmark$	
r_{eff}^f, r_{eff}^c	Effective radiance (μm)	$\checkmark$	
v_{eff}^f, v_{eff}^c	Effective variance	$\checkmark$	
$\mathbf{m}_r^f$, $\mathbf{m}_r^c$	Real part refractive index	$\checkmark$	$\checkmark$
$\mathbf{m}_i^f$, $\mathbf{m}_i^c$	Imaginary part refractive index	$\checkmark$	$\checkmark$

[a]The superscripts, 'c' and 'f', respectively denote fine and coarse aerosol modes. Refractive indices are for spectral wavelengths of 440, 675, 870, and 1020 nm.

given AERONET site, we use the available inversion products that have been obtained with the Dubovik00&06 algorithm, for which the *a priori* can be well characterized by the mean values and standard deviations of each component in the state vector. At the same time, the a priori can also be determined from other sources if historical AERONET retrieval is not available. For example, we could extract aerosol microphysical climatology from chemistry transport model simulations [e.g., *Wang et al.*, 2010] or from measurements of in situ and/or even satellite sensors.

Among those retrieved parameters, the aerosol volumes—V_0^f and V_0^c—are the most variable or uncertain quantities. A reasonable initial guess for these quantities could speed up the iterative inversion. Here, we "look up" their initial values from the AOD measurements at two spectral wavelengths. Given the *a priori* information on the aerosol PSD and refractive indices, the aerosol extinction efficiency Q_{ext} can be obtained for each fine and coarse mode with the Mie code. And the AOD is related to the V_0^f and V_0^c via equation:

$$\tau_A = \tau_A^f + \tau_A^c = \frac{3V_0^f Q_{ext}^f}{4r_{eff}^f} + \frac{3V_0^c Q_{ext}^c}{4r_{eff}^c}. \tag{3.16}$$

Clearly, applying the above equation to the AODs at any two spectral wavelengths, we can easily solve V_0^f and V_0^c.

For some parameters, the *a priori* estimates may be poorly known, but these parameters

behave smoothly with no sharp oscillations. For example, the aerosol refractive index usually does not vary rapidly over the visible to near-infrared spectral range. In this regard, a smoothness constraint could be a preferable addition. The technique of constraining a smooth solution was pioneered by *Phillips* [1962]; *Twomey* [1963], and has been successfully used to retrieve coherent aerosol size distributions [*Dubovik and King*, 2000] and atmospheric vertical profiles [*Twomey*, 1977]. The principle of the smoothness constraint is to restrain the degree of non-linearity of a certain physical parameter by limiting the values of its dth derivatives:

$$\mathbf{G_d} + \boldsymbol{\varepsilon}_\Delta = \mathbf{0} \tag{3.17}$$

where $\mathbf{G_d}$ is a differential matrix composed of coefficients for calculating the *d*th derivatives of $\mathbf{x}$ with respect to the dependent variable, and the vector $\boldsymbol{\varepsilon}_\Delta$ indicates uncertainties in these derivatives.

In particular, for constraining the dependence of the spectral refractive index with wavelength, the matrix $\mathbf{G_d}$ calculates the dth difference of the refractive index at four wavelengths (440, 675, 870, and 1020 nm). As discussed by *Dubovik and King* [2000], we assume a linear relationship between the logarithm of the refractive index and the logarithm of the wavelength: $m_r \sim \lambda^{-\alpha}$, and $m_i \sim \lambda^{-\beta}$. Further, the matrix $\mathbf{G_1}$ for the first difference (of either m_r or m_i of one mode) can be expressed as:

$$
\begin{aligned}
\mathbf{G_1} &= \begin{bmatrix} 1/\Delta\lambda_1 & 0 & 0 \\ 0 & 1/\Delta\lambda_2 & 0 \\ 0 & 0 & 1/\Delta\lambda_3 \end{bmatrix} \begin{bmatrix} -1 & 1 & 0 & 0 \\ 0 & -1 & 1 & 0 \\ 0 & 0 & -1 & 1 \end{bmatrix} \\
&= \begin{bmatrix} -1/\Delta\lambda_1 & 1/\Delta\lambda_1 & 0 & 0 \\ 0 & -1/\Delta\lambda_2 & 1/\Delta\lambda_2 & 0 \\ 0 & 0 & -1/\Delta\lambda_3 & 1/\Delta\lambda_3 \end{bmatrix}
\end{aligned} \tag{3.18}
$$

Here, $\Delta\lambda_1$, $\Delta\lambda_2$, and $\Delta\lambda_1$ are the denominators for the first-order differences in the logarithm, e.g., $\Delta\lambda_1 = \ln\frac{675}{440}$. As to $\boldsymbol{\varepsilon}_\Delta$, we assume errors in first differences of the refractive index following *Dubovik and King* [2000], i.e., 0.2 for m_r and 1.5 for m_i.

Similar to the approach suggested by *Dubovik and King* [2000], we use multiple *a priori* constrains in the retrieval. Specifically, we combine the *a priori* constraint of equation (3.4) and the smoothness constraint of equation (3.17); our inverse problem is equivalent to solving the following set of three equations (in contast to (3.5) that has two equations):

$$\begin{cases} \mathbf{y} = \mathbf{F}(\mathbf{x}) + \boldsymbol{\varepsilon} \\ \mathbf{x} = \mathbf{x}_a + \boldsymbol{\varepsilon}_a \\ \mathbf{0} = \mathbf{G}_d + \boldsymbol{\varepsilon}_\Delta. \end{cases} \tag{3.19}$$

3.3.3 Statistical optimized inversion

Under the assumption of Gaussian-distributed errors, the optimized solution of equation (3.19) according to the MAP method corresponds to the state vector that minimizes the quadratic cost function consisting of multiple terms [*Dubovik and King*, 2000; *Dubovik*, 2004]:

$$J(\mathbf{x}) = \boldsymbol{\gamma}_y [\mathbf{y} - \mathbf{F}(\mathbf{x})]^T \mathbf{S}_y^{-1} [\mathbf{y} - \mathbf{F}(\mathbf{x})] + \boldsymbol{\gamma}_a (\mathbf{x} - \mathbf{x}_a)^T \mathbf{S}_a^{-1} (\mathbf{x} - \mathbf{x}_a) + \boldsymbol{\gamma}_\Delta \mathbf{x}^T \boldsymbol{\Omega}\mathbf{x}. \tag{3.20}$$

where $\boldsymbol{\Omega}$ is a smoothing matrix related to $\mathbf{G}_d$ and the error covariance matrix $\mathbf{S}_\Delta$ (of the dth derivatives of $\mathbf{x}$) by $\boldsymbol{\Omega} = \mathbf{G}_d^T \mathbf{S}_\Delta^{-1} \mathbf{G}_d$. The vectors $\boldsymbol{\gamma}_y$, $\boldsymbol{\gamma}_a$, and $\boldsymbol{\gamma}_\Delta$ are regularization parameters. In principle, the minimization of three-term cost function given by the equation (3.20) is conceptually analogous to the minimization of bi-component cost functions (3.7) generally considered in the Bayesian approach [*Rodgers*, 2000]. These three terms on

the right-hand size of equation (3.20) represent, respectively, (1) the total squared fitting error incurred owing to departures of the model predictions from the observations, (2) the penalty error incurred owing to departures of the estimates from the a priori, and (3) the penalty error incurred owing to departures from the defined smoothness feature. Overall, the minimization of $J(\mathbf{x})$ achieves the objective of improving the agreement between the model and the measurements while ensuring that the solution remains within a reasonable range and degree of smoothness.

The regularization parameters in the calculation of $J(\mathbf{x})$ act as weights to balance the fitting error and the penalty errors. Clearly, a good assignment of $\boldsymbol{\gamma}$ is of crucial importance for the statistical optimal solution. High values of $\boldsymbol{\gamma}_a$ and $\boldsymbol{\gamma}_\Delta$ can lead to over-smoothing of the solution with little improvement to the fitting residuals, while low values minimize the error term at the cost of greatly increasing the parameter penalty terms. Optimal values of $\boldsymbol{\gamma}$ for two-term cost functions can be identified at the corner near the origin of the so-called L-curve [*Hansen*, 1998]. However, such approach is not appropriate to the multi-term cost function. In this study, we assume equal weights for observational constraint term and combined *a priori* constrain terms in the cost function:

$$\boldsymbol{\gamma}_a = \frac{1}{2} n^{-1} \mathbf{e}, \quad \boldsymbol{\gamma}_\Delta = \frac{1}{2} (n_\Delta - d)^{-1} \mathbf{e}, \quad \boldsymbol{\gamma}_y = \left\langle \frac{1}{4m_k} \right\rangle_{k=1,4} \tag{3.21}$$

Here, d is the order of difference, $\mathbf{e}$ is a vector consisting of n elements of 1, and n_Δ is the number of state elements that are supplied with smoothness constraints. Values for $\boldsymbol{\gamma}_y$ are chosen to control the fitting residuals for observations of four different categories as listed in Table 3.1. Each group comprises the number of m_k observations for k from 1 to 4. The corresponding elements of $\boldsymbol{\gamma}_y$ for the kth group are $\frac{1}{4m_k}$, which means the observation quadratic term is normalized by the observation count of each group.

In principle, solving this inverse problem is tantamount to a pure mathematical mini-

mization procedure. The minimization of $J(\mathbf{x})$ equation (3.20) is performed with an iterative quasi-Newton optimization approach using the L-BFGS-B algorithm [*Byrd et al.*, 1995; *Zhu et al.*, 1994], which offers bounded minimization to ensure the solution stays within a physically reasonable range. The L-BFGS-B algorithm requires knowledge of $\mathbf{x}_a$ and $J(\mathbf{x})$, as well as the gradient of $J(\mathbf{x})$ with respect to $\mathbf{x}$, or $\nabla_{\mathbf{x}} J$. By linearizing the forward model F(x), we can determine $\nabla_{\mathbf{x}} J$ by

$$\nabla_{\mathbf{x}} J(\mathbf{x}) = \boldsymbol{\gamma}_y \mathbf{K}^T \mathbf{S}_y^{-1} [\mathbf{y} - \mathbf{F}(\mathbf{x})] + \boldsymbol{\gamma}_a \mathbf{S}_a^{-1} (\mathbf{x} - \mathbf{x}_a) + \boldsymbol{\gamma}_\Delta \boldsymbol{\Omega} \mathbf{x}. \tag{3.22}$$

Here, the Jacobian matrix $\mathbf{K}$ is computed analytically by the UNL-VRTM (section 2.2) through equations (2.15) and (2.16). At each iteration, improved estimates of the state vector are implemented and the forward simulation is recalculated. The convergence criterion to determine the optimal solution is the smallness of the reduction of $J(\mathbf{x})$ and the norm of $\nabla_{\mathbf{x}} J(\mathbf{x})$. The iteration stops when the reduction of $J(\mathbf{x})$ is less than 1% within 10 continuous iterations. Then, the optimal solutions are identified corresponding to the smallest norm of $\nabla_{\mathbf{x}} J(\mathbf{x})$ from these 10 last iterations. In addition, to ensure a physically reasonable solution, we also perform retrieval error analysis, and impose a practical quality control on real measurements.

3.3.4 Retrieval Error Characertization

The retrieval without error characterization is of significantly lesser value. Once the retrieval is achieved, the retrieval error can be characterized by the *a posteriori* state, and the error analysis can be performed in terms of a linearization of the problem around the solution $\hat{\mathbf{x}}$. We estimate the retrieval error on each state vector element using the error covariance

matrix of the *a posteriori* state:

$$\hat{\mathbf{S}}^{-1} = \hat{\mathbf{K}}^T \mathbf{S}_y^{-1} \hat{\mathbf{K}} + \mathbf{S}_a^{-1} + \mathbf{\Omega}. \tag{3.23}$$

where $\hat{\mathbf{K}}$ is the Jacobian matrix of the forward model $\mathbf{F}(\mathbf{x})$ at the solution $\hat{\mathbf{x}}$. It should be noted that the above three-term a posteriori formularized according to the three-term cost function defined in the equation (3.20). Simply, the retrieval error for each element can be estimated by:

$$\hat{\varepsilon}_i = \hat{\mathbf{S}}_{i,i}^{\frac{1}{2}} \tag{3.24}$$

With $\hat{\mathbf{S}}$ applied to equation (3.9), we can also estimate the uncertainty in parameters (such as ω_A and asymmetry factor in this study) that can be fully determined by the parameters in $\mathbf{x}$ but are not themselves directly retrieved.

3.3.5   Qaulity Control of Measurements

We apply a suite of quality criteria to ensure (a) a cloud-free condition, (b) that aerosol particles are quasi-homogeneously distributed in the horizontal plane within the scanning region, and (c) the measurements are densely populated and cover a wide range of scattering angles so that they provide sufficient information to retrieve all parameters falling within specified uncertainty levels. More specifically, these criteria are as follows: (i) the number of AOD observations ≥ 2 within a ± 25-minute centered at the period of a full scan sequence; (ii) sky radiance observations are excluded when the scattering angle is less than $3.2°$ and DOLP observations are excluded when the scattering angle is smaller than $5°$; (iii) a symmetry check for the almucantar radiances: the difference is less than 5% for the azimuthal angle of $180°$ and less than 10% elsewhere; and (iv) principal-plane observations are discarded when their second derivatives with respect to the scattering angle are beyond smoothing threshold.

Although most of these criteria follow *Holben et al.* [2006], we also check the smoothness of the principal-plane radiances and DOLP to identify scans that are contaminated by cloud. We apply the threshold on the second derivative of radiance (or DOLP) with respect to scattering angle in order to restrain local oscillations of radiance (or DOLP) caused by clouds or heterogeneous aerosol plumes. Thus, applying such a threshold can effectively remove sharp kinks and ensure continuous quantities in the principal-plane scanning sequences. Indeed, this smoothness check share the same principle to the smoothness constraint presented in the section 3.3.2.

CHAPTER 4

INFORMATION CONTENT ANALYSIS

4.1 Introduction

The AERONET collects not only the multi-spectral and multi-angular radiance observations, but also the state of light polarization from various viewing angles over many sites (section 1.1.2). Unfortunately, the potential of AERONET polarization measurements in retrieving aerosol microphysical parameters has not been fully exploited. Polarization measurements contain valuable information about aerosol microphysical properties [*Mishchenko and Travis*, 1997; *Cairns et al.*, 1997], as the polarization of light is highly sensitive to the aerosol size and refractive index [*Hansen and Travis*, 1974]. Several studies have emphasized the usefulness of the polarimetric observations taken by the ground-based instruments [*Cairns et al.*, 1997; *Boesche et al.*, 2006; *Emde et al.*, 2010; *Zeng et al.*, 2008]. *Vermeulen et al.* [2000] presented a two-step method to retrieve aerosol microphysical properties from polarized radiances: first, the single scattering albedo and the natural and polarized phase functions were retrieved from transmission and almucantar radiances and polarization in the principal plane; second, the aerosol PSD and refractive index were then derived. With the current AERONET inversion algorithm, *Dubovik et al.* [2006] conducted a case study using polarization data in a UAE[2] (Unified Aerosol Experiment-United Arab Emirates) field campaign [*Reid et al.*, 2008]. *Li et al.* [2009] extended the inversion algorithm of *Dubovik et al.* [2006] to include multi-spectral polarization and demonstrated improved retrievals in

real part aerosol refractive index for fine particles and the fraction of spherical particles.

However, questions regarding the use of AERONET polarimetric observations for retrieving aerosol microphysical parameters remain unresolved: (1) Practically, do the existing AERONET photo-polarimetric measurements have any potential to improve the retrieval of aerosol information content that we now routinely obtain from radiance measurement only? and (2) Hypothetically, how can future upgrades of AERONET photo-polarimetric measurements and inversion algorithm maximize the retrieval information content of aerosols? Answering these two questions is not only relevant to the future AERONET instrumentation design, but also for the ground-based passive polarimetric remote sensing of aerosols in general.

In this chapter, we seek to answer above questions from a theoretical perspective (section 3.2.2) by investigating the available information contained in the AERONET measurements with and without the inclusion of polarization data. This investigation is to provide the a theoretical foundation to support actual algorithm development for using polarimetric data for aerosol retrievals. The structure of this chapter is as follows. In section 4.2, we describe the experimental design on the aerosol models, error characteristics of *a priori* and AERONET measurements. Section 4.3 presents the results of information content and error analysis. In section 4.4, we investigate the sensitivity of retrieval uncertainties in aerosol parameters with respect to the aerosol loading and fine/coarse aerosol characteristics.

Table 4.1: The aerosol parameters defined for both fine and coarse aerosol modes[a].

Mode	$r_{\text{eff}}(\mu m)$	v_{eff}	$\mathbf{m}_r$	$\mathbf{m}_i$	ω_A
Fine	0.21 (80%)	.25 (80%)	1.44, 1.44, 1.43, 1.42 (.15)	.009, .011, .012, .011 (.01)	.95, .93, .92, .91
Coarse	1.90 (80%)	.41 (80%)	1.56, 1.55, 1.54, 1.54 (.15)	.004, .003, .003, .002 (.005)	.84, .91, .93, .96

[a]The complex refractive index $\mathbf{m}_r - \mathbf{m}_i i$, and single scattering albedo ω_A are reported at 440, 675, 870, and 1020 nm. Bracketed values are assumed a priori error in relative for r_{eff} and v_{eff} and in absolute for $\mathbf{m}_r$, $\mathbf{m}_i$, and ω_A.

Finally, we summarize in section 4.5 the general findings of this study and implications for practical algorithm development.

4.2 Experimental Design

4.2.1 *a priori* characteritics

The state vector **x** comprises 22 (11 pairs) retrieved parameters, namely, the columnar volume concentration V_0, the effective radius r_{eff}, the effective variance v_{eff}, and the complex refractive index $m_r + m_i i$ at 440, 675, 870, and 1020 nm (section 3.3.1). These 11 pairs of parameters charcterizing aerosol properties in the both fine and coarse aerosol modes; each mode follows a lognormal PSD function. Table 4.1 displays aerosol size parameters, refractive indices, and single scattering albedo for each size mode adopted for error and information analysis; also showed in brackets are their associated *a priori* uncertainties. The fine-mode particles are corresponding to water-soluble aerosols obtained from OPAC database [*Hess et al.*, 1998] with updates by *Drury et al.* [2010], while the coarse-mode is preassembly for large spherical particles with refractive index from *Patterson et al.* [1977]; *Wagner et al.* [2012].

In order to include various atmospheric conditions, we simulate three types of aerosols—each with different relative percentage between the coarse and fine modes—(I) fine particles

Table 4.2: The aerosol scenarios adapted for numerical experiments[a].

Aerosol type	V_0	fmf_v	τ_A	fmf_τ	AE	ω_A
Fine-dominated	.15	.8	1.0, .58, .36, .25	.97, .95, .92, .88	1.5	.95, .93, .92, .91
Well-mixed	.22	.5	1.0, .61, .41, .32	.90, .83, .74, .65	1.3	.94, .93, .92, .93
Coarse-dominated	.43	.2	1.0, .71, .57, .50	.69, .55, .42, .32	.82	.91, .92, .92, .94

[a]Values for τ_A, ω_A, and fmf_τ are listed respectively for spectral wavelength of 440, 675, 870, and 1020 nm. The AE is reported between 440 and 870 nm. V_0 is in the unit of $\mu m^3 \mu m^{-2}$
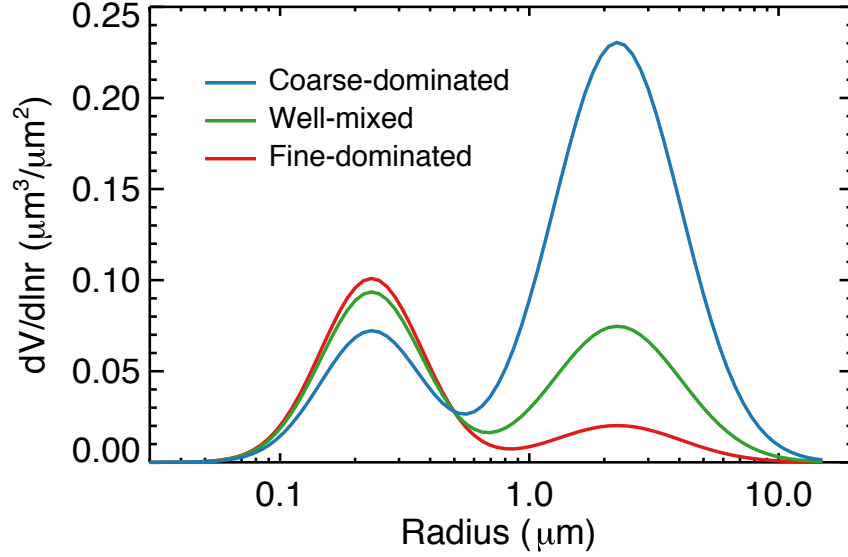
Figure 4.1: Volume size distribution for the aerosol types adopted for the information analysis. Relevant aerosol parameters are summarized in the Tables 4.1 and 4.2.

dominated, (II) well mixed, and (III) coarse particles dominated. As listed in Table 4.2 and illustrated in Figure 4.1, fine-mode fractions in terms of volume (fmf_v) are defined as 0.8, 0.5, and 0.2 for these three types, respectively. Aerosol volumes are scaled as necessary to maintain a normalized AOD at 440 nm corresponding to a moderate hazy condition ($\tau_{440} = 1.0$). The spectral aerosol optical depths τ_A, single scattering albedo ω_A, and the Ångström exponent (AE) are calculated and also shown in Table 4.2.

4.2.2 Synthetic observations

As described in section 1.1.2 and Table 1.1, The SunPhotometer equipped at AERONET sites routinely measures direct and diffuse (sky) solar radiances and optionally the mono-band light polarization [*Holben et al.*, 1998]. Recently, multi-spectral polarizations have also been taken with a newer-generation SunPhotometer (CIMEL CE318-DP) at some sites [*Li et al.*, 2009] and the UAE[2] fields campaign *Reid et al.* [2008]. Here we focus our study on using multi-spectral polarizations for the inversion of aerosol parameters.

Table 4.3: List of scenarios of AERONET observations used for information content analysis.

Scenario	Observations included[a]	Remark
I1	τ_A, and I_{alm}	Observations used in Dubovik00&06 algorithm
I2	τ_A, I_{alm}, and I_{pp}	Scenario I1 plus principal-plane radiances
P1	τ_A, I_{alm}, I_{pp} and $DOLP_{pp}$	Scenario I2 plus principal-plane polarization
P2	τ_A, I_{alm}, and $DOLP_{alm}$	Scenario I1 plus almucantar polarization

[a]Variables are for four spectral wavelengths, i.e., 440, 675, 870, and 1020 nm.

In order to investigate the merit of synergizing various observations in the inversion, we define four different scenarios of observation vectors, i.e., I1, I2, P1, and P2 as summarized in the Table 1. The observation vector in scenario I1 comprises direct sun AODs and solar almucantar radiances (I_{alm}) at 440, 675, 870, and 1020 nm. Scenario I2 includes measurements in scenario A and the total radiances (I_{pp}) at the same four wavelengths observed in the solar principal-plane. Observations in scenario P1 are defined to further include $DOLP_{pp}$ at those four wavelengths. Lastly, scenario P2 observations comprise basic measurements in scenario I1 plus almucantar polarization ($DOLP_{alm}$) at same wavelengths. The $DOLP_{alm}$ is not routinely measured by any current SunPhotometer, but we include it for a comparative analysis. Measurements defined in scenario I1 represent observations used by the current AERONET operational inversion and thus serves as a control experiment. From scenario I2, we can investigate the synergy of radiances in both the solar almucantar and solar principal-plane. Scans in the solar principal-plane can achieve larger scattering angles and thus may contain additional scattering information. And with scenarios P1 and P2 we will be able to evaluate the potential of adding polarization in the inversion.

We exclude I_{ppl} (Table 1.1) in our analysis because sky radiance in the solar principal plane can be also obtained during the polarization scan (I_{pp}). I_{ppl} and I_{pp} are different in the viewing-angle sequences, but they generally share a similar range of scattering angles. Thus, one is redundant for the other. We also exclude analysis for monochromatic polarization (at 870 nm) current measured on many AERONET sites, because single-band polarization

measurements contain much less information than multi-band ones and newer generation SunPhotometers with multi-band polarization capacity will be deployed at more AERONET sites.

4.3 Results

Following the approach stated in section 3.2, we have simulated the AERONET photo-polarimetric measurements under various solar zenith angles from $40°$ to $75°$ for the three defined aerosol types (Table 4.2). The simulated radiances (I_{alm}) on the solar almucantar plane and the degree of linear polarization ($DOLP_{pp}$) on the solar principal plane are illustrated in Figure 4.2 for aerosols of type II with solar zenith angle of $55°$. These simulations for other aerosol types and other solar zenith angles are of similar pattern. According to Figure 4.2a, I_{alm} decreases as the scattering angle increases, resulting from forward-dominated scattering phase function of aerosol particles. The maximum $DOLP_{pp}$ takes place at the scattering angle of $90°$ as a result of composite effect of Rayleigh and aerosol scattering, while the smaller $DOLP_{pp}$ values dominates at the small scattering angles because of the predominance of diffracted light (Figure 4.2b). With the synthetic data and relevant error characterizations, we have computed the EN Jacobian matrix, DFS, and a posteriori error to evaluate the capacity of AERONET measurements in inferring aerosol microphysical properties. Our analysis mainly focuses on the comparison of those quantities between measurements with and without including polarization, so that we can understand the importance of adding polarization for the retrieval.

4.3.1 Error-normalized (EN) Jacobian matrix

We compare the EN Jacobians for the I_{alm} and $DOLP_{pp}$ in both Figure 4.3 and Figure 4.4 to disclose the importance of $DOLP_{pp}$ measurements to the retrieval. Distinct patterns of
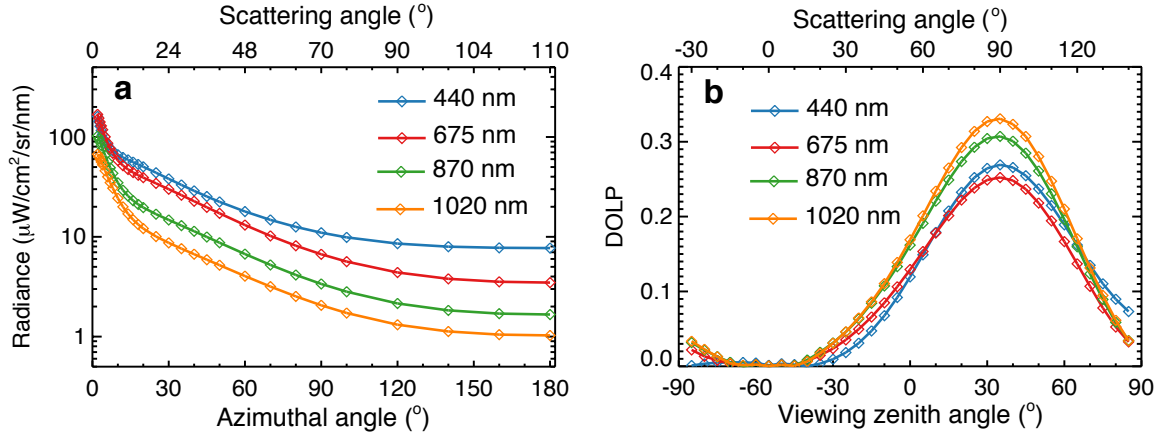
Figure 4.2: (a) Simulated radiances in the solar almucantar plane as a function of azimuth angle. (b) Simulated degree of linear polarization (DOLP) in the solar principal plane as a function of view zenith angle. Simulations are for the well-mixed aerosol type with columnar AOD of 1.0 at 440 nm as shown in the Table 4.2. Solar zenith angle is $55°$ and top abscissas show corresponding scattering angles.

EN Jacobians can be found between the $DOLP_{pp}$ and I_{alm} over the scattering angle. As shown in Figures 4.3a and 4.4a, the radiance at scattering angles less than $\sim10°$ decreases with increasing fine-mode aerosol loading (e.g. negative $\partial I_{alm}/\partial V_0$) and increases with increasing coarse-mode aerosol loading (e.g. positive $\partial I_{alm}/\partial V_0$), whereas the sensitivity of the I_{alm} to V_0 at larger scattering angles is larger positive in the fine mode and less positive in the coarse mode. It is because large particles scatter more radiation than small particles at near-forward scattering angles [*van de Hulst*, 1981]. In contrast, the $DOLP_{pp}$ presents profound sensitivity to the V_0 of aerosol in both modes at the scattering angles between $45°$ and $135°$ (Figures 4.3f and 4.4f).

Furthermore, the EN Jacobians of I_{alm} and $DOLP_{pp}$ can also be synergized in terms of their variations on the spectral wavelength. For example, the EN Jacobians for I_{alm} with respect to the fine-mode V_0 express lowest at 440 nm (blue curve in Figure 4.3a), but those for $DOLP_{pp}$ at 440 nm (blue curve in Figure 4.3f) are largest ones among these four spectral bands. Indeed, variations of these sensitivities with wavelength are mainly determined by
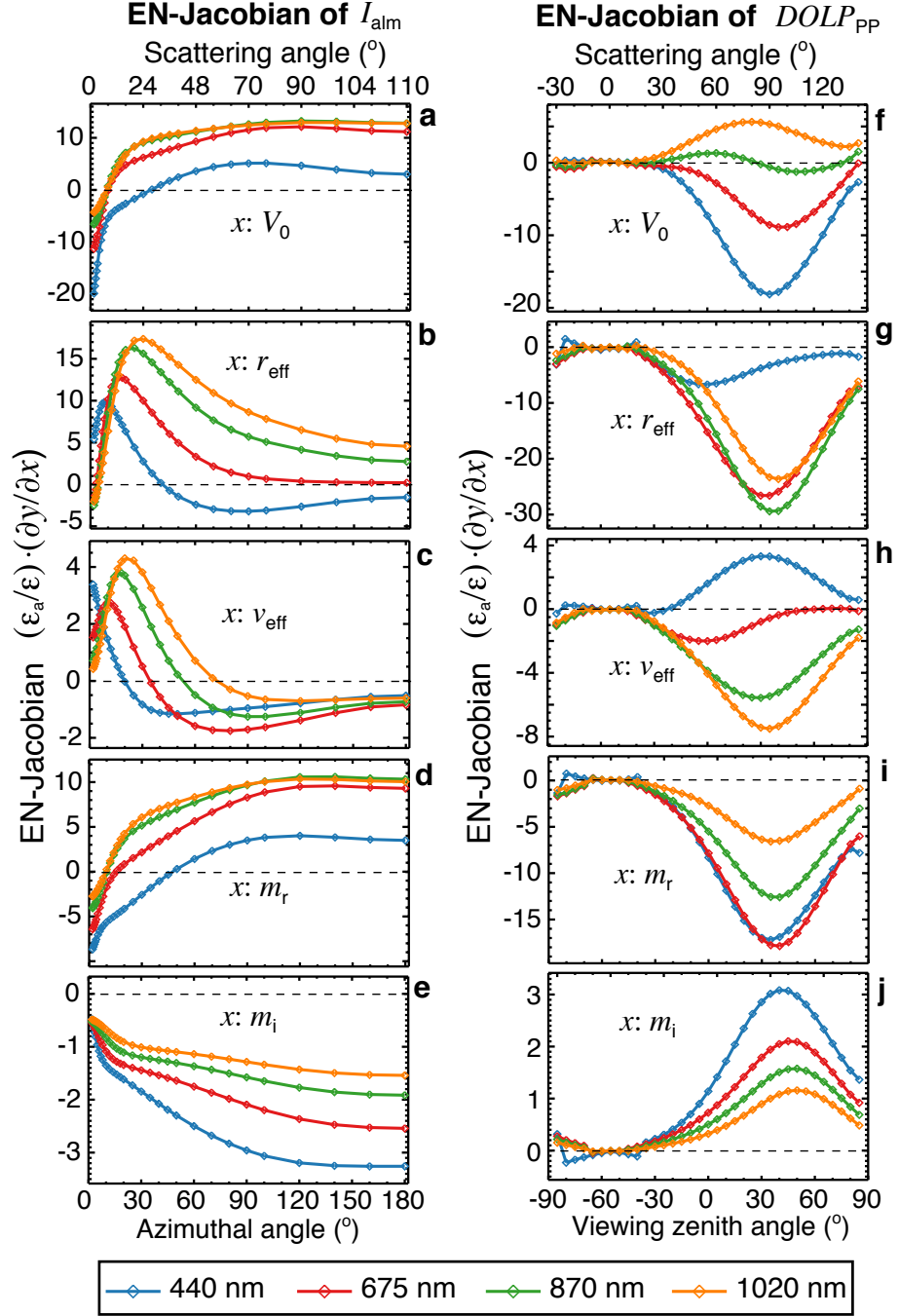
Figure 4.3: Error-normalized Jacobians of almucantar radiances I_{alm} (left column) and degree of linear polarization $DOLP_{pp}$ (right column) with respect to retrieved aerosol parameters in the *fine* mode: (a, f) V_0, (b, g) r_{eff}, (c, h) v_{eff}, (d, i) m_r, and (e, j) m_i. Simulations use type-II aerosols with columnar AOD of 1.0 at 440 nm and solar zenith angle of $55°$. The top and bottom abscissas are respectively the scattering angle and SunPhotometer scanning geometries.
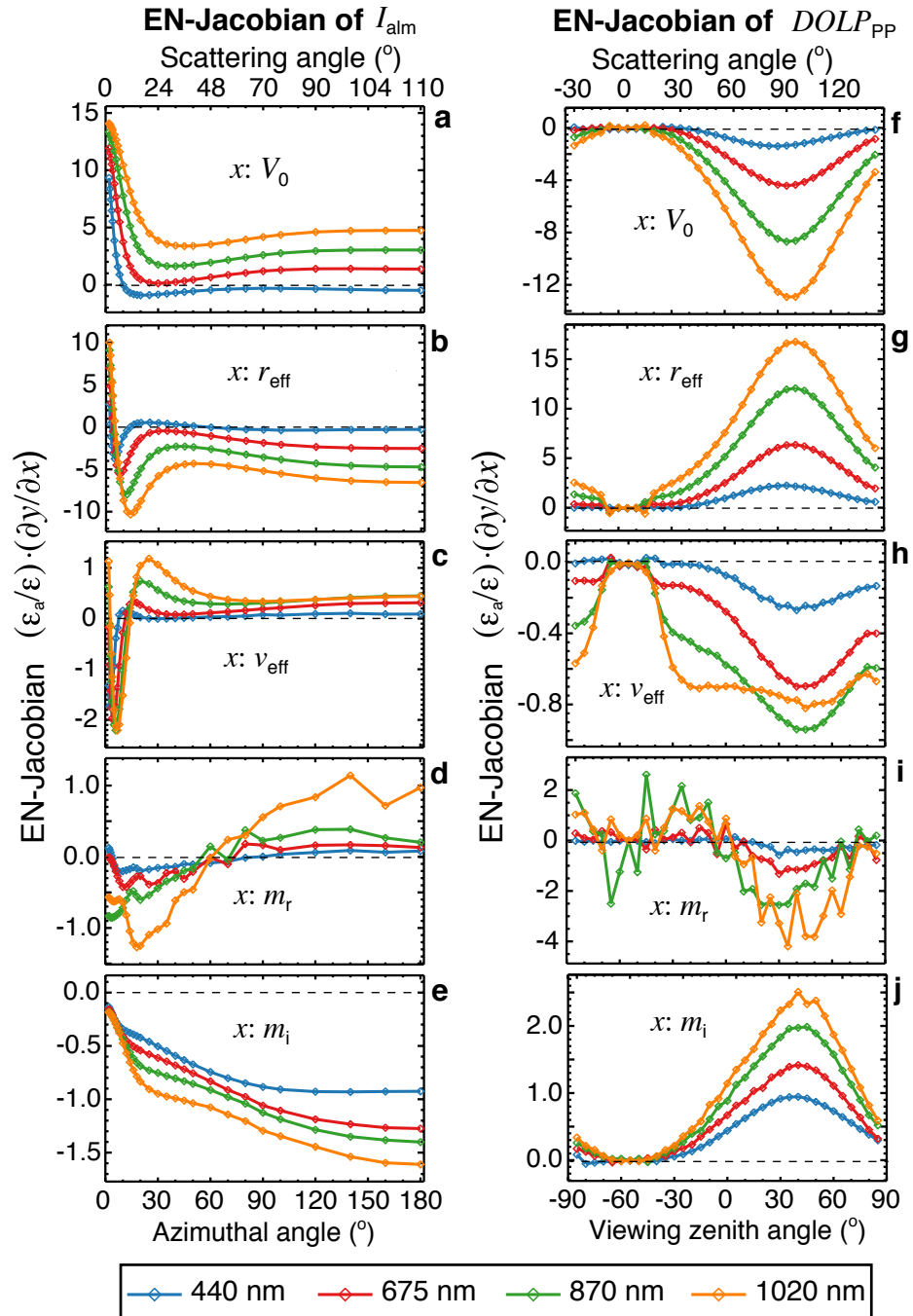
Figure 4.4: Same as Figure 4.3 but for parameters of aerosol in the *coarse* mode.

the change of size parameter η, which defined as the ratio of the particle size to the applied spectral wavelength, $\eta = 2\pi r_{\text{eff}}/\lambda$. The DOLP$_{\text{pp}}$ in scattering angles near 90° approaches unity under pure Rayleigh scattering regime where $\eta \ll 1$. When the η increases, the value of $\partial \text{DOLP}_{\text{pp}}/\partial V_0$ decreases and transits into negative at $\eta \sim 2$, reaches negative maxima at $\eta \sim 10$, then increases and slowly transits back to positive when η is as large as ~ 40 [*Hansen and Travis*, 1974]. The magnitude of the η at these four bands ranges from 3.0 to 1.3 for the fine-mode particles and from 27 to 11 for the coarse-mode particles. Therefore we can understand that: (i) the sensitivity of DOLP$_{\text{pp}}$ to the fine-mode V_0 is positive at 1020 nm due to the small size parameter $\eta = 1.3$ (orange curve in Figure 4.3f); (ii) this sensitivity gets weaker at 675 nm to 870 nm and transits to negative at 440 nm as η increases (Figure 4.3f); and (iii) this sensitivity for aerosol in the coarse mode is more negative for longer wavelengths that are corresponding to smaller values of η.

We also note that sensitivity of the I_{alm} to PSD parameters dominates for scattering angles less than $\sim 40°$ (Figures 4.3b-c and 4.4b-c), while its sensitivity to m_{r} and m_{i} prevails at larger scattering angles (Figures 4.3d-e and 4.4d-e). In the near-forward scattering angular regions, the dominant scattering effect is the diffraction of light, which essentially depends on the size of particles and is independent of the index of refraction [*van de Hulst*, 1981; *Hansen and Travis*, 1974]. The DOLP$_{\text{pp}}$, in contrast, is sensitive to both the aerosol size and the refractive index at scattering angles from 45° to 135° (right columns of the Figures 4.3 and 4.4). Variations of the sensitivity among spectral bands can be explained by the wavelength-dependent size parameters as discussed in the above paragraph.

Overall, the DOLP$_{\text{pp}}$ EN Jacobians have similar or larger magnitudes to these of I_{alm}, indicating that the DOLP$_{\text{pp}}$ measurements possess equal or larger information for the inversion of these aerosol properties. Adding such complementary DOLP$_{\text{pp}}$ measurements to the current radiance-only inversion can potentially increase the retrieval accuracy. The magnitude of EN Jacobian elements varies among retrieved parameters, which leads to the

variability of retrieval accuracy. The EN Jacobians with respect to the V_0 and r_{eff} of both modes and the fine-mode v_{eff} and refractive index are larger than those of other parameters. Correspondingly, these parameters are expected to achieve higher accuracy in the retrieval. While the maxima in EN Jacobians of I_{alm} with respect to the coarse-mode refractive index at 870 and 1020 nm slightly excess unity (Figure 4.4d-e), larger counterparts for DOLP_{pp} (Figure 4.4i-j) will likely result in improved retrievals. In contrast, magnitudes of EN Jacobian for both I_{alm} and DOLP_{pp} with respect to coarse-mode refractive index at 440 and 675 nm are smaller than unity across the whole angular range. Adding polarization may not improve the retrieval for coarse-mode refractive index at those shorter wavelengths in such aerosol scenario. However, the consideration of spectral dependence of refractive index by using the smoothness constraints will potentially resolve this problem [*Dubovik*, 2004].

4.3.2   Information content and retrieval error

We calculated the averaging kernel matrix **A**, DFS, and *a posteriori* error for retrieved parameters from these four scenarios of observation defined in Table 4.3. Figuress 4.5a-c illustrate how the DFS varies with the solar zenith angles for three defined aerosol types. The DFS in the scenario I2 (red curves) ranges from 14 to 15 for the fine-dominated aerosol model, and from 17 to 19 for other two aerosol models, about 2–3 degrees higher than those using AODs and I_{alm} measurements in the scenario I1 (black curves), indicating that sky radiances in the principal plane (I_{pp}) contain additional information. The scenario P1 (green curves), which comprises solar almucantar sky radiances and principal-plane polarimetric radiances at four wavelengths, further increases DFS by 1–2. Observations in the scenario P2 (blue curves)—radiance and polarization in the almucantar plane—yields DFS values slightly below those in the scenarios I2 and P1. Therefore, from Figure 4.5 we conclude that adding measurements in the solar principal plane into the inversion significantly increases the
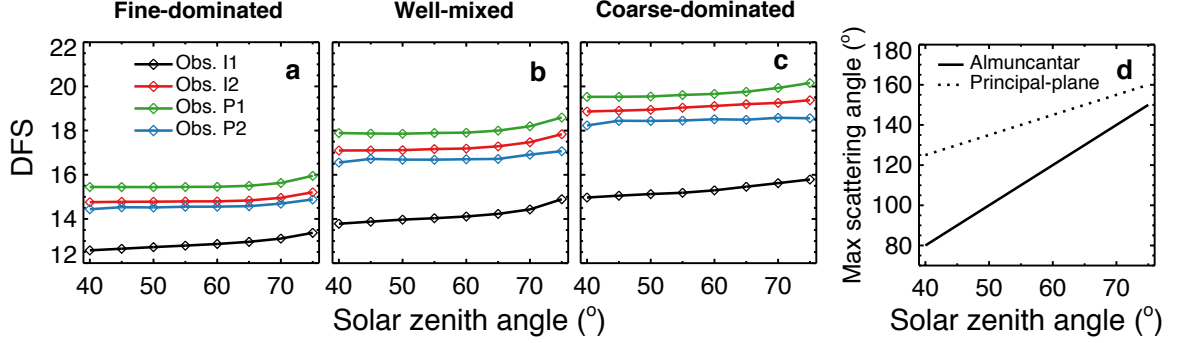
Figure 4.5: Degree of freedom for signal (DFS) as a function of solar zenith angle for retrieving all 22 parameters when using aerosol type of (a) fine-dominated, (b) well-mixed, and (c) coarse-dominated. Four differently colored-curves denote four observation scenarios defined in Table 1. Panel (d) shows the maximum scattering angles that can be reached by the almucantar and the principal-plane scans.

information content for aerosol properties, especially when combining the I_{pp} and $DOLP_{pp}$. We also note that the DFS increases with solar zenith angle for all cases. Observations in larger solar zenith angle enable a wider range of scattering angles (Figure 4.5d), and thus contain more information on the aerosol scattering phase function and in turn on the aerosol microphysical parameters.

We illustrate the DFS components $\mathbf{A}_{i,i}$ in Figure 4.6 for the V_0, r_{eff} and v_{eff}, and in Figure 4.7 and 4.8 for the m_r and m_i, respectively. Also shown in those figures are the a posteriori errors, which are the diagonal elements of $\hat{\mathbf{S}}^{\frac{1}{2}}$. It should be noted that errors for V_0, r_{eff}, and v_{eff} are in terms of relative uncertainties (%), while errors in the m_r and m_i are absolute quantities. Curves of four different colors in each panel indicate these defined four observation scenarios and are averages for the three aerosol types. Error bars represent one fifth of the standard deviations among the three aerosol types (the use of the o ne-fifth scale is only for plotting purpose). These error bars thus depict the variability of the DFS component and retrieval error over the fine-mode fraction (fmf_v). Mean retrieval uncertainties averaged over various solar zenith angles are summarized in Table 4.4. We discuss these results for each retrieved parameter in detail as following.

4.3.2.1 Aerosol PSD

Among the 22 elements in the state vector, the V_0, r_{eff} and v_{eff} describe the aerosol PSD. According to Figure 4.6a-c, observations in the scenario P1 (green curves) always yield the highest DFS components for inferring PSD parameters in both the fine and coarse modes, followed by observations from the scenarios I2 (red) and P2 (blue), and lastly the scenario I1 (black). As a consequence, the *a posterior* errors are found smallest for the scenario P1 and largest for the scenario I1 (Figure 4.6d-e). Retrieval errors in the scenario I1 (black curves) are 5–15% for V_0, 5–9% for r_{eff}, and 20–30% for v_{eff}, which vary with solar zenith angles. In contrast, retrieval errors in the scenario P1 (green curves) are reduced to ~2.5%(3%), 1%(3.5%), and 7%(20%) for the fine (coarse) mode. From observations in the scenarios P2 and I2, one can retrieve V_0, r_{eff}, and v_{eff} of errors lying between the scenarios I1 and P1, though slightly larger in the scenario P2. In addition, higher DFS components and smaller retrieval errors are found for the fine-mode parameters than those for the coarse mode, because radiances and polarization are in particular more sensitive to aerosol parameters in the fine mode as shown in the contrast between the Figures 4.3 and 4.4

We also note that, in the scenario I1, DFS components for the coarse-mode parameters decrease with increasing solar zenith angle, while no obvious trend can be found for the fine-mode parameters. This can be explained by the low sensitivity of the I_{alm} to the coarse-mode V_0, r_{eff}, and v_{eff} at large scattering angles as showed in Figure 4.4a-c. Higher sensitivities occur at scattering angles below ~30°; the increase in SZA results in a smaller number of measurements in the near-forward scattering angular regions, and thus leads to larger retrieval errors. However, these trends turn to be weaker or negligible in other observation scenarios, especially the scenario P1. We can understand this from two aspects. First, observations from principal plane can add additional measurements near the forward scattering region. Second and most importantly, the added polarization measurements in
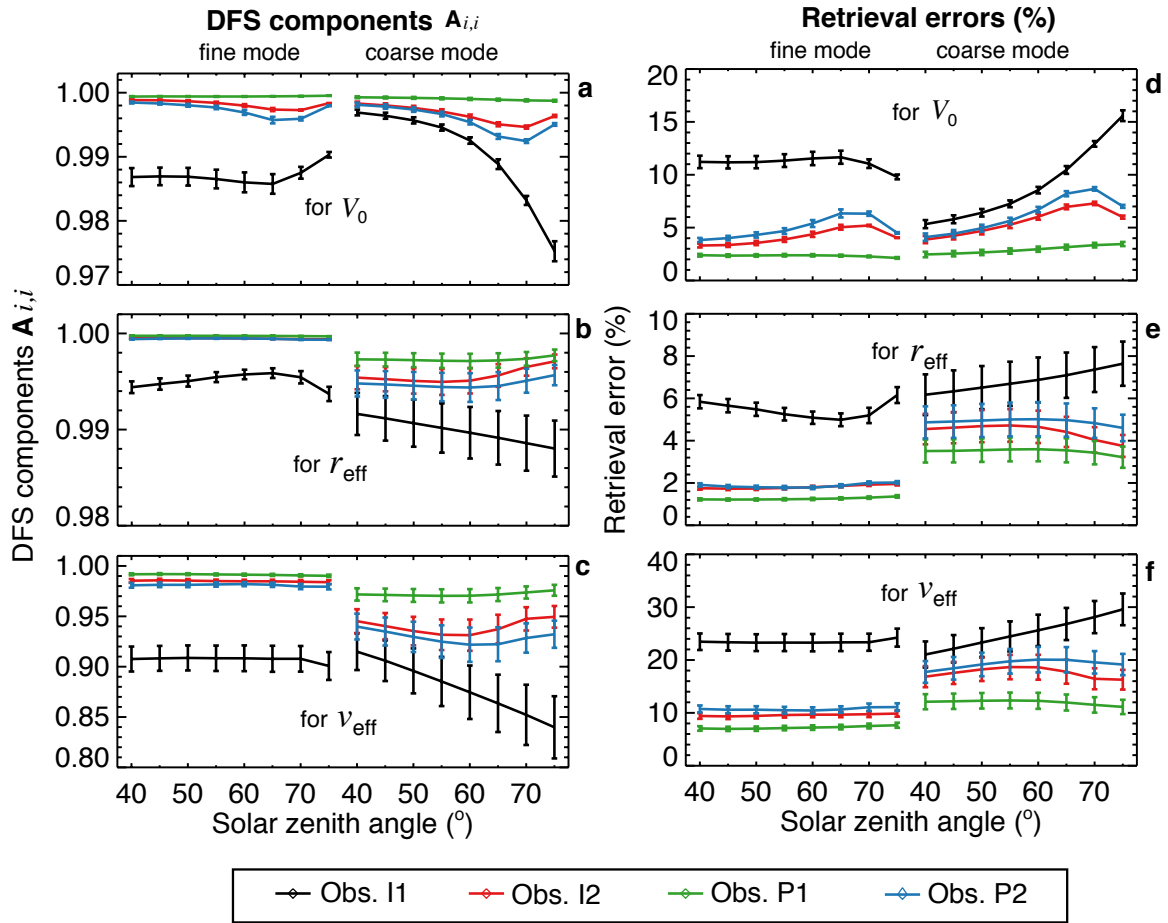
Figure 4.6: DFS components (left column) and retrieval uncertainty (right column) as a function solar zenith angle with different observation scenarios defined in Table 4.3. Quantities are averages for three aerosol types defined in Table 4.2, and error bars represent one fifth of standard deviation. Three rows from top to bottom are respectively for retrieving V_0, r_{eff}, and v_{eff}. In each panel, shown in the left is for the fine mode and in the right is for the coarse mode.

the scenarios P1 and P2 contain additional information that is independent of the scattering

angle limitation as discussed in the section 4.3.1.

Overall, the increase in DFS components by adding polarization measurements is

less than 0.1 for retrieving V_0, r_{eff}, and v_{eff}, because radiances alone contain abundant

information. The retrieval accuracy in aerosol PSD from observations of all scenarios

exceeds the requirements for better quantifying aerosol climate radiative forcing identified

by *Mishchenko et al.* [2004]. Even so, the addition of multi-band DOLP$_{pp}$ measurements to the inversion can still yield up to ∼70% retrieval error reduction in the fine-mode and up to ∼50% reduction in the coarse-mode aerosol PSD parameters.

4.3.2.2 Refractive indices

As shown in Figure 4.7a-b, different magnitudes prevail in the DFS components for the m_r between fine and coarse modes and among different observation scenarios. For example, DFS components for aerosols in the fine mode overreach 0.8 at all four wavelengths in the scenario I1; while the counterparts in the coarse mode approach 0.5 at 1020 nm and are less than 0.2 for the other three wavelengths. This is due to the weaker sensitivity of almucantar radiances to the coarse-mode m_r (as in Figure 4.4d) comparing to that for aerosol in the fine mode (as in Figure 4.3d). In general, adding the DOLP$_{alm}$, I_{pp}, or both the I_{pp} and DOLP$_{pp}$ in the inversion increases the DFS components for m_r of aerosols in both the fine and the coarse modes. Particularly, DFS components achieve the most significant rise in the scenario P1 by climbing to 0.95–1.0 in the fine mode and to 0.4–0.8 in the coarse mode. Also shown in Figure 4.7a, an increasing pattern with solar zenith angles is found in the DFS components for the fine-mode aerosol at larger wavelengths because stronger sensitivity occurs in larger scattering angles.

As expected, the retrieval of m_r can be more accurate by adding additional measurements. According to Figure 4.7c-d, the *a posteriori* error in m_r averaged on the four spectral bands is ∼0.015 (0.065) for aerosols in the fine (coarse) mode from measurements in the scenario I1. In contrast, it is reduced to 0.008 (0.037), 0.005 (0.035), and 0.009 (0.040) in the scenarios I2, P1, and P2, respectively. Retrieval errors in the coarse-mode m_r are larger in shorter spectral wavelengths because of weaker sensitivity to the I_{alm} and DOLP. For instance of the scenario P1, it is about 0.06 at 440 nm, 0.035 at 675 nm, and 0.02 at 870 and 1020 nm.

The DFS components for the m_i are shown in Figure 4.8a–b, and the corresponding
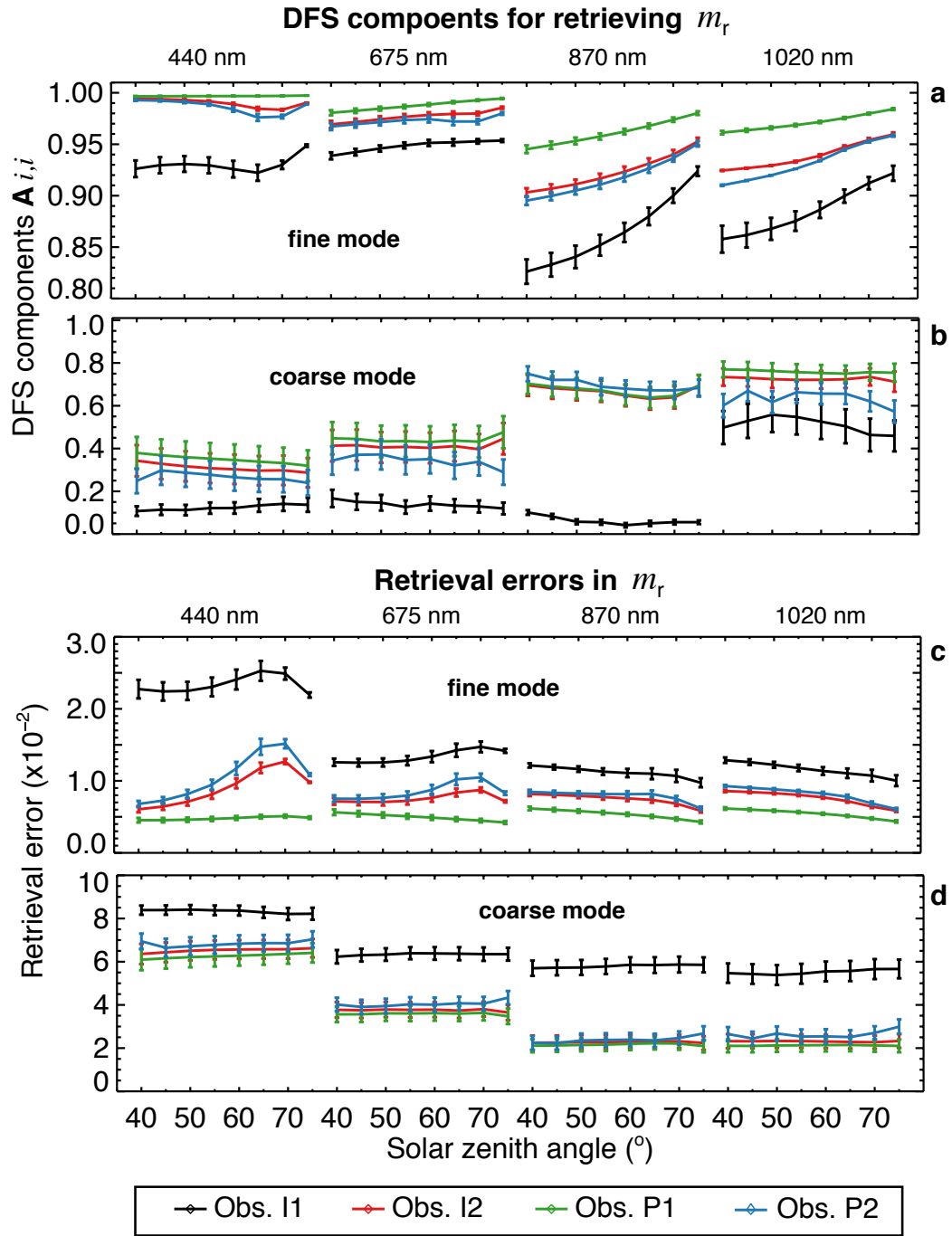
Figure 4.7: Same as Figure 4.6 but for DFS components (a-b) and retrieval uncertainty (c-d) for retrieving real part refractive index *mreal* in four wavelength bands. (a) and (c) are for the fine aerosol mode, while (b) and (d) for the coarse mode.
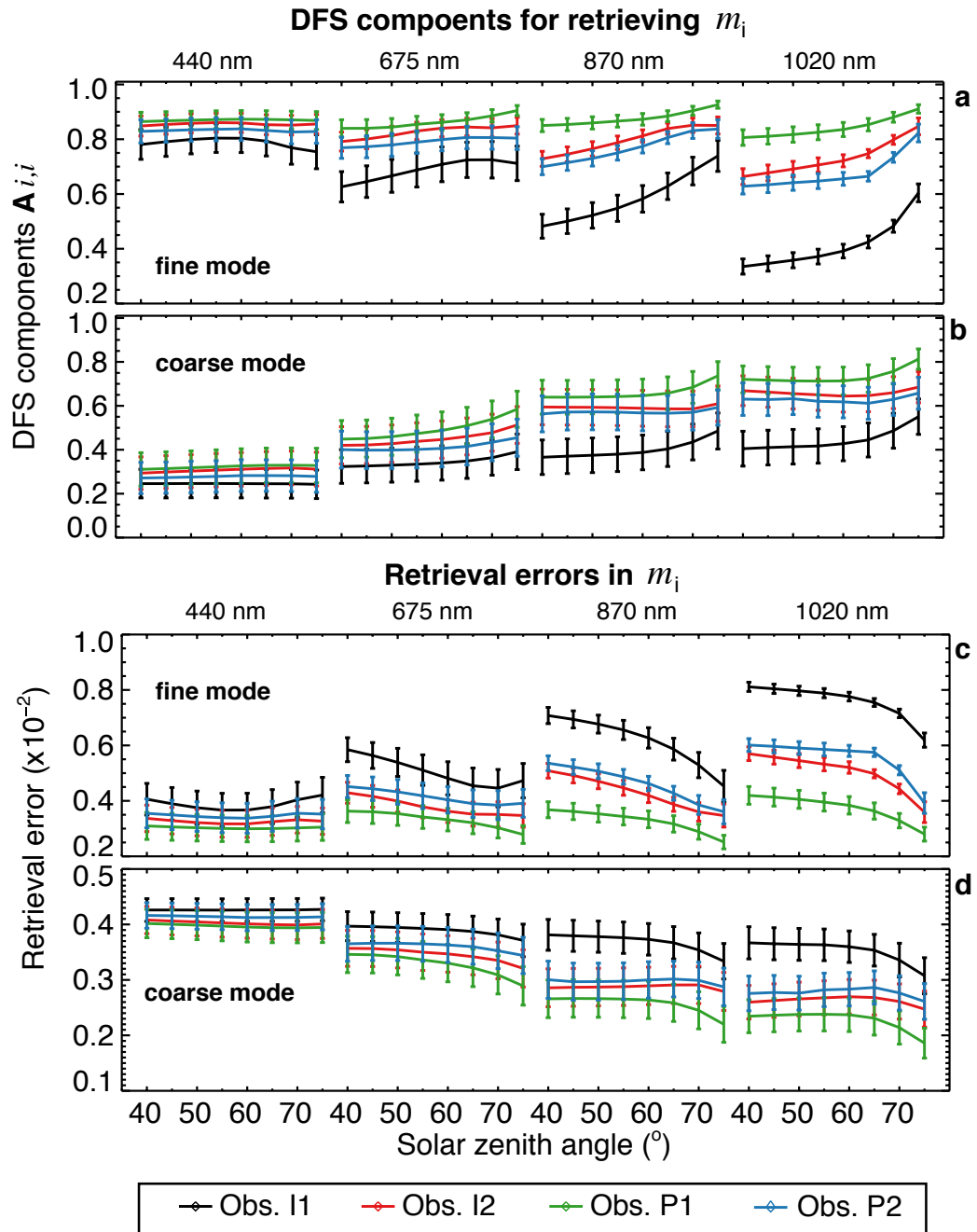
Figure 4.8: Same as Figure 4.7 but for retrieving imaginary part refractive index m_i.

Table 4.4: Error for retrieved and derived parameters among *a priori*, *a posteriori*, and Glory characterization[a].

| Entries | Error in retrieved parameters | | | | | |
	V_0 (%)	r_{eff} (%)	v_{eff} (%)	m_{r}	m_{i}	ω_{A}
A priori	100/100	80/80	80/80	.15/.15	.01/.05	-
Obs. I1	11./9.0	5.5/6.8	23/25	.015/.065	.0057/.0038	.037/.085
Obs. I2	4.1/5.5	1.8/4.4	10/18	.008/.037	.0041/.0032	.024/.073
Obs. P1	2.3/2.9	1.3/3.5	7.2/12	.005/.035	.0033/.0030	.019/.068
Obs. P2	4.9/6.2	1.9/4.9	11/19	.009/.040	.0044/.0034	.026/.076
Glory[b]	–	10	40	.02	–	.03

[a]Results of our work are averaged values for three aerosol types and for solar zenith angles from $40°$ to $70°$.
[b]Referred to *Mishchenko et al.* [2004].

retrieval errors in m_{i} are displayed in Figure 4.8c–d. Similar to those for the m_{i}, DFS components for retrieving the m_{i} are larger in the fine mode and show an increasing pattern with the solar zenith angle. Observations in the scenario P1 always yield largest DFS components and smallest retrieval error for the m_{i}, followed by the scenarios P2 and I2. Observations in the scenario I1 offer the m_{i} retrieval with largest error. If averaged on the solar zenith angles and aerosol types, the retrieval error in the m_{i} is 0.006 (0.004) for aerosol in the fine (coarse) mode in the scenario I1, and can be reduced to 0.003 (0.003) in the scenario P1.

4.3.2.3 Single scattering albedo

Note that the aerosol single scattering albedo ω_{A} is an intermediate rather than a directly retrieved parameter. The error in ω_{A} can be estimated from the $\hat{\mathbf{S}}$ with the equation (3.9). The ω_{A} for each aerosol mode uniquely depends on the light wavelength and aerosol microphysical parameters including r_{eff}, v_{eff}, and m_{r} and m_{i}, although the m_{i} impacts ω_{A} most significantly [*Hansen and Travis*, 1974]. Required derivatives of ω_{A} to these parameters in the equation (3.9) can be obtained from the linearized Mie code (section 2.2.2) integrated

into the UNL-VRTM. We calculated uncertainties in the ω_A for each wavelength and each aerosol type, and the averaged values are summarized in Table 4.4. Observations in these four scenarios can retrieve ω_A with the uncertainty of 0.037, 0.024, 0.019, and 0.026 for the fine mode, and 0.085, 0.073, 0.068, and 0.076 for the coarse mode, respectively. Thus, only the fine-mode ω_A retrieval with polarization involved can meet the accuracy requirements (0.03) for accurate climate forcing estimates [*Mishchenko et al.*, 2004]. We noted that the mean uncertainty in the coarse-mode ω_A exceeds 0.06 in all of these four scenarios, but higher accuracy may be achieved under coarse-dominated conditions as shown in the following section.

4.4 Sensitivity of retrieval error to AOD and fmf

The performance of retrieval usually varies with aerosol conditions like the aerosol loading and the prevalence of aerosol in either the fine or the coarse modes (e.g., fine-mode volume fraction, fmf_v). As a result, uncertainties in aerosol retrievals can depend much more strongly on the AOD than they do on the properties of an individual aerosol model [*Knobelspiesse et al.*, 2012]. For the same reason, the inversion of refractive indices and ω_A in the current AERONET algorithm is confined to the condition when the 440-nm AOD is larger than 0.4 [*Dubovik et al.*, 2000; *Holben et al.*, 2006]. Our above analysis, which focused on three aerosol types by a constant AOD value at 440 nm (τ_{A440}=1.0), is insufficient to represent variable global conditions. At the same time, we also found noticeable variability of the DFS components and a posteriori errors existing among three aerosol types with different fmf_v, especially for the coarse-mode parameters. Thus, it is necessary to investigate how aerosol conditions affect the retrieval error, in order to answer the question: under what aerosol conditions the AERONET measurements (with and without polarization) are capable to yield retrievals with satisfied accuracy?
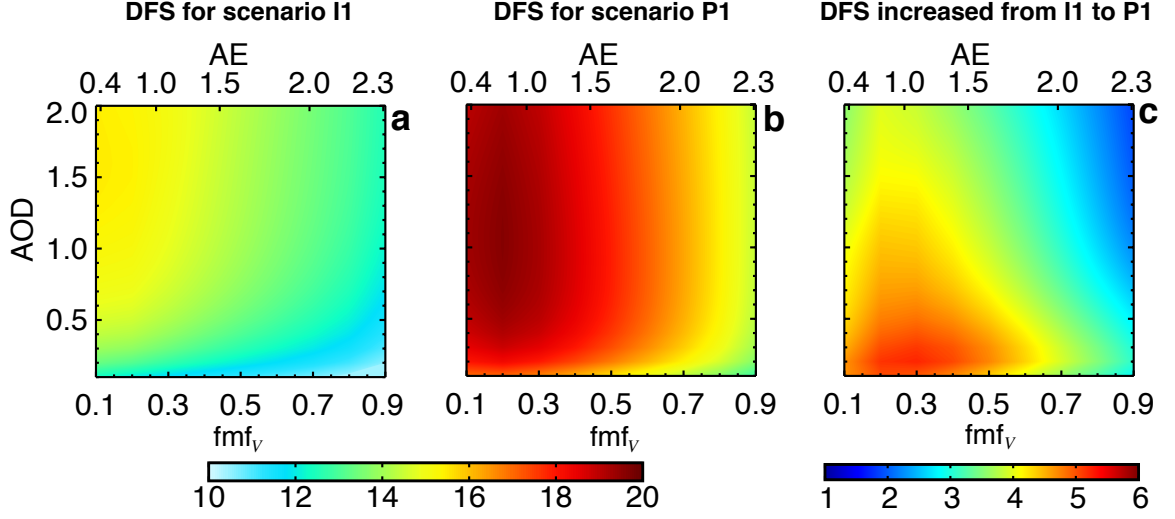
Figure 4.9: Contours of DFS as a function of fmf$_v$ and AOD in scenarios I1 (a) and P1 (b). (c) the difference of DFS between (a) and (b). Simulations are for solar zenith angle of 55°. The top abscissa denotes Ångström exponent (AE).

We expand our analysis for the τ_{A440} ranging from 0.1 to 2.0 and for the fmf$_v$ from 0.1 to 0.9. In practice, the fmf$_v$ is inaccessible prior to inversion. Instead, we use the Ångström exponent (AE) from 870 to 1020 nm together with τ_{A440} to define the aerosol conditions, because the AE in the longer paired wavelength is highly related to the fmf$_v$ [*Schuster et al.*, 2006] and immediately available from the AERONET direct sun measurements. With the aerosol properties defined in the Table 4.3, the fmf$_v$ from 0.1 to 0.9 gives AE values from 0.35 to 2.3. We exclude the scenarios of I2 and P2 in our following analysis, because the scenario P1 demonstrates the most superior performance and is also the focus of our algorithm development.

Figure 4.9a–b display the contours of DFS as a function of the AE (or fmf$_v$) and τ_{A440} in the scenarios I1 and P1, respectively. We found that the DFS decreases with an increasing AE and fmf$_v$ for the same AOD. This is attributed to the fact that the coarse-mode parameters are more difficult to retrieve than their fine-mode counterparts, restrained by their weaker sensitivities to the I_{alm} and the DOLP$_{pp}$. Thus, the decrease in the coarse-mode fraction
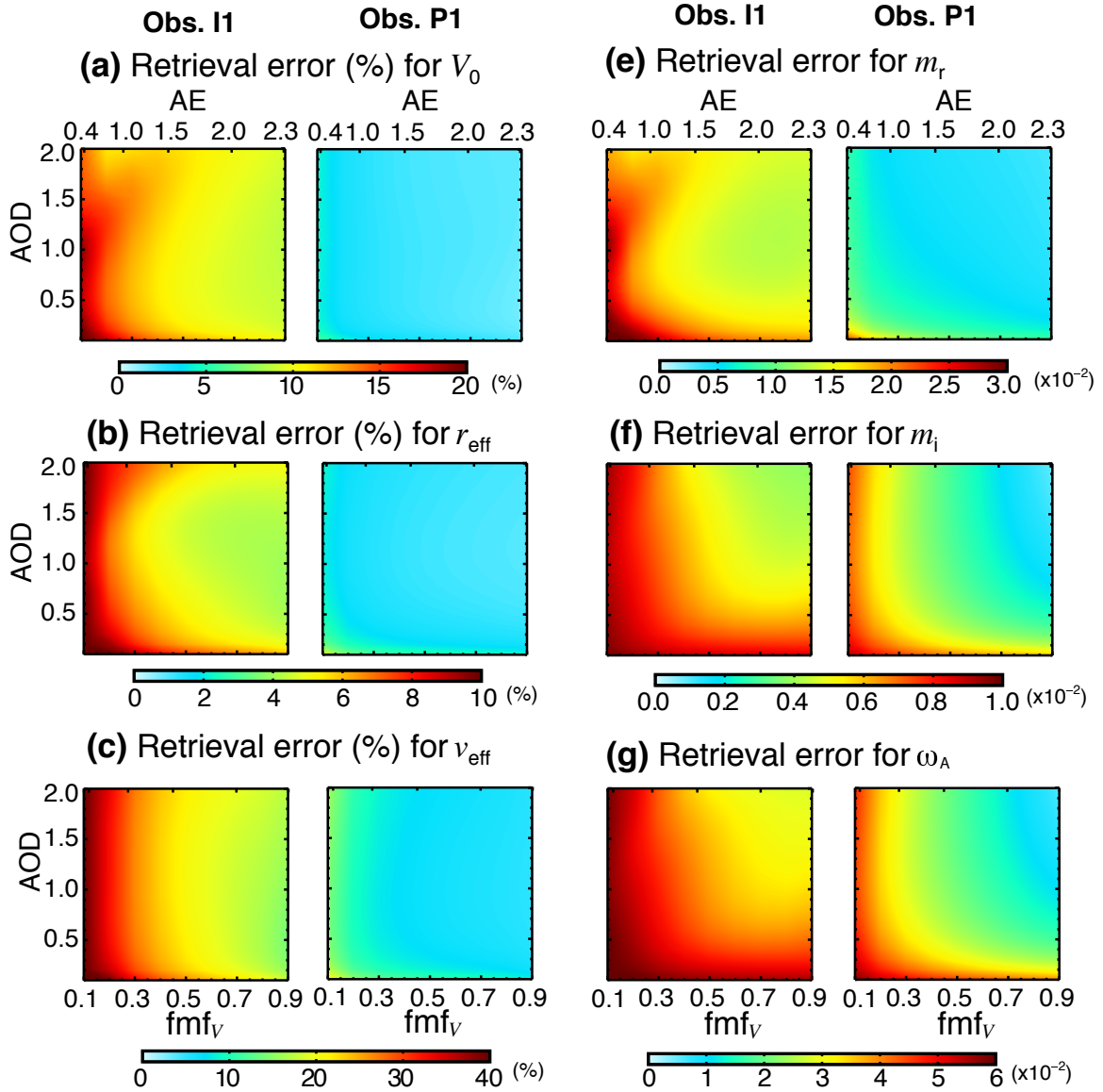
Figure 4.10: Retrieval uncertainties as a function of fmf_v (or AE) and AOD for each individual aerosol parameters in the *fine* mode: (a) V_0, (b) r_{eff}, (c) v_{eff}, (d) m_r, (e) m_i, and (f) ω_A. Two sub-panels in each panel indicate observations in the scenarios I1 and P1, respectively. Simulations are for solar zenith angle of $55°$. The x- and y-axis are identical to those in Figure 4.9. Relative uncertainties are shown for V_0, r_{eff} and v_{eff}, while absolute errors for m_r, m_i, and ω_A. Retrieval errors for m_r, m_i, and ω_A are averaged values over the four spectral bands.
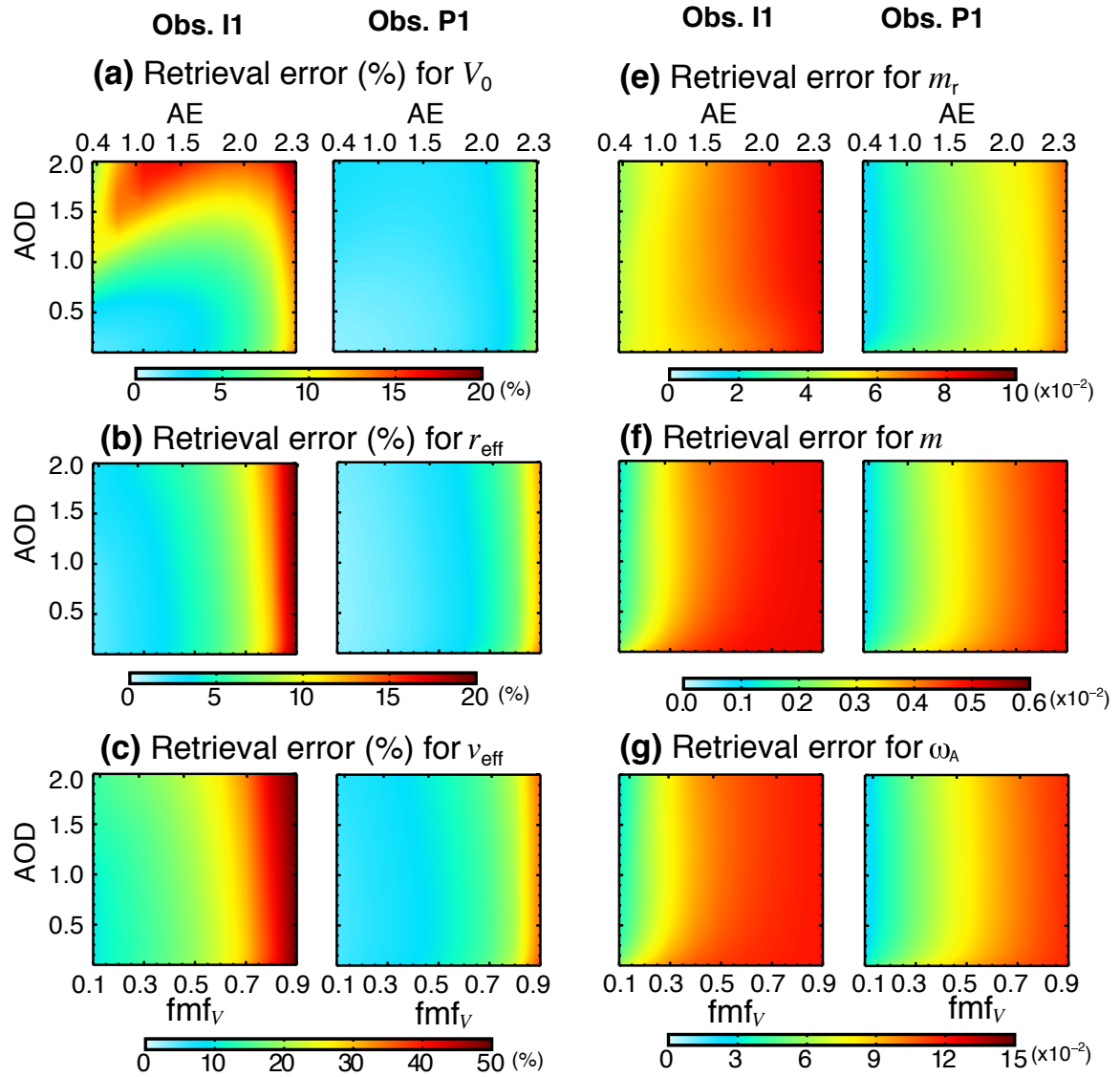
Figure 4.11: Same as Figure 4.10, but for aerosol parameters in the *coarse* mode.

significantly reduces the aerosol information for coarse-mode parameters but retain the information for fine-mode parameters, resulting in decreases in the total DFS. We also notice from Figure 4.9a that the DFS increases with an increasing AOD in the scenario I1. However, AOD change has less impact in the scenario P1 (Figure 4.9b). For example, the DFS values are lower than 14 when AOD $<$ 0.4 in the scenario I1, whereas even larger DFS can be found in the scenario P1 when AOD $<$ 0.2. Therefore, we may expect that the inversion in the scenario P1 will be capable to retrieve aerosol parameters in conditions of lower aerosol loading, and may bring down the τ_{A440} threshold of 0.4 from the current AERONET inversion algorithm to retrieve the refractive index and ω_A. Finally, as indicated in Figure 4.9c, the addition of I_{pp} and $DOLP_{pp}$ in the inversion can add 2–5 pieces of useful information. Such improvement occurs in all aerosol conditions but is more dominated when enough coarse particles are present: $fmf_v < 0.5$ (or AE< 1.6), in which the radiance-only inversion usually yields a large retrieval error for the fine-mode aerosol.

In Figures 4.10 and 4.11, we show the contours of the a posteriori error $\hat{\varepsilon}$ in the scenarios I1 and P1 for the individual fine-mode and coarse-mode parameters, respectively. Overall, observations in scenarios P1 offer more accurate retrievals for all parameters in both the fine and the coarse aerosol modes. In both scenarios, the $\hat{\varepsilon}$ decreases for fine-mode parameters and increases for coarse-mode parameters with increasing the AE (or fmf_v) for same τ_{A440}, indicating that the relative contribution of fine and coarse modes determines the relative information of each mode. Extreme cases are fmf_v of 1 or 0, i.e., the absence of the coarse- or fine-mode aerosols, which certainly will only allow a mono-modal retrieval. Thus, the bi-modal retrieval, especially for refractive indices, requires that aerosols reach certain mixture conditions to contain enough information for both modes. For example in the scenario I1, while the fine-mode r_{eff} can be well retrieved with 5% accuracy when the $fmf_v > 0.2$ at τ_{A440} of 0.5 (Figure 4.10b), the $fmf_v > 0.3$ is required to ensure the $\hat{\varepsilon} < 0.02$ in the fine-mode m_r (Figures 4.10e). Comparing to the change of the fmf_v, the change of

Table 4.5: Required aerosol conditions (τ_{A440} and AE) to achieve anticipated retrieval accuracy $<\varepsilon>$ for observations in scenario I1 and P1.

		Scenario I1		Scenario P1	
x	$<\varepsilon>$	τ_{A440}	AE	τ_{A440}	AE
V_0^f	10%	>0.3	>1.5	[a]All	All
V_0^c	10%	<1.3	<2.2	All	All
r_{eff}^f	5%	>0.3	>1.3	All	All
r_{eff}^c	10%	All	<2.0	All	<2.2
v_{eff}^f	20%	>0.3	>1.5	All	All
v_{eff}^c	30%	All	<1.8	All	<2.2
m_r^f	0.02	>0.4	[b]**>1.0**	All	All
m_r^c	0.04	All	**<1.0**	All	<1.8
ω_A^f	0.04	>0.6	**>1.5**	>0.2	>0.7
ω_A^c	0.08	>0.2	**<1.1**	All	<1.6

[a] 'All' indicates conditions: $0.1 < \tau_{A440} < 2.0$ and $0.35 < AE < 2.3$;
[b] 2Underlined bold indicate conditions that cannot allow bi-modal retrievals.

τ_{A440} has less impact on the $\hat{\varepsilon}$ of the PSD parameters; and this impact occurs in low aerosol loadings. For example, Figure 4.10g shows that a minimum of ∼0.4 for τ_{A440} is required in the scenario I1 to guarantee a retrieval error in the fine-mode ω_A less than 0.04 when $fmf_v = 0.5$.

From the Figures 4.10 and 4.11, we can identify required aerosol conditions in terms of the AE and τ_{A440} in order to achieve certain anticipated accuracy $<\varepsilon>$, which are summarized in Table 4.5. Clearly, observations with polarization can enable retrievals of same accuracy in a lower aerosol loading. For example, the retrieval accuracy of 10% for the V_0 and r_{eff} and 30% for the v_{eff} in the fine mode requires τ_{A440} to be larger than 0.3 for inversion in the scenario I1 (Figure 4.10a–c). In contrast, inversion in the scenario P1 can easily ensure retrievals of the same accuracy when τ_{A440} is 0.1. For the fine-mode m_r retrieval, an accuracy of 0.04 requires $\tau_{A440} > 0.4$ for the inversion I1 but $\tau_{A440} > 0.2$ for the inversion P1 (Figure 4.10e). Moreover, the radiance-only inversion is unable to resolve the bi-modal m_r and ω_A under any circumstance, because AE>1.5 is necessary for retrieving the fine-mode ω_A (Figure 4.10g), meanwhile AE<1.1 is required for its coarse-mode retrieval

(Figure 4.11g). This agrees with *Dubovik et al.* [2000] in that the retrieval of refractive indices for both fine and coarse mode is essentially non-unique due to limited information in the AERONET (radiance-only) observations. In contrast, observations in the scenario P1 can allow bi-modal retrievals of the m_i and ω_A when $0.7 < \text{AE} < 1.6$ and $\tau_{A440} > 0.2$ (Figures 4.10g and 4.11g). Therefore, our retrieval algorithm is designed to use observations of scenario P1 to retrieve bi-modal refractive indices when τ_{A440} and AE reach these criteria. In aerosol conditions beyond the criteria, bi-modal PSD along with a mono-modal refractive index will be retrieved by assuming the refractive index is independent of the aerosol mode.

4.5 Summary

In an effort to improve the AERONET inversion by including additional polarization measurements, this study examines the potential microphysical aerosol information contained in the AERONET photo-polarimetric observations. We have focused our analysis on how the added polarization measurements impact on the retrieval accuracy the in aerosol particle size distribution (PSD), spectral refractive index, and single scattering albedo ω_A. A numerical testbed has been constructed to generate the synthetic AERONET radiance and degree of linear polarization (DOLP) over 440, 675, 870, and 1020 nm. We considered four scenarios of observations to whether or not include the DOLP for the inversion, i.e., (I1) direct Sun AOD and almucantar sky radiances, (I2) observations in the scenario I1 with additional radiance measurements in the solar principal plane, (P1) observations in the scenario I2 plus polarization measurements in the solar principal plane, and (P2) observations in the scenario I1 plus almucantar polarization. Measurements in the scenario I1 are those used in current AERONET inversion algorithm, and thus represent a control experiment. For each observation scenario, we also considered three aerosol types to represent general aerosol climatology. The Bayesian statistical approach then was applied to relate information

contained in those synthetic data and retrieval errors in aerosol physical parameters to the instrumental as well as the a priori characteristics. Then the error-normalized Jacobian, degree of freedom for signal (DFS), and the a posteriori error in each individual retrieved parameter were presented as function of solar zenith angle for these observation scenarios.

The results show a remarkable increase in information by adding additional polarization and/or radiances into the inversion. Overall, observations in the scenario P1 yield the highest DFS, which is larger than that in the scenario I1 by 2–5 for all defined aerosol types. This can be understood that polarization measurements in the solar principal plane, in comparing with sky radiances in solar almucantar, have complementary sensitivities with respect to retrieved aerosol parameters. Also, measurements in the principal plane allow a wider range of scattering angles and supplies more information on aerosol backscattering. In scenario P2, adding polarization in the solar almucantar offer an increase of $\sim$2 pieces of information with DFS values slightly below those in scenarios I2. We also note that the DFS increases with increasing solar zenith angle for all cases, resulting from more information contained in observations of a wider range of scattering angle.

We also analyzed the DFS components and the a posteriori uncertainty for each individual retrieved parameter. As expected, the smallest retrieval errors were always found in the scenario P1: 2.3% (2.9%) for the volume concentration, 1.3% (3.5%) and 7.2% (12%) for the effective radius and effective variance, 0.005 (0.035) for the real part of refractive index, and 0.019 (0.068) for the single scattering albedo in the fine (coarse) mode. These values represent an error reduction from the scenario I1 of 79% (57%), 76% (49%), 69% (52%), 66% (46%), and 49% (20%), respectively. Uncertainties in retrieved parameters averaged among these three aerosol types are summarized in the Table 4.4 for each observation scenario.

Seeking to answer under what conditions the inversions can achieve a mode-resolved aerosol refractive index and ω_A, we further investigated how the AOD (τ_{A440}) and fine/coarse

modal domination (in terms of Ångström exponent, or AE) influence the retrieving accuracy from observations in the scenarios I1 and P1. We found that adding principal-plane polarization measurements can increase the DFS by up to $\sim$5 in cases dominated by coarse-mode particles ($\text{fmf}_v < 0.5$), in which the radiance-only inversion usually yields larger retrieval uncertainty for fine-mode aerosol. As a consequence, these photo-polarimetric observations can enable accurate retrievals in a lower aerosol loading when the τ_{A440} is 0.1, except for the fine-mode m_r retrieval that requires $\tau_{A440} > 0.2$. The analysis also indicate that the radiance-only inversion is unable to resolve bi-modal m_i and ω_A under any circumstance. However, observations in the scenario P1 can allow bi-modal retrievals of m_i and ω_A when $0.7 < \text{AE} < 1.6$. Such criteria can guide us in the practical retrieval algorithm to determine whether a mono-modal or bi-modal retrieval of the aerosol refractive index and ω_A. In aerosol conditions beyond the criteria, bi-modal PSD along with the mode-independent refractive index will be retrieved.

Finally, it should be noted that in our analysis the aerosol particles in each mode are assumed to be poly-disperse homogeneous spheres. Although the linearized T-matrix code has been implemented in our model, the simulation of scattering properties for large non-spherical particles (for example spheroids) still remain computational limitations. Our future efforts will implement non-spherical treatment in order to more realistically represent mineral dust aerosols.

CHAPTER 5

CASE DEMONSTRATIONS

5.1   Selected case and the a priori characterization

5.2   Fitting Residuals

5.3   Retrieved Aerosol Properties

5.4   Improvement over Radiance-Only Retrievals

5.5   Summary

CHAPTER 6

SUMMARY AND OUTLOOK

6.1   Summary of the Dissertation

6.2   Main Conclusions of This Work

6.3   Outlook and Future Work

APPENDIX A

ABBREVIATIONS AND ACRONYMS

APPENDIX B

SYMBOLS

A   Averaging kernel matrix

$\mathbf{B}^j$ Greek matrix, or the coefficients of phase matrix expansion

A   Averaging kernel matrix

A   Averaging kernel matrix

A   Averaging kernel matrix

A   Averaging kernel matrix

A   Averaging kernel matrix

A   Averaging kernel matrix

A   Averaging kernel matrix

A   Averaging kernel matrix

A   Averaging kernel matrix

A   Averaging kernel matrix

A   Averaging kernel matrix

A   Averaging kernel matrix

A   Averaging kernel matrix

A   Averaging kernel matrix

A   Averaging kernel matrix

A   Averaging kernel matrix

A   Averaging kernel matrix

A   Averaging kernel matrix

A   Averaging kernel matrix

A   Averaging kernel matrix

A   Averaging kernel matrix

A   Averaging kernel matrix

A   Averaging kernel matrix

A   Averaging kernel matrix

A   Averaging kernel matrix

A   Averaging kernel matrix

A   Averaging kernel matrix

A   Averaging kernel matrix

APPENDIX C

DERIVATIONS OF TRANSFORMATION VECTOR Π

Let x be an aerosol microphysical parameter. The aerosol extinction and scattering optical thickness (τ_A and δ_A), single scattering albedo (ω_A), and Greek coefficient matrix ($\mathbf{B}_A^j$) are functions of x. However, the gaseous absorption and Rayleigh scattering parameters are independent of x. This appendix outlines the derivations of equations (2.19) and (2.21) and the expressions in Table 2.1 and Table 2.2.

First, we transform equation (2.18) as below:

$$\phi_x = \frac{x}{\tau}\frac{\partial \tau}{\partial x} = \frac{x}{\tau}\frac{\partial(\tau_G + \tau_R + \tau_A)}{\partial x} = \frac{1}{\tau}x\frac{\partial \tau_A}{\partial x} \tag{C.1}$$

$$\begin{aligned}
\varphi_x &= \frac{x}{\omega}\frac{\partial \omega}{\partial x} = \frac{x}{\omega}\frac{[(\delta_A + \tau_G)]}{\partial x} \\
&= \frac{x}{\omega}\frac{1}{\tau^2}\left[\tau\frac{\partial(\delta_A + \tau_R)}{\partial x} - (\delta_A + \tau_R)\frac{\partial \tau}{\partial x}\right] \\
&= \frac{x}{\omega\tau}\frac{\partial \delta_A}{\partial x} - (\delta_A + \tau_R)\frac{x}{\omega\tau^2}\frac{\partial \tau_A}{\partial x} \\
&= \frac{x}{\delta_A + \tau_R}\frac{\partial \delta_A}{\partial x} - \frac{1}{\tau}\frac{\partial \tau_A}{\partial x} \\
&= \frac{x}{\delta_A + \tau_R}\frac{\partial \delta_A}{\partial x} - \phi_x
\end{aligned} \tag{C.2}$$

$$\boldsymbol{\Psi}_x^j = \frac{x}{\mathbf{B}^j}\frac{\partial \mathbf{B}^j}{\partial x} = \frac{x}{\mathbf{B}^j}\frac{\partial[(\tau_R\mathbf{B}_R^j + \delta_A\mathbf{B}_A^j)/(\delta_A + \tau_R)]}{\partial x}$$

$$
= \frac{x}{\mathbf{B}^j} \frac{1}{(\delta_A + \tau_R)^2} \left[(\delta_A + \tau_R) \frac{\partial(\delta_A \mathbf{B}_A^j)}{\partial x} - (\tau_R \mathbf{B}_R^j + \delta_A \mathbf{B}_A^j) \frac{\partial \delta_A}{\partial x} \right]
$$

$$
= \frac{x}{\mathbf{B}^j} \frac{1}{\delta_A + \tau_R} \left[\frac{\partial(\delta_A \mathbf{B}_A^j)}{\partial x} - \mathbf{B}^j \frac{\partial \delta_A}{\partial x} \right]
$$

$$
= \frac{1}{(\delta_A + \tau_R) \mathbf{B}^j} \left[\delta_A x \frac{\mathbf{B}_A^j}{\partial x} + (\mathbf{B}_A^j - \mathbf{B}^j) x \frac{\partial \delta_A}{\partial x} \right] \tag{C.3}
$$

These expressions are linear combinations of ϕ_x', φ_x', and $\mathbf{\Psi}_x'^j$ (as defined by equation (2.20)), where

$$
\left[\phi_x', \varphi_x', \left\langle \mathbf{\Psi}_x'^j \right\rangle_{j=1,J} \right]^T = \left[x \frac{\partial \tau_A}{\partial x}, x \frac{\partial \delta_A}{\partial x}, \left\langle x \frac{\partial \mathbf{B}_A^j}{\partial x} \right\rangle_{j=1,J} \right]^T \tag{C.4}
$$

We then can write above equations (C.1)–(C.3) into vector formulism (as equation (2.19):

$$
\left[\phi_x, \varphi_x, \left\langle \mathbf{\Psi}_x^j \right\rangle_{j=1,J} \right]^T = \mathbf{\Pi} \left[\phi_x', \varphi_x', \left\langle \mathbf{\Psi}_x'^j \right\rangle_{j=1,J} \right]^T \tag{C.5}
$$

where $\mathbf{\Pi}$ is a matrix comprising the relevant coefficients, as noted in equation (2.21). Equations (C.5) and (2.21) then act as a universal formulation for preparing linearized inputs of optical property for VLIDORT. Computation of $\left[\phi_x, \varphi_x, \left\langle \mathbf{\Psi}_x^j \right\rangle_{j=1,J} \right]$ can then be achieved by the calculation of $\left[\phi_x', \varphi_x', \left\langle \mathbf{\Psi}_x'^j \right\rangle_{j=1,J} \right]$ for a given parameter x.

Let us first consider the derivation of $\left[\phi_x', \varphi_x', \left\langle \mathbf{\Psi}_x'^j \right\rangle_{j=1,J} \right]$ for certain aerosol optical properties in a given atmospheric layer, i.e., τ_A, ω_A, and β_A^k, where β_A^k indicates one of the elements in the kth aerosol scattering Greek matrix $\mathbf{B}_A^k$.

For $x = \tau_A$, we have

$$
\phi_x' = \tau_A \frac{\partial \tau_A}{\partial \tau_A} = \tau_A \tag{C.6}
$$

$$\varphi_x' = \tau_A \frac{\partial \delta_A}{\partial \tau_A} = \tau_A \omega_A \tag{C.7}$$

$$\mathbf{\Psi}_x'^j = \tau_A \frac{\partial \mathbf{B}_A^j}{\partial \tau_A} = \mathbf{0} \tag{C.8}$$

For $x = \omega_A$, we have

$$\phi_x' = \omega_A \frac{\partial \tau_A}{\partial \omega_A} = 0 \tag{C.9}$$

$$\varphi_x' = \omega_A \frac{\partial \delta_A}{\partial \omega_A} = \omega_A \tau_A \tag{C.10}$$

$$\mathbf{\Psi}_x'^j = \omega_A \frac{\partial \mathbf{B}_A^j}{\partial \omega_A} = \mathbf{0} \tag{C.11}$$

For $x = \beta_A^k$, we have

$$\phi_x' = \beta_A^k \frac{\partial \tau_A}{\partial \beta_A^k} = 0 \tag{C.12}$$

$$\varphi_x' = \beta_A^k \frac{\partial \delta_A}{\beta_A^k} = 0 \tag{C.13}$$

$$\mathbf{\Psi}_x'^j = \beta_A^k \frac{\partial \mathbf{B}_A^j}{\beta_A^k} = \begin{cases} \frac{\delta_A \beta_A^k}{\beta^k} & \text{if } j = k \\ \\ 0 & \text{if } j \neq k \end{cases} \tag{C.14}$$

Expressions in Table 2.1 are then derived by substituting equations (C.6)–(C.14) into equation (C.5).

The UNL-VRTM integrates the VLIDORT with linearized Mie/T-matrix codes, and this combination allows us to generate Stokes vectors and associated analytical Jacobians with respect to aerosol microphysical parameters for two aerosol modes. Thus, we must supply the $\left[\phi_x', \varphi_x', \left\langle \mathbf{\Psi}_x'^j \right\rangle_{j=1,J} \right]$ quantities for all such parameters. We give an example here, assuming that the aerosols are bimodal, with two lognormal size distributions described by geometric standard deviations (σ_g^f and σ_g^c), geometric median radii (r_g^f and r_g^c), and non-sphericity

parameters (ε^{f} and ε^{c}) for the fine and coarse modes. We note that ε is available only when non-spherical particles are assumed (T-matrix code is applied). Complex refractive indices are $m_{\text{r}}^{\text{f}} - m_{\text{i}}^{\text{f}}i$ and $m_{\text{r}}^{\text{c}} - m_{\text{i}}^{\text{c}}i$. Given these microphysical properties, the linearized Mie/T-matrix codes will compute for each mode the scattering and extinction efficiencies (Q_{sca} and Q_{ext}), the set of expansion coefficients ($\mathbf{B}_{\text{A}}^{j}$) of scattering phase matrix, as well as the derivatives of these quantities with respect to these microphysical properties. For a wide size range of aerosol particles, which enable am about 100% accumulated value for the bi-lognormal probability function, the optical thickness for aerosol extinction and scattering and the associated Greek matrix coefficients within for one atmospheric layer can be calculated through

$$\tau_{\text{A}} = \tau_{\text{A}}^{\text{f}} + \tau_{\text{A}}^{\text{c}} = \frac{3V_0^{\text{f}}Q_{\text{ext}}^{\text{f}}}{4r_{\text{eff}}^{\text{f}}} + \frac{3V_0^{\text{c}}Q_{\text{ext}}^{\text{c}}}{4r_{\text{eff}}^{\text{c}}} \tag{C.15}$$

$$\delta_{\text{A}} = \delta_{\text{A}}^{\text{f}} + \delta_{\text{A}}^{\text{c}} = \frac{3V_0^{\text{f}}Q_{\text{sca}}^{\text{f}}}{4r_{\text{eff}}^{\text{f}}} + \frac{3V_0^{\text{c}}Q_{\text{sca}}^{\text{c}}}{4r_{\text{eff}}^{\text{c}}} \tag{C.16}$$

$$\mathbf{B}_{\text{A}}^{j} = \frac{\delta_{\text{A}}^{\text{f}}\mathbf{B}_{\text{A}}^{\text{f}j} + \delta_{\text{A}}^{\text{c}}\mathbf{B}_{\text{A}}^{\text{c}j}}{\delta_{\text{A}}^{\text{f}} + \delta_{\text{A}}^{\text{c}}} \tag{C.17}$$

We can compute vector $\left[\phi_x', \varphi_x', \left\langle \mathbf{\Psi}_x'^{j} \right\rangle_{j=1,J} \right]$ for a given parameter by differentiating above equations (C.15)–(C.17). For $x = V_0^{\text{f}}$ as an example:

$$\phi_x' = V_0^{\text{f}}\frac{\partial \tau_{\mathbf{A}}}{\partial V_0^{\text{f}}} = V_0^{\text{f}}\frac{3Q_{\text{ext}}^{\text{f}}}{4r_{\text{eff}}^{\text{f}}} = \tau_{\text{A}}^{\text{f}} \tag{C.18}$$

$$\varphi_x' = V_0^{\text{f}}\frac{\partial \delta_{\mathbf{A}}}{\partial V_0^{\text{f}}} = V_0^{\text{f}}\frac{3Q_{\text{sca}}^{\text{f}}}{4r_{\text{eff}}^{\text{f}}} = \delta_{\text{A}}^{\text{f}} \tag{C.19}$$

$$\mathbf{\Psi}_x'^{j} = V_0^{\text{f}}\frac{\partial \mathbf{B}_{\mathbf{A}}^{j}}{\partial V_0^{\text{f}}} = \frac{\delta_{\text{A}}^{\text{f}}}{\delta_{\text{A}}}(\mathbf{B}_{\text{A}}^{\text{f}j} - \mathbf{B}_{\text{A}}^{j}) \tag{C.20}$$

And similarly for $x = r_g^f$, we have

$$\phi_x' = \tau_A^f \left(\frac{r_g^f}{Q_{ext}^f} \frac{\partial Q_{ext}^f}{\partial r_g^f} - \frac{r_g^f}{r_{eff}^f} \frac{\partial r_{eff}^f}{\partial r_g^f} \right) \tag{C.21}$$

$$\varphi_x' = \delta_A^f \left(\frac{r_g^f}{Q_{sca}^f} \frac{\partial Q_{sca}^f}{\partial r_g^f} - \frac{r_g^f}{r_{eff}^f} \frac{\partial r_{eff}^f}{\partial r_g^f} \right) \tag{C.22}$$

$$\mathbf{\Psi}_x'^j = \frac{\varphi_x'}{\delta_A} (\mathbf{B}_A^{f,j} - \mathbf{B}_A^j) + r_g^f \frac{\partial \mathbf{B}_A^{s,j}}{\partial r_g^f} \tag{C.23}$$

In a similar fashion, we can obtain the vector $\left[\phi_x', \varphi_x', \left\langle \mathbf{\Psi}_x'^j \right\rangle_{j=1,J} \right]$ for other fine-mode aerosol parameters including τ_A^f, ω_A^f, V_0^f, m_r^f, m_i^f, r_g^f, σ_g^f, and ε^f (as listed in Table 2.2). For coarse-mode aerosol parameters, the derivations are the same with superscript 's' replaced by 'c'.

We have implemented various aerosol-loading vertical profiles into the testbed, including uniform, exponential-decreasing, and quasi-Gaussian profile shapes. For the uniform profile, aerosols are assumed evenly distributed with height. The layer AOD for the exponential-decreasing profile follows form

$$\int_{+\infty}^{z} \tau_A(z) dz = \tau_{a0} \exp \left(-\frac{z}{H} \right) \tag{C.24}$$

where τ_{a0} is the columnar AOD, and H is a scale height parameter. The quasi-Gaussian profile is derived from a generalized distribution function [*Spurr and Christi*, 2014]

$$\tau_A(z) = K \frac{\exp(-\gamma|z - z_{peak}|)}{[1 + \exp(-\gamma|z - z_{peak}|)]^2} \tag{C.25}$$

where K is a constant related to τ_{a0}, γ is related to half-width constant, and z_{peak} is the height having peak loading. Derivatives of layer aerosol optical thickness with respect to these profile parameters (H, γ, and z_{peak} are also included in order to calculate Jacobians of Stokes

vector to these parameters, and the vectors $\left[\phi_x', \varphi_x', \left\langle \mathbf{\Psi}_x'^{j} \right\rangle_{j=1,J}\right]$ for these derivatives are also shown in Table 2.2.

REFERENCES

Bodhaine, B. A., N. B. Wood, E. G. Dutton, and J. R. Slusser (1999), On rayleigh optical depth calculations, *Journal of Atmospheric and Oceanic Technology*, *16*(11), 1854–1861. 2.2.1

Boesche, E., P. Stammes, T. Ruhtz, R. Preusker, and J. Fischer (2006), Effect of aerosol microphysical properties on polarization of skylight: sensitivity study and measurements, *Appl. Opt.*, *45*(34), 8790–8805. 4.1

Boucher, O., et al. (2013), *Clouds and Aerosols. In Climate Change 2013: The Physical Science Basis. Contribution of Working Group I to the Fifth Assessment Report of the Intergovernmental Panel on Climate Change [Stocker T.F., et al. (eds.)]*, p. 571–658, Cambridge University Press, Cambridge, United Kingdom and New York, NY, USA. 1.1

Byrd, R. H., P. Lu, J. Nocedal, and C. Zhu (1995), A limited memory algorithm for bound constrained optimization, *SIAM Journal on Scientific Computing*, *16*, 1190–1208. 3.3.3

Cairns, B., B. E. Carlson, A. A. Lacis, and E. E. Russell (1997), *An analysis of ground-based polarimetric sky radiance measurements*, p. 383–393, Proc. SPIE. 4.1

Chin, M., et al. (2002), Tropospheric aerosol optical thickness from the gocart model and comparisons with satellite and sun photometer measurements, *Journal of the Atmospheric Sciences*, *59*(3), 461–483. 1.1.3

Chowdhary, J., B. Cairns, M. Mishchenko, and L. Travis (2001), Retrieval of aerosol properties over the ocean using multispectral and multiangle photopolarimetric measurements from the research scanning polarimeter, *Geophysical Research Letters*, *28*(2), 243–246. 1.1.3

Chowdhary, J., B. Cairns, and L. D. Travis (2002), Case studies of aerosol retrievals over the ocean from multiangle, multispectral photopolarimetric remote sensing data, *Journal of the Atmospheric Sciences*, *59*(3), 383–397. 1.1.3

Chowdhary, J., B. Cairns, M. I. Mishchenko, P. V. Hobbs, G. F. Cota, J. Redemann, K. Rutledge, B. N. Holben, and E. Russell (2005), Retrieval of aerosol scattering and absorption properties from photopolarimetric observations over the ocean during the clams experiment, *Journal of the Atmospheric Sciences*, *62*(4), 1093–1117. 1.1.3

Coulson, A. (1988), *Polarization and intensity of light in the atmosphere*, VA A Deepak Pub, Hampton. (document), 2.3, 2.3

Coulson, K., J. Dave, and Z. Sekera (1960), *Tables related to radiation emerging from a planetary atmosphere With Rayleigh scattering*, Univ California Press, Berkeley, CA. (document), 2.3, 2.3

Cox, C., and W. Munk (1954), Measurement of the roughness of the sea surface from photographs of the sun?s glitter, *Journal of the Optical Society of America*, *44*(11), 838–850. 2.2.3

Curcio, J. (1961), Evaluation of atmospheric aerosol particle size distribution from scattering measurements in the visible and infrared, *Journal of the Optical Society of America*, *51*(5), 548–551. 1.1.1

Dave, J. V. (1971), Determination of size distribution of spherical polydispersions using scattered radiation data, *Applied Optics*, *10*(9), 2035–2044. 1.1.1

de Rooij, W. A., and C. C. A. H. v. d. Stap (1984), Expansion of mie scattering matrices in generalized spherical functions, *Astronomy and Astrophysics*, *131*(2), 237–248. 2.2.2

Deuzé, J. L., F. M. Bréon, P. Y. Deschamps, C. Devaux, M. Herman, A. Podaire, and J. L. Roujean (1993), Analysis of the polder (polarization and directionality of earth's reflectances) airborne instrument observations over land surfaces, *Remote Sensing of Environment*, *45*(2), 137–154. 1.1.3

Deuzé, J. L., et al. (2001), Remote sensing of aerosols over land surfaces from polder-adeos-1 polarized measurements, *Journal of Geophysical Research: Atmospheres*, *106*(D5), 4913–4926. 1.1.3

Diner, D. J., et al. (1998), Multi-angle imaging spectroradiometer (misr) instrument description and experiment overview, *Geoscience and Remote Sensing, IEEE Transactions on*, *36*(4), 1072–1087. 1.1.3

Drury, E., et al. (2010), Synthesis of satellite (modis), aircraft (icartt), and surface (improve, epa-aqs, aeronet) aerosol observations over eastern north america to improve modis aerosol retrievals and constrain surface aerosol concentrations and sources, *J. Geophys. Res.*, *115*(D14), D14,204. 1.1.3, 4.2.1

Dubovik, O. (2004), *Optimization of Numerical Inversion in Photopolarimetric Remote Sensing*, *NATO Science Series II: Mathematics, Physics and Chemistry*, vol. 161, book section 3, pp. 65–106, Springer Netherlands. 3.3.3, 4.3.1

Dubovik, O., and M. D. King (2000), A flexible inversion algorithm for retrieval of aerosol optical properties from sun and sky radiance measurements, *J. Geophys. Res.*, *105*(D16), 20,673–20,696. 1.1.1, 1.1.2, 3.3.2, 3.3.2, 3.3.2, 3.3.3

Dubovik, O., A. Smirnov, B. N. Holben, M. D. King, Y. J. Kaufman, T. F. Eck, and I. Slutsker (2000), Accuracy assessments of aerosol optical properties retrieved from aerosol robotic network (aeronet) sun and sky radiance measurements, *Journal of Geophysical Research*, *105*(D8), 9791–9806. 1.1.2, 1.1.3, 4.4, 4.4

Dubovik, O., B. N. Holben, T. Lapyonok, A. Sinyuk, M. I. Mishchenko, P. Yang, and I. Slutsker (2002a), Non-spherical aerosol retrieval method employing light scattering by spheroids, *Geophysical Research Letters*, *29*(10). 1.1.1

Dubovik, O., B. Holben, T. F. Eck, A. Smirnov, Y. J. Kaufman, M. D. King, D. Tanre, and I. Slutsker (2002b), Variability of absorption and optical properties of key aerosol types observed in worldwide locations, *Journal of the Atmospheric Sciences*, *59*(3), 590–608. 1.1.3

Dubovik, O., et al. (2006), Application of spheroid models to account for aerosol particle nonsphericity in remote sensing of desert dust, *Journal of Geophysical Research: Atmospheres*, *111*, D11,208. 1.1.1, 1.1.2, 1.1.3, 4.1

Dubovik, O., M. Herman, A. Holdak, T. Lapyonok, D. Tanre, J. L. Deuze, F. Ducos, A. Sinyuk, and A. Lopatin (2011), Statistically optimized inversion algorithm for enhanced retrieval of aerosol properties from spectral multi-angle polarimetric satellite observations, *Atmos. Meas. Tech.*, *4*(5), 975–1018, aMT. 2.2.3

Emde, C., R. Buras, B. Mayer, and M. Blumthaler (2010), The impact of aerosols on polarized sky radiance: model development, validation, and applications, *Atmos. Chem. Phys.*, *10*(2), 383–396, aCP. 4.1

Evans, K. F., and G. L. Stephens (1991), A new polarized atmospheric radiative transfer model, *Journal of Quantitative Spectroscopy and Radiative Transfer*, *46*(5), 413–423, doi: DOI: 10.1016/0022-4073(91)90043-P. 2.3

Frankenberg, C., O. Hasekamp, C. O'Dell, S. Sanghavi, A. Butz, and J. Worden (2012), Aerosol information content analysis of multi-angle high spectral resolution measurements and its benefit for high accuracy greenhouse gas retrievals, *Atmos. Meas. Tech.*, *5*(7), 1809–1821, aMT. 3.2.2

Garcia, R. D. M., and C. E. Siewert (1989), The fn method for radiative transfer models that include polarization effects, *Journal of Quantitative Spectroscopy and Radiative Transfer*, *41*(2), 117–145, doi: DOI: 10.1016/0022-4073(89)90133-7. (document), 2.4, 2.3

Grassl, H. (1971), Determination of aerosol size distributions from spectral attenuation measurements, *Applied Optics*, *10*(11), 2534–2538. 1.1.1

Halthore, R. N., T. F. Eck, B. N. Holben, and B. L. Markham (1997), Sun photometric measurements of atmospheric water vapor column abundance in the 940-nm band, *Journal of Geophysical Research: Atmospheres*, *102*(D4), 4343–4352. 2.2.1

Hansen, J. E., and L. D. Travis (1974), Light scattering in planetary atmospheres, *Space Sci. Rev.*, *16*, 572–610. 1.1.1, 1.1.3, 2.1, 2.2.1, 3.3.1, 4.1, 4.3.1, 4.3.2.3

Hansen, P. C. (1998), *Rank-Deficient and Discrete Ill-Posed Problems: Numerical Aspects of Linear Inversion*, Soc. for Ind. and Appl. Math., Philadelphia, Pa. 3.3.3

Hasekamp, O. P., and J. Landgraf (2005a), Retrieval of aerosol properties over the ocean from multispectral single-viewing-angle measurements of intensity and polarization: Retrieval approach, information content, and sensitivity study, *J. Geophys. Res.*, *110*(D20), D20,207. 3.2.2, 3.3.1

Hasekamp, O. P., and J. Landgraf (2007), Retrieval of aerosol properties over land surfaces: capabilities of multiple-viewing-angle intensity and polarization measurements, *Applied Optics*, *46*(16), 3332–3344. 3.3.1

Hasekamp, O. P., P. Litvinov, and A. Butz (2011), Aerosol properties over the ocean from parasol multiangle photopolarimetric measurements, *Journal of Geophysical Research: Atmospheres*, *116*(D14), D14,204. 1.1.3

Haywood, J., and O. Boucher (2000), Estimates of the direct and indirect radiative forcing due to tropospheric aerosols: A review, *Rev. Geophys.*, *38*(4), 513–543. 1.1

Herman, B. M., S. R. Browning, and J. A. Reagan (1971), Determination of aerosol size distributions from lidar measurements, *Journal of the Atmospheric Sciences*, *28*(5), 763–771. 1.1.1

Hess, M., P. Koepke, and I. Schult (1998), Optical properties of aerosols and clouds: The software package opac, *Bulletin of the American Meteorological Society*, *79*(5), 831–844. (document), 2.5, 4.2.1

Holben, B. N., et al. (1998), Aeronet - a federated instrument network and data archive for aerosol characterization, *Remote Sensing of Environment*, *66*(1), 1–16. 1.1, 1.1.1, 1.1.2, 4.2.2

Holben, B. N., T. F. Eck, I. Slutsker, A. Smirnov, A. Sinyuk, J. Schafer, D. Giles, and O. Dubovik (2006), Aeronet's version 2.0 quality assurance criteria, *Proc. SPIE 6408, Remote Sensing of the Atmosphere and Clouds*, *64080Q*, 10.1117/12.706524. 1.1.3, 3.3.5, 4.4

Hovenier, J., C. v. d. Mee, and H. Domke (2004), *Transfer Of Polarized Light In Planetary Atmospheres*, 258 pp., Kluwer Academic Publishers, Dordrecht, The Netherlands. 2.1

Kahn, R. A., B. J. Gaitley, M. J. Garay, D. J. Diner, T. F. Eck, A. Smirnov, and B. N. Holben (2010), Multiangle imaging spectroradiometer global aerosol product assessment by comparison with the aerosol robotic network, *J. Geophys. Res.*, *115*(D23), D23,209. 1.1.3

Kaufman, Y. J., A. Gitelson, A. Karnieli, E. Ganor, R. S. Fraser, T. Nakajima, S. Mattoo, and B. N. Holben (1994), Size distribution and scattering phase function of aerosol particles retrieved from sky brightness measurements, *Journal of Geophysical Research: Atmospheres*, *99*(D5), 10,341–10,356. 1.1.1

Kaufman, Y. J., D. Tanré, L. A. Remer, E. F. Vermote, A. Chu, and B. N. Holben (1997), Operational remote sensing of tropospheric aerosol over land from eos moderate resolution imaging spectroradiometer, *Journal of Geophysical Research: Atmospheres*, *102*(D14), 17,051–17,067. 1.1.3

Kaufman, Y. J., D. Tanre, and O. Boucher (2002), A satellite view of aerosols in the climate system, *Nature*, *419*, 215 – 223. 1.1

King, M. D., D. M. Byrne, B. M. Herman, and J. A. Reagan (1978), Aerosol size distributions obtained by inversions of spectral optical depth measurements, *Journal of the Atmospheric Sciences*, *35*(11), 2153–2167. 1.1.1

Knobelspiesse, K., B. Cairns, M. Mishchenko, J. Chowdhary, K. Tsigaridis, B. van Diedenhoven, W. Martin, M. Ottaviani, and M. Alexandrov (2012), Analysis of fine-mode aerosol retrieval capabilities by different passive remote sensing instrument designs, *Optics Express*, *20*(19), 21,457–21,484. 3.2.2, 4.4

Levelt, P. F., E. Hilsenrath, G. W. Leppelmeier, G. H. J. van den Oord, P. K. Bhartia, J. Tamminen, J. F. de Haan, and J. P. Veefkind (2006), Science objectives of the ozone monitoring instrument, *Geoscience and Remote Sensing, IEEE Transactions on*, *44*(5), 1199–1208. 2.2.1

Levy, R. C., L. A. Remer, and O. Dubovik (2007a), Global aerosol optical properties and application to moderate resolution imaging spectroradiometer aerosol retrieval over land, *Journal of Geophysical Research: Atmospheres*, *112*(D13), D13,210. 1.1.3

Levy, R. C., L. A. Remer, S. Mattoo, E. F. Vermote, and Y. J. Kaufman (2007b), Second-generation operational algorithm: Retrieval of aerosol properties over land from inversion of moderate resolution imaging spectroradiometer spectral reflectance, *J. Geophys. Res.*, *112*(D13), D13,211. 1.1.3

Levy, R. C., L. A. Remer, R. G. Kleidman, S. Mattoo, C. Ichoku, R. Kahn, and T. F. Eck (2010), Global evaluation of the collection 5 modis dark-target aerosol products over land, *Atmos. Chem. Phys.*, *10*(21), 10,399–10,420, aCP. 1.1.3

Li, Z., et al. (2009), Improvements for ground-based remote sensing of atmospheric aerosol properties by additional polarimetric measurements, *Journal of Quantitative Spectroscopy and Radiative Transfer*, *110*(17), 1954–1961. 1.1.2, 1.1.3, 4.1, 4.2.2

Liou, K. N. (2002), *An Introduction to Atmospheric Radiation*, 583 pp., Academic Press, San Diego, CA, USA, volume 84 doi: DOI: 10.1016/S0074-6142(02)80015-8. 2.2.1

Litvinov, P., O. Hasekamp, and B. Cairns (2011), Models for surface reflection of radiance and polarized radiance: Comparison with airborne multi-angle photopolarimetric

measurements and implications for modeling top-of-atmosphere measurements, *Remote Sensing of Environment*, *115*(2), 781–792. 2.2.3

Lucht, W., C. B. Schaaf, and A. H. Strahler (2000), An algorithm for the retrieval of albedo from space using semiempirical brdf models, *Geoscience and Remote Sensing, IEEE Transactions on*, *38*(2), 977–998. 2.2.3, 2.2.3

Maignan, F., F. M. Bréon, and R. Lacaze (2004), Bidirectional reflectance of earth targets: evaluation of analytical models using a large set of spaceborne measurements with emphasis on the hot spot, *Remote Sensing of Environment*, *90*(2), 210–220. 2.2.3

Maignan, F., F.-M. Bréon, E. Fédèle, and M. Bouvier (2009), Polarized reflectances of natural surfaces: Spaceborne measurements and analytical modeling, *Remote Sensing of Environment*, *113*(12), 2642–2650. 2.2.3, 2.2.3, 2.2.3

Martonchik, J. V., R. A. Kahn, and D. J. Diner (2009), *Retrieval of aerosol properties over land using MISR observations*, Springer, Berlin. 1.1.3

McClatchey, R. A., R. W. Fenn, J. E. A. Selby, F. E. Volz, and J. S. Garing (1972), Optical properties of the atmosphere (third edition), *Report*, Air Force Cambridge Research Labs Hanscom AFB MA. (document), 2.2, 2.2

Mishchenko, M. I., and L. D. Travis (1997), Satellite retrieval of aerosol properties over the ocean using polarization as well as intensity of reflected sunlight, *J. Geophys. Res.*, *102*(D14), 16,989–17,013. 1.1.3, 4.1

Mishchenko, M. I., and L. D. Travis (1998), Capabilities and limitations of a current fortran implementation of the t-matrix method for randomly oriented, rotationally symmetric scatterers, *Journal of Quantitative Spectroscopy and Radiative Transfer*, *60*(3), 309–324. 2.2.2

Mishchenko, M. I., L. D. Travis, and D. W. Mackowski (1996), T-matrix computations of light scattering by nonspherical particles: A review, *Journal of Quantitative Spectroscopy and Radiative Transfer*, *55*(5), 535–575. 2.2.2

Mishchenko, M. I., L. D. Travis, and A. A. Lacis (2002), *Scattering, Absorption, and Emission of Light by Small Particles*, Cambridge University Press, Cambridge, UK. 1.1.3, 2.1

Mishchenko, M. I., B. Cairns, J. E. Hansen, L. D. Travis, R. Burg, Y. J. Kaufman, J. Vanderlei Martins, and E. P. Shettle (2004), Monitoring of aerosol forcing of climate from space: analysis of measurement requirements, *Journal of Quantitative Spectroscopy and Radiative Transfer*, *88*(1-3), 149–161. 1.1, 1.1.3, 4.3.2.1, 4.4, 4.3.2.3

Mishchenko, M. I., et al. (2007), Accurate monitoring of terrestrial aerosols and total solar irradiance: Introducing the glory mission, *Bulletin of the American Meteorological Society*, *88*(5), 677–691. 1.1.3, 3.3.1

Myhre, G., et al. (2013), *Anthropogenic and Natural Radiative Forcing. In Climate Change 2013: The Physical Science Basis. Contribution of Working Group I to the Fifth Assessment Report of the Intergovernmental Panel on Climate Change [Stocker T.F., et al. (eds.)]*, book section 8, p. 659–740, Cambridge University Press, Cambridge, United Kingdom and New York, NY, USA. 1.1

Nadal, F., and F. M. Breon (1999), Parameterization of surface polarized reflectance derived from polder spaceborne measurements, *Geoscience and Remote Sensing, IEEE Transactions on*, *37*(3), 1709–1718. 2.2.3

Nakajima, T., M. Tanaka, and T. Yamauchi (1983), Retrieval of the optical properties of aerosols from aureole and extinction data, *Applied Optics*, *22*(19), 2951–2959. 1.1.1

Nakajima, T., G. Tonna, R. Rao, P. Boi, Y. Kaufman, and B. Holben (1996), Use of sky brightness measurements from ground for remote sensing of particulate polydispersions, *Applied Optics*, *35*(15), 2672–2686. 1.1.1

Orphal, J., and K. Chance (2003), Ultraviolet and visible absorption cross-sections for hitran, *Journal of Quantitative Spectroscopy and Radiative Transfer*, *82*(1-4), 491–504. 2.2.1

Patterson, E. M., D. A. Gillette, and B. H. Stockton (1977), Complex index of refraction between 300 and 700 nm for saharan aerosols, *Journal of Geophysical Research*, *82*(21), 3153–3160. 4.2.1

Phillips, D. L. (1962), A technique for the numerical solution of certain integral equations of the first kind, *J. ACM*, *9*(1), 84–97. 1.1.1, 3.3.2

Ramanathan, V., P. J. Crutzen, J. T. Kiehl, and D. Rosenfeld (2001), Aerosols, climate, and the hydrological cycle, *Science*, *294*(5549), 2119–2124. 1.1

Reid, J. S., et al. (2008), An overview of uae2 flight operations: Observations of summertime atmospheric thermodynamic and aerosol profiles of the southern arabian gulf, *Journal of Geophysical Research: Atmospheres*, *113*(D14), D14,213. 1.1.2, 4.1, 4.2.2

Remer, L. A., et al. (2005), The modis aerosol algorithm, products, and validation, *Journal of the Atmospheric Sciences*, *62*(4), 947–973. 1.1.3

Ricchiazzi, P., S. Yang, C. Gautier, and D. Sowle (1998), Sbdart: A research and teaching software tool for plane-parallel radiative transfer in the earth's atmosphere, *Bulletin of the American Meteorological Society*, *79*(10), 2101–2114. (document), 2.2, 2.3

Rodgers, C. D. (1998), Information content and optimisation of high spectral resolution remote measurements, *Advances in Space Research*, *21*(3), 361–367. 3.2.2, 3.2.2

Rodgers, C. D. (2000), *Inverse Methods for Atmospheric Sounding: Theory and Practice*, World Scientific, Singapore. 3.2.1, 3.2.1, 3.2.2, 3.3.3

Rothman, L. S., et al. (2009), The hitran 2008 molecular spectroscopic database, *Journal of Quantitative Spectroscopy and Radiative Transfer*, *110*(9-10), 533–572, doi: DOI: 10.1016/j.jqsrt.2009.02.013. 2.2.1

Sanghavi, S., J. V. Martonchik, J. Landgraf, and U. Platt (2012), Retrieval of aerosol optical depth and vertical distribution using o2 a- and b-band sciamachy observations over kanpur: a case study, *Atmos. Meas. Tech.*, *5*(5), 1099–1119, aMTD. 3.2.2

Schuster, G. L., O. Dubovik, and B. N. Holben (2006), Angstrom exponent and bimodal aerosol size distributions, *J. Geophys. Res.*, *111*, D07,207. 2.2.2, 3.3.1, 4.4

Seinfeld, J. H., and S. N. Pandis (2006), *Atmospheric Chemistry and Physics: From Air Pollution to Climate Change, 2nd Edition*, 1232 pp., John Wiley and Sons, Inc., Hoboken, New Jersey. 2.2.2

Shannon, C. E. (1948), A mathematical theory of communication, *Bell System Technical Journal*, *27*(3), 379–423. 3.2.2

Shaw, G. E. (1979), Inversion of optical scattering and spectral extinction measurements to recover aerosol size spectra, *Applied Optics*, *18*(7), 988–993. 1.1.1

Smirnov, A., B. N. Holben, T. F. Eck, O. Dubovik, and I. Slutsker (2000), Cloud-screening and quality control algorithms for the aeronet database, *Remote Sensing of Environment*, *73*(3), 337–349. 1.1.2

Spurr, R. (2006), Vlidort: A linearized pseudo-spherical vector discrete ordinate radiative transfer code for forward model and retrieval studies in multilayer multiple scattering media, *Journal of Quantitative Spectroscopy and Radiative Transfer*, *102*, 316–342. 2.2.1, 2.2.4, 3.3

Spurr, R., and M. Christi (2014), On the generation of atmospheric property jacobians from the (v)lidort linearized radiative transfer models, *Journal of Quantitative Spectroscopy and Radiative Transfer*, *142*(0), 109–115. C

Spurr, R., J. Wang, J. Zeng, and M. I. Mishchenko (2012), Linearized t-matrix and mie scattering computations, *Journal of Quantitative Spectroscopy and Radiative Transfer*, *113*(6), 425–439. 2.2.2, 3.3

Spurr, R. J. D. (2004), A new approach to the retrieval of surface properties from earthshine measurements, *Journal of Quantitative Spectroscopy and Radiative Transfer*, *83*(1), 15–46. 2.2.3, 3.3

Tanaka, M., T. Nakajima, and T. Takamura (1982), Simultaneous determination of complex refractive index and size distribution of airborne and water-suspended particles from light scattering measurements, *Meteorological Society of Japan Journal*, *60*, 1259–1272. 1.1.1

Tanaka, M., T. Takamura, and T. Nakajima (1983), Refractive index and size distribution of aerosols as estimated from light scattering measurements, *Journal of Climate and Applied Meteorology*, *22*(7), 1253–1261. 1.1.1

Twomey, S. (1963), On the numerical solution of fredholm integral equations of the first kind by the inversion of the linear system produced by quadrature, *J. ACM*, *10*(1), 97–101. 1.1.1, 3.3.2

Twomey, S. (1977), *Introduction to the Mathematics of Inversion in Remote Sensing and Indirect Measurements*, 243 pp., Dover Publications, Inc., Mineola, NY, USA. 3.3.2

Twomey, S., and H. B. Howell (1967), Some aspects of the optical estimation of microstructure in fog and cloud, *Applied Optics*, *6*(12), 2125–2131. 1.1.1

van de Hulst, H. C. (1981), *Light Scattering by Small Particles (Dover edition)*, Dover Publications, Mineola, New York. 4.3.1, 4.3.1

Vermeulen, A., C. Devaux, and M. Herman (2000), Retrieval of the scattering and microphysical properties of aerosols from ground-based optical measurements including polarization. i. method, *Appl. Opt.*, *39*(33), 6207–6220. 4.1

Vijay, N., and J. W. Hovenier (2012), Polarized light reflected and transmitted by thick rayleigh scattering atmospheres, *The Astrophysical Journal*, *748*(1), 28. 2.3

Wagner, R., T. Ajtai, K. Kandler, K. Lieke, C. Linke, T. Müller, M. Schnaiter, and M. Vragel (2012), Complex refractive indices of saharan dust samples at visible and near uv wavelengths: a laboratory study, *Atmospheric Chemistry and Physics*, *12*(5), 2491–2512. 4.2.1

Wang, J., X. Xu, R. Spurr, Y. Wang, and E. Drury (2010), Improved algorithm for modis satellite retrievals of aerosol optical thickness over land in dusty atmosphere: Implications for air quality monitoring in china, *Remote Sensing of Environment*, *114*(11), 2575–2583, doi: DOI: 10.1016/j.rse.2010.05.034. 1.1.3, 3.3.2

Wang, J., X. Xu, D. K. Henze, J. Zeng, Q. Ji, S.-C. Tsay, and J. Huang (2012), Top-down estimate of dust emissions through integration of modis and misr aerosol retrievals with the geos-chem adjoint model, *Geophys. Res. Lett.*, *39*(8), L08,802. 3.3

Wang, J., X. Xu, S. Ding, J. Zeng, R. Spurr, X. Liu, K. Chance, and M. Mishchenko (2014), A numerical testbed for remote sensing of aerosols, and its demonstration for evaluating retrieval synergy from a geostationary satellite constellation of geo-cape and goes-r, *Journal of Quantitative Spectroscopy and Radiative Transfer*, *146*(0), 510–528. (document), 2.2, 2.3, 2.4, 2.5, 2.6

Wanner, W., X. Li, and A. H. Strahler (1995), On the derivation of kernels for kernel-driven models of bidirectional reflectance, *Journal of Geophysical Research: Atmospheres*, *100*(D10), 21,077–21,089. 2.2.3, 2.2.3

Waquet, F., P. Goloub, J. L. Deuzé, J. F. Léon, F. Auriol, C. Verwaerde, J. Y. Balois, and P. François (2007), Aerosol retrieval over land using a multiband polarimeter and comparison with path radiance method, *Journal of Geophysical Research*, *112*(D11). 2.2.3

Waquet, F., B. Cairns, K. Knobelspiesse, J. Chowdhary, L. D. Travis, B. Schmid, and M. I. Mishchenko (2009), Polarimetric remote sensing of aerosols over land, *J. Geophys. Res.*, *114*(D1), D01,206. 1.1.3, 2.2.2, 3.3.1

Wendisch, M., and W. Von Hoyningen-Huene (1994), Possibility of refractive index determination of atmospheric aerosol particles by ground-based solar extinction and scattering measurements, *Atmospheric Environment*, *28*(5), 785–792. 1.1.1

Xu, X., J. Wang, D. K. Henze, W. Qu, and M. Kopacz (2013), Constraints on aerosol sources using geos-chem adjoint and modis radiances, and evaluation with multisensor (omi, misr) data, *Journal of Geophysical Research: Atmospheres*, *118*(12), 6396–6413. 3.3

Yamamoto, G., and M. Tanaka (1969), Determination of aerosol size distribution from spectral attenuation measurements, *Applied Optics*, *8*(2), 447–453. 1.1.1

Yamasoe, M. A., Y. J. Kaufman, O. Dubovik, L. A. Remer, B. N. Holben, and P. Artaxo (1998), Retrieval of the real part of the refractive index of smoke particles from sun/sky measurements during scar-b, *Journal of Geophysical Research: Atmospheres*, *103*(D24), 31,893–31,902. 1.1.1

Yang, Z., J. Wang, C. Ichoku, E. Hyer, and J. Zeng (2013), Mesoscale modeling and satellite observation of transport and mixing of smoke and dust particles over northern sub-saharan african region, *Journal of Geophysical Research: Atmospheres*, *118*(21), 12,139–12,157. 1.1.3

Zeng, J., Q. Han, and J. Wang (2008), High-spectral resolution simulation of polarization of skylight: Sensitivity to aerosol vertical profile, *Geophys. Res. Lett.*, *35*(20), L20,801. 4.1

Zhu, C., R. H. Byrd, P. Lu, and J. Nocedal (1994), L-bfgs-b: a limited memory fortran code for solving bound constrained op- timization problems, *Technique report*, Northwestern University. 3.3.3

Ångström, A. (1929), On the atmospheric transmission of sun radiation and on dust in the air, *Geografiska Annaler*, *11*, 156–166. 1.1.1

LIST OF PUBLICATIONS

List my publication here